## *Constraining the dark matter particle mass through galaxy-galaxy strong gravitational lensing*

HE, QIUHAN

# Constraining the dark matter particle mass through galaxy-galaxy strong gravitational lensing

Qiuhan He

A thesis presented for the degree of

Doctor of Philosophy

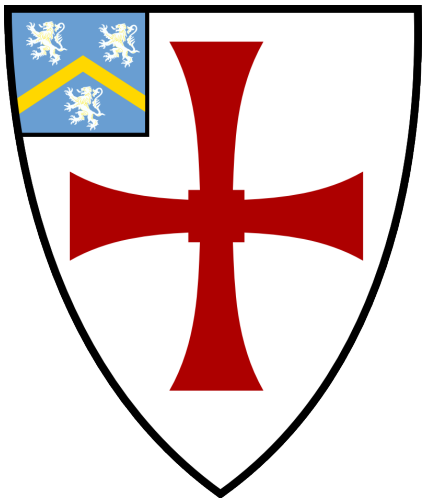

Institute for Computational Cosmology

The University of Durham

United Kingdom

Nov 2022

“采菊东篱下，悠然见南山。”

————陶渊明

# Constraining the dark matter particle mass through galaxy-galaxy strong gravitational lensing

**Qiuhan He**

**Abstract**

We study several possible ways of constraining the dark matter particle mass through galaxy-galaxy strong gravitational lensing, where the key underlying idea is that a strong lens image could be perturbed by low-mass haloes that happen to be close to light-rays emitted from a background source galaxy. Under the Approximate Bayesian Computation framework, we develop a forward-modelling procedure aimed at directly placing constraints on the dark particle's thermal relic mass using a set of observations. We use mock images to demonstrate its ability to extract subhalo information from the power spectrum of image residuals and unbiasedly recover the input mass of the dark matter particles. We re-derive the number density of detectable intervening line-of-sight haloes relative to lens subhaloes in galaxy-galaxy strong lens observations. Unlike previous methods determining the detectability through fitting deflections or idealistic images, we regard a perturber as detectable only if adding it to a smooth model generates a statistically significant improvement in the reconstructed image. Our new results show that line-of-sight haloes are still important but, in most cases, no longer completely dominate detections over those of subhaloes. Finally, we study the effects on subhalo inference from the complexity of the lens through simulating mock lensed images with a lens from a high-resolution hydrodynamic simulation. We find that the commonly used lens model, a power-law profile, could wrongly infer the subhalo information if it cannot capture the non-elliptical features of the lens galaxy. We also consider a decomposed model for the lens mass, which separately models the stellar and dark matter mass. We find the decomposed model can successfully capture the complexity of the simulated galaxy and correctly infer the subhalo information.

Supervisors: Carlos S. Frenk, Shaun Cole and Richard Massey

# Acknowledgements

First of all, I would like to thank my supervisors, Prof. Carlos S. Frenk, Prof. Shaun Cole and Prof. Richard Massey for providing me such a great opportunity to study very interesting and attracting scientific questions in Durham, a quiet and beautiful medieval-like town. I could not imagine how challenging the journey would be without their guidance, support and encouragement. The generosity, enthusiasm, patience and optimism that I received from them should be my lifelong treasure. I am also thankful for my other "informal" supervisors, Dr. James Nightingale, Dr. Andrew Robertson and Dr. Aristeidis Amvrosiadis for their help in all aspects of my project and patience in attending almost every weekly meeting over the last four years! I really enjoy those discussions since people always have amazing and new ideas! In addition, I would like to thank Dr. Ran Li for introducing me to the astronomy field when I was a sophomore at UCAS and for continuing to provide me with professional advice.

Thanks to all my colleagues including Amy Etherington, Sam Lange, Dr. Xiaoyue Cao, Dr. Nicola Armorisco and Prof. R. Benton Metcalf for their contribution to the work in the thesis. As well, I would like to thank the PyAutoLens team for building an excellent tool that I can use to realize a wide range of ideas.

Special thanks to my friends in Durham, Alberto, Alex, Amy, Aoife, Arnau, Ashly, Boye, Carol, Christoph, Chengzong, Difu, Ellen, Giorgio, Joaquin, Han, Hailin, Lai, Miguel, Myles, Sergio, Shao Shi, Sut-Ieng and Victor. I will always remember the drinks we had together. Also thanks to my old friends, Hengsheng, Kunpeng, Xiangkun, Xing and Yangting for their long-term support, particularly during the pandemic.

Finally, I would like to thank my family, my parents and grandparents for their support during all my life. Of course, to my dearest girl, Xuewen, thanks for all the

happiness you have brought to me. You make me happier than I had ever thought I would be. I feel so fortunate that I can meet you in my life.

# Contents

# Declaration

The work described in this thesis was undertaken between October 2018 and August 2022 while the author was a research student under the supervision of Professor Carlos S. Frenk, Professor Shaun Cole and Professor Richard Massey at the Institute for Computational Cosmology in the Department of Physics at Durham University. This work has not been submitted for any other degree at Durham University or any other university.

Chapter 2 of this thesis has been published in the form of a paper:

- He, Qiuhan; Robertson, Andrew; Nightingale, James; Cole, Shaun; Frenk, Carlos S.; Massey, Richard; Amvrosiadis, Aristeidis; Li, Ran; Cao, Xiaoyue; Etherington, Amy. **A forward-modelling method to infer the dark matter particle mass from strong gravitational lenses**, *Monthly Notices of the Royal Astronomical Society* (2022) **511**: 3046-3062.

Chapter 3 of this thesis has been published in the form of a paper:

- He, Qiuhan; Li, Ran; Frenk, Carlos S.; Nightingale, James; Cole, Shaun; Amorisco, Nicola C.; Massey, Richard; Robertson, Andrew; Etherington, Amy; Amvrosiadis, Aristeidis; Cao, Xiaoyue. **Galaxy–galaxy strong lens perturbations: line-of-sight haloes versus lens subhaloes**, *Monthly Notices of the Royal Astronomical Society* (2022) **512**: 5862-5873.

Chapter 4 has been published in the form of a paper:

- He, Qiuhan; Nightingale, James; Robertson, Andrew; Amvrosiadis, Aristeidis; Cole, Shaun; Frenk, Carlos S.; Massey, Richard; Li, Ran; Amorisco, Nicola C.; Metcalf, R. Benton; Cao, Xiaoyue; Etherington, Amy. **Testing strong**

**lensing subhalo detection with a cosmological simulation**, *Monthly Notices of the Royal Astronomical Society* (2023) **518**: 220-239.

# List of Figures

# List of Tables

Chapter 1

# Introduction

In 1930s, when studying the velocities of galaxies within the Coma Cluster, Fritz Zwicky realized that the galaxies were moving so fast that an unseen mass, hundreds of times more massive than the stellar mass, must exist to prevent the cluster disintegrating and for the first time he referred to such unseen mass as "dark matter" (DM) (Zwicky, 1933, 1937). Since then, more and more astrophysical observations like the study of galaxy motion and rotation curves (Kahn and Woltjer, 1959, Rubin and Ford, 1970) have confirmed the common existence of DM. In recent decades, with great advances in both the observations and theories, researchers have made many breakthroughs in cosmology and established the standard cosmological paradigm, the $\Lambda$ cold dark matter ($\Lambda$CDM) model (see Frenk and White, 2012, for a review), which has successfully accounted for many observations, like the inhomogeneities of cosmic microwave background (CMB) and the clustering of galaxies.

According to the standard model, the Universe starts with a big bang from a very hot and compact point. As the Universe expands, particles precipitate from the thermal background as temperatures and pressure decrease. After a while, matter clusters and creates various structures, eventually evolving into the Universe we live in today. According to the dominant form of energy, the Universe can be divided into three epochs chronologically: radiation-dominated, matter-dominated,

and dark energy-dominated epoch. Most particles move relativistically during the radiation-dominated epoch and matter is prevented from collapsing to form haloes by the radiative pressure. Additionally, in the radiation-dominated epoch, most of the time the Universe is opaque, but towards the end of the epoch, nuclei start to capture free electrons that eventually allow photons to travel freely through the Universe, leading to the creation of CMB. Approximately at the same time, the Universe enters the matter-dominated epoch, in which dark matter haloes develop gradually as gravitational forces outweigh radiation pressures. The seeds of gravitational instability are thought to originate in the primordial quantum perturbations at very early times, which later expand with the inflation of the Universe. It is normally assumed that the perturbations have a broad spectrum. However, due to the free streaming of dark matter particles during the radiation-dominated epoch, some small perturbations may have been smoothed out before dark matter haloes form. As a result of the free-streaming scheme, the mass of a dark halo has a lower limit. The free-streaming scale, $\lambda_{\rm FS}$, can be approximated as the addition of two lengths, the relativistic and non-relativistic travelling lengths (Schneider et al., 2012):

$$\begin{aligned}\lambda_{\rm FS} &\equiv \int_0^{t_{\rm eq}} \frac{v(t)}{a(t)} dt \approx \int_0^{t_{\rm nr}} \frac{\rm c}{a(t)} dt + \int_{t_{\rm nr}}^{t_{\rm eq}} \frac{v(t)}{a(t)} dt \\ &\approx \frac{2{\rm c}t_{\rm nr}}{a\left(t_{\rm nr}\right)} \left(1 + \log\left(\frac{a\left(t_{\rm eq}\right)}{a\left(t_{\rm nr}\right)}\right)\right),\end{aligned} \tag{1.1}$$

where c is the speed of light, $a$ is the scale factor, $t_{\rm nr}$ and $t_{\rm eq}$ refer to the time when the (dark) particles become non-relativistic and the time when the matter-dominated epoch starts, respectively. As shown, the free-streaming scale is related to the time when the (dark) particles precipitate from the thermal background. The heavier the particle, the sooner it decouples from the thermal background, resulting in a smaller free-streaming scale and therefore a lower mass a halo can have. As a result, the lower limit for the mass of a dark halo can be approximated by the "free-streaming" mass, $m_{\rm FS}$, as

$$m_{\rm FS} \equiv \frac{4\pi}{3} \rho_{\rm m} \left(\frac{1}{2}\lambda_{\rm FS}\right)^3, \tag{1.2}$$

where $\rho_{\rm m}$ is the (dark) matter density at the time when the matter-dominated epoch starts.

The core of the ΛCDM model is the hierarchical formation of self-bound dark matter haloes due to gravitational instability. Small clumps of dark matter first form after the Universe enters into the matter-dominated epoch and those small clumps grow into larger and larger dark matter haloes through accreting surrounding dark matter particles and also merging with other clumps. Later on, precipitated baryonic gas from the thermal background flows into these dark haloes' centres and gives birth to stars and galaxies, if the dark halo is massive enough to accrete enough gas (White and Rees, 1978, White and Frenk, 1991). As the picture describes, the theory predicts a vast abundance of dark matter haloes from a mass scale of galaxy clusters down to around the scale given by the free-streaming of dark matter matter particles during the radiation-dominated epoch as shown by Eq. 1.1 and 1.2. For a typical CDM particle of $\sim 100$ GeVs, the corresponding lowest halo mass is around the Earth mass (Frenk and White, 2012, Wang et al., 2020). The theory also predicts that the mass function of those haloes (the abundance as a function of halo mass) should be well characterised by a simple power law except for an exponential cut-off at the very high mass end. In the intermediate mass regime, the mass function has been well constrained by large sky surveys through counting galaxies and is shown to agree well with the single power-law prediction (Frenk et al., 1990, Rozo et al., 2010). However, in lower mass ranges ($< 10^{10}$ $M_\odot$) where a dark matter halo would not be massive enough to hold a luminous galaxy (Thoul and Weinberg, 1996, Efstathiou, 1992, Benson et al., 2002, Sawala et al., 2016, Benitez-Llambay and Frenk, 2020), direct counting of dark haloes becomes infeasible and the form of the mass function remains unclear. The unconstrained low mass range of the mass function below around $10^{10}$ $M_\odot$ leaves spaces for other physically motivated particle candidates for DM, besides typically-assumed CDM particles, which are traditionally expected to be a kind of super-symmetric particle of several hundred GeV (Hut, 1977, Scherrer and Turner, 1986). Famously, by con-

trast, a family of lighter particles called "warm" dark matter could damp relatively larger fluctuations in the early Universe due to their later decoupling from the thermal background, which limits the smallest size of dark halo that could form in the early Universe. For example, if the dark matter particle is a sterile neutrino with a mass of several keV, the lower cut-off of the mass function would be in the range between $10^7$ to $10^{10}$ $M_\odot$. These models have recently received increasing attention due to the failure to detect the signature of super-symmetric particles in ground-based experiments (Cui et al., 2017, Aprile and Xenon Collaboration, 2017, Akerib et al., 2017), which makes it more important and meaningful to push further the constraint on the form of dark halo mass function to lower masses through non-direct astrophysical methods.

Several approaches have been proposed and applied to extract abundance information of invisible small dark matter haloes based on different astrophysical effects of those haloes. For example, at cosmological distances, people can estimate the line-of-sight abundance of small dark matter haloes by analyzing the spectrum of Lyman-alpha emission from distant quasars, since every time that light passes through a dark halo it would be partially absorbed by the gas within the halo and thus reveal information about haloes along the line of sight (Viel et al., 2013, Iršič et al., 2017, Garzilli et al., 2019). Similarly, people analyze strong gravitational lensing systems to extract evidence of tiny perturbations that dark matter haloes would cause when the background galaxy's light happens to pass by one of them (Koopmans, 2005, Vegetti and Koopmans, 2009a,b, Vegetti et al., 2012, Hezaveh et al., 2016, Li et al., 2016b). For smaller scales within the Milky Way, people can use the abundance of the Milky Way's satellites to constrain the dark matter halo mass function, since different dark matter models predict different numbers of satellites, though this is complicated by baryonic physics processes (Newton et al., 2021). In addition, with accurate position and velocity measurements of Milky Way stellar streams from Gaia (Gaia Collaboration et al., 2018), people have started studying the perturbations caused by haloes a stream might encounter, and

used them to infer the abundance of those small haloes (Banik et al., 2021, Hermans et al., 2021). Every approach has its own strengths and weaknesses. For example, the Lyman-alpha emission analysis and studies of Milky Way satellites can at most constrain the mass function around $10^9$ $M_\odot$, where below that very little gas is ever bound in dark matter haloes making them extremely difficult to observe. However, ideally stellar streams can place constraints down to $\sim 10^6$ $M_\odot$ since the measurement is made on individual stars, which are sensitive to very small gravitational perturbations. In terms of constraints from strong lensing, it is expected to constrain the mass function down to $\sim 10^7$ $M_\odot$ and has the unique advantage of constraining low mass line-of-sight dark matter haloes whose properties are hardly affected by complicated baryonic physics. The challenge which exists in strong lensing modelling is simultaneously solving for the unknown foreground galaxy mass distribution and background galaxy light distribution. Much effort has been made in this field during the past decade, however, due to the complexity of the technique and the data size and quality, only a few dark matter haloes have been detected and the constraint from strong lensing is not yet comparable with some of other methods. However, within this decade, hundreds of times more strong lensing systems will be discovered with better image quality by new telescopes, such as the James Webb Space Telescope (JWST), Euclid Space Telescope (EST) and China Space Station Telescope (CSST), which promise to enable much tighter constraints on the halo mass function. In this thesis, we further investigate the methodology of utilizing strong lensing to constrain the dark halo mass function and develop parts of the methods to prepare for the data that will be coming soon.

To aide in the understanding of topics discussed later in this thesis, in the following parts of this Chapter we will introduce some relevant background. In Section 1.1, we introduce some basic models and properties of dark matter haloes. Then in Section 1.2 we describe concepts and formulae related to the phenomenon of gravitational lensing. In Section 1.3, we summarize some recent progress in the field of

subhalo lensing and finally we give an outline of this thesis in Section 1.4.

## 1.1 Properties of dark matter haloes

### 1.1.1 Halo mass function

The halo mass function describes the most fundamental property, the abundance, of dark matter haloes. To be specific, it is defined as the number density of dark matter haloes per unit mass. Ignoring baryonic effects, in the CDM case, the halo mass function is almost a power law from galaxy cluster masses to an Earth mass, while in the WDM case, due to the damping of the power spectrum of initial perturbations, which prohibits the formation of haloes below a certain mass threshold, the halo mass function is expected to have a cut-off at sub-galaxy mass scales. In this thesis, following Gilman et al. (2019), we introduce a "cut-off" by defining the halo mass function, $F\left(M,z\right)$ as

$$F(M,z) \equiv \frac{d^2N}{dMdV}(M,z) = F_{\rm CDM}(M,z)\left(1+\frac{M_{\rm hf}}{M}\right)^{-1.3}, \tag{1.3}$$

where $M$ is the halo mass, $z$ is the redshift, and $F_{\rm CDM}$ is the mass function in the CDM case, which if not specified, takes the form and values given by Sheth et al. (2001). In Eq. 1.3, the "cut-off" on the lower end of the mass function is parameterized by the half-mode mass, $M_{\rm hf}$, a characteristic mass corresponding to the mass scale at which the dark matter transfer function falls to half the value of the CDM transfer function which can be related to the mass of the dark matter particle, $M_{\rm DM}$, by

$$M_{\rm hf} = 10^{10}\left(\frac{M_{\rm DM}}{\rm keV}\right)^{-3.33}{\rm M_\odot h^{-1}}, \tag{1.4}$$

where h is the Hubble parameter in units of 100 km s$^{-1}$ Mpc$^{-1}$ (Lovell et al., 2014) *.

*The transfer function is defined as $T\left(k\right) \equiv \sqrt{\frac{P(k)}{P_0(k)}}$, where $P\left(k\right)$ ($P_0\left(k\right)$) is the (primordial) dark matter power spectrum.

### 1.1.2 Dark matter halo profile

N-body simulations have shown that dark matter halo profiles can be accurately described by a simple fomula, the Navarro-Frenk-White (NFW) profile

$$\rho\left(r\right)=\frac{\rho_{\rm s}}{r/r_{\rm s}(1+r/r_{\rm s})^2}, \tag{1.5}$$

which has has only two free parameters, the scale radius, $r_{\rm s}$ and scale density, $\rho_{\rm s}$. The enclosed mass at radius, $r$, is then

$$M(r)=\int_0^r \frac{\rho_{\rm s}}{r'/r_{\rm s}(1+r'/r_{\rm s})^2}\cdot 4\pi r'^2{\rm d}r'=4\pi\rho_{\rm s}r_{\rm s}^3\left(\ln\frac{r_{\rm s}+r}{r_{\rm s}}-\frac{r}{r_{\rm s}+r}\right). \tag{1.6}$$

It is noted that as $r\to\infty$, $M\left(r\right)\propto\ln r$, and thus an NFW halo does not have a finite mass. When referring to the mass of an NFW halo, we usually first define a characteristic radius, $r_{200}$, within which the average density of the halo is 200 times the critical density of the Universe, and then we take the total mass within $r_{200}$ as the mass of the NFW halo, which is similarly denoted as $M_{200}$. The ratio between $r_{200}$ and $r_{\rm s}$ is defined as the concentration of the halo, $c\equiv r_{200}/r_{\rm s}$, and its relation with the halo mass is called the mass-concentration relation. As a result of the reduction in small-scale power with WDM, low mass dark haloes form later and are thus less concentrated compared with their CDM counterparts (Lovell et al., 2012, Schneider et al., 2012, Macciò et al., 2013, Bose et al., 2016, Ludlow et al., 2016). According to the *Copernicus Complexio* simulation (coco-warm), the mass-concentration relation in the WDM case can be empirically described as

$$c(M_{200},z)=c_{\rm CDM}(M_{200},z)\left((1+z)^{0.026z-0.04}\left(1+60\frac{M_{\rm hf}}{M_{200}}\right)^{-0.17}\right), \tag{1.7}$$

where $c_{\rm CDM}(M_{200},z)$ is the concentration in the CDM case. Throughout our work, we adopt the relation given by Ludlow et al. (2016) which shows remarkable agreement with the recent simulations from cluster to Earth mass scales (Wang et al., 2020). Note the relation only provides the median concentration as a function of mass, but Wang et al. (2020) have shown that the concentration at fixed mass has a log-normal distribution, with a standard deviation of 0.15 dex.

For a dark matter subhalo existing in a host galaxy, its outer part can be modified by environmental effects such as tidal stripping, which makes the outer density drop dramatically beyond some truncation radius (Gao et al., 2004). As a result, for subhaloes within a galaxy, we use the truncated NFW (tNFW) profile to describe their profiles (Baltz et al., 2009), which has the form

$$\rho\left(r\right)=\frac{\rho_{\mathrm{s}}}{r/r_{\mathrm{s}}(1+r/r_{\mathrm{s}})^{2}}\left(\frac{r_{\mathrm{t}}^{2}}{r_{\mathrm{t}}^{2}+r^{2}}\right)^{n}, \tag{1.8}$$

where $r_{\mathrm{t}}$ is the truncation radius, and $n$ is a parameter that controls the sharpness of the truncation. The form of a tNFW profile just adds a truncation term to the original NFW profile, and thus the $M_{200}$, $r_{200}$ and concentration can be defined for a tNFW halo in the same way as for an NFW halo. However, baryonic physics add more variations and complexity to the mass-concentration relation and so far there is not a unified model to describe the relation for subhaloes. It is noted that when $n>0$, the profile has a finite mass. Specially, if $n=1$, the total mass is

$$M_{\mathrm{t}}=4\pi\rho_{\mathrm{s}}r_{\mathrm{s}}^{3}\frac{\tau^{2}}{\left(\tau^{2}+1\right)^{2}}\left[\left(\tau^{2}-1\right)\ln\tau+\tau\pi-\left(\tau^{2}+1\right)\right], \tag{1.9}$$

where $\tau\equiv r_{\mathrm{t}}/r_{\mathrm{s}}$.

## 1.2 Gravitational lensing

Gravitational lensing is a phenomenon where light rays emitted from a background galaxy are deflected by foreground objects' gravitational potentials. In principle, images of cosmological objects are all "gravitationally lensed" at some level, but for most cases the distortion is hardly seen unless, from our viewpoint, a background galaxy happens to align with a massive foreground object, of which the chance is very rare. Though the prediction of a cosmological scale gravitational lensing has been made for decades, the phenomenon was only first confirmed through a double quasar system in 1980 (Young et al., 1980). Due to the rare chance of perfect alignment, by now only around 100 lensing systems with heavily distorted background images are observed. Depending on the scale of distortion of the

background galaxy, we usually divide the gravitational lensing into two categories, strong and weak lensing: in the strong lensing case, the background galaxy is almost perfectly aligned with the foreground galaxy and results in multiple or extended distorted images; In the weak lensing case, background galaxies are further away from alignment and the distortion is hardly observable and can only be extracted from statistical analysis. It is noted that both of these kinds of lensing are on the distance scale between different galaxies while there is a third kind of lensing called "micro lensing" which occurs on the scale within a galaxy. Recently, a wandering black hole was detected through the micro lensing (Sahu et al., 2022).

In this thesis we consider only strong lensing and in this section introduce some commonly used terminology in this particular field. For a thorough introduction to the whole theory of lensing we recommend the book of Schneider et al. (1992) for details. We first introduce the simplest case, a single-plane lensing system, where the light rays are deflected only once by the massive galaxy between the distant source galaxy and the observer. Then, based on the single-plane lensing system, we describe multi-plane systems where light rays from distant galaxies are deflected more than once.

### 1.2.1 Single-plane lensing systems

Fig. 1.1 shows a typical single-plane lensing configuration where the distant galaxy is usually called the "source", while the galaxy between the observer and the source is called the "lens". The angle $\vec{\hat{\alpha}}$ represents the angle by which a light ray is deflected, called the "un-scaled" deflection angle. The geometric relation between the observed position of the source, $\vec{\theta}$, the true position, $\vec{\beta}$, and $\vec{\hat{\alpha}}$ can be written as:

$$\vec{\beta}(\vec{\xi}) = \vec{\theta}(\vec{\xi}) - \frac{D_{\rm ls}}{D_{\rm s}}\vec{\hat{\alpha}}(\vec{\xi}), \tag{1.10}$$

where $D_{\rm ls}$ is the angular diameter distance between the source and the lens, and $D_{\rm s}$ is the angular diameter distance of the source. Under the "thin" plane assumption,

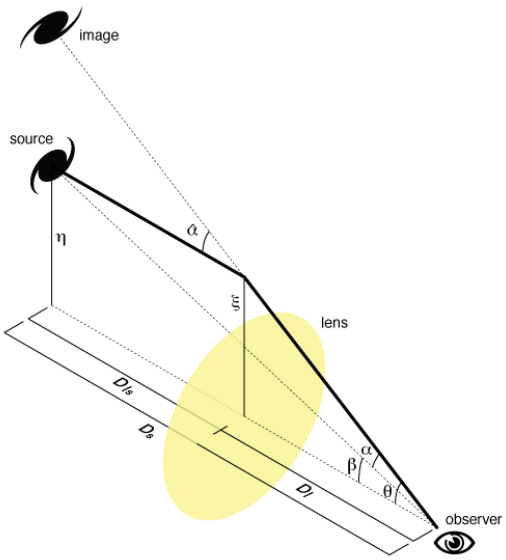


Figure 1.1: A typical single-plane lensing system. (Modified from https://en.wikipedia.org/wiki/Gravitational_lensing_formalism.)

where we assume all the lens mass is placed exactly on the same plane, for a lens galaxy with 2D mass distribution of $\Sigma(\xi)$, $\vec{\hat{\alpha}}$ can be calculated from (Eq. (2.1) of Schneider et al. (1992))

$$\vec{\hat{\alpha}}(\vec{\xi}) = \frac{4\mathrm{G}}{\mathrm{c}^2}\int \frac{(\vec{\xi}-\vec{\xi'})\Sigma(\xi')}{||\xi-\xi'||^2}d\xi'^2. \tag{1.11}$$

If we substitute $\vec{\xi}$ with $D_\mathrm{l}\vec{\theta}$, where $D_\mathrm{l}$ is the angular diameter distance of the lens, and define $\vec{\alpha} \equiv D_\mathrm{ls}\vec{\hat{\alpha}}/D_\mathrm{s}$, then the lensing equation, Eq. 1.11, can be re-written as

$$\vec{\alpha}(\vec{\theta}) = \frac{1}{\pi}\int \frac{(\vec{\theta}-\vec{\theta'})\kappa(\vec{\theta'})}{||\vec{\theta}-\vec{\theta'}||^2}d\vec{\theta'}^2, \tag{1.12}$$

where $\kappa(\vec{\theta}) \equiv \Sigma(\vec{\theta})/\Sigma_\mathrm{cr}$ is called the convergence map and $\Sigma_\mathrm{cr} \equiv \frac{\mathrm{c}^2 D_\mathrm{s}}{4\pi \mathrm{G} D_\mathrm{ls} D_\mathrm{l}}$ is the critical density of the lensing system. Since $\kappa(\vec{\theta})$ is proportional to the surface mass density, it is convenient to use $\kappa(\vec{\theta})$ to visualize the 2D mass distribution of the lens. Also, with the definitions above, Eq. 1.10 can be simplified to

$$\vec{\beta}(\vec{\theta}) = \vec{\theta} - \vec{\alpha}(\vec{\theta}), \tag{1.13}$$

and for convenience, we call $\vec{\alpha}$ the deflection angle. Since $\nabla_{\vec{\theta}}\ln||\vec{\theta}-\vec{\theta'}|| = \frac{(\vec{\theta}-\vec{\theta'})}{||\vec{\theta}-\vec{\theta'}||^2}$, we can define a lensing potential as

$$\psi(\vec{\theta}) \equiv \frac{1}{\pi}\int \kappa(\vec{\theta'})\ln||\vec{\theta}-\vec{\theta'}||d\vec{\theta'}^2, \tag{1.14}$$

of which the gradient is the deflection angle. We list some useful relations between $\psi(\vec{\theta})$, $\vec{\alpha}(\vec{\theta})$ and $\kappa(\vec{\theta})$ below,

$$\vec{\nabla}\psi(\vec{\theta}) = \vec{\alpha}(\vec{\theta}) \tag{1.15}$$

$$\vec{\nabla}\cdot\vec{\alpha}(\vec{\theta}) = 2\cdot\kappa(\vec{\theta}) \tag{1.16}$$

$$\nabla^2\psi(\vec{\theta}) = 2\cdot\kappa(\vec{\theta}). \tag{1.17}$$

We can also calculate the curl of the deflection angle, $\zeta(\vec{\theta})$, but the curl of the gradient of a scalar field, $\psi(\vec{\theta})$, is always zero, so $\zeta(\vec{\theta}) \equiv \nabla\times\vec{\alpha}(\vec{\theta}) = 0$. However, this is not true in multi-plane lensing systems. In fact, most of the equations shown above do not hold true in multi-plane cases, but with slight changes, similar concepts can be adapted into multi-plane lensing systems.

Viewing Eq. 1.13 as a coordinate transformation between the lens and source planes, under the first order approximation, we can describe the distortions with its Jacobi matrix defined as

$$J(\vec{\theta}) \equiv \frac{\partial\vec{\beta}}{\partial\vec{\theta}}(\vec{\theta}) = (1-\kappa(\vec{\theta}))\begin{bmatrix}1 & 0\\ 0 & 1\end{bmatrix} - \gamma(\vec{\theta})\begin{bmatrix}\cos 2\phi(\vec{\theta}) & \sin 2\phi(\vec{\theta})\\ \sin 2\phi(\vec{\theta}) & -\cos 2\phi(\vec{\theta})\end{bmatrix}, \tag{1.18}$$

where we see that the distortion can be decomposed into two terms, the isotropic distortion induced by the convergence and the non-isotropic distortion induced by the "shear", specified by its amplitude, $\gamma(\vec{\theta})$, and direction, $\phi(\vec{\theta})$.

### 1.2.2 Multi-plane lensing systems

A multi-plane lensing system can be easily viewed as a combination of many single-plane systems. First, we re-write the basic deflection angle equation, Eq. 1.10, in the multi-plane case. Assuming that the "thin" plane assumption holds true between each pair of planes, we can solve the lensing equation on each plane and connect them together to get the light paths through the whole system as:

$$\vec{\eta} = \frac{D_s}{D_1}\vec{\xi}_1 - \sum_{i=1}^{N} D_{is}\hat{\vec{\alpha}}_i(\vec{\xi}_i), \tag{1.19}$$

where

$$\vec{\xi}_j = \frac{D_j}{D_1}\vec{\xi}_1 - \sum_{i=1}^{j-1} D_{ij}\hat{\vec{\alpha}}_i(\vec{\xi}_i). \tag{1.20}$$

Note that the definition of $\hat{\vec{\alpha}}_i$ is the same as in the single-plane case, which represents the un-scaled deflection angle induced by the mass on the $i$-th plane. Again, by substituting $\vec{\xi}_i$ with $\vec{\theta}_i D_i$, and $\hat{\vec{\alpha}}_i$ with $\vec{\alpha}_i D_{\rm is}/D_{\rm s}$, we can simplify Eq. 1.20 as

$$\vec{\beta}(\vec{\theta}_1) = \vec{\theta}_1 - \sum_{i=1}^{N} \vec{\alpha}_i(\vec{\theta}_i), \tag{1.21}$$

where

$$\vec{\theta}_j(\vec{\theta}_1) = \vec{\theta}_1 - \sum_{i=1}^{j-1} \lambda_{ij}\vec{\alpha}_i(\vec{\theta}_i) \tag{1.22}$$

$$\lambda_{ij} = \frac{D_{ij}D_{\rm s}}{D_j D_{\rm is}}, \tag{1.23}$$

and $D_{ij}$ is the angular diameter distance between the $i$-th and $j$-th plane. In particular, $D_{\rm is}$ is the angular diameter distance between the $i$-th plane and the source plane. With respect to Eq. 1.21, the deflection angle in multi-plane cases, $\vec{\alpha}(\vec{\theta}_1)$, is defined as

$$\vec{\alpha}(\vec{\theta}_1) \equiv \sum_{i=1}^{N} \vec{\alpha}_i(\vec{\theta}_i). \tag{1.24}$$

Viewing the simple form of Eq. 1.24, it seems that the deflection angle in multi-plane cases is just a linear combination of the deflection angle of each plane. However, note that the variable on the right is $\vec{\theta}_i$ instead of $\vec{\theta}_1$, which actually incorporates all the complicated non-linear mapping relations between each plane in front of the $i$-th plane.

Following the terms used by Gilman et al. (2019), we define the divergence and curl of the deflection angle in the multi-plane cases to be the "effective" convergence, $\kappa_{\rm eff}$, and "effective" curl, $\zeta_{\rm eff}$, denoted as

$$\kappa_{\rm eff}(\vec{\theta}_1) \equiv \frac{1}{2}\nabla_{\vec{\theta}_1} \cdot \vec{\alpha}(\vec{\theta}_1) \tag{1.25}$$

$$\zeta_{\rm eff}(\vec{\theta}_1) \equiv \frac{1}{2}\nabla_{\vec{\theta}_1} \times \vec{\alpha}(\vec{\theta}_1). \tag{1.26}$$

Because $\vec{\alpha}(\vec{\theta}_1)$ is a two-dimensional vector, the curl of it is a scalar field. A natural question in multi-plane cases is whether we can define a lensing potential, of which

the gradient is the deflection angle. In other words, is $\zeta_{\rm eff}$ still zero in a multi-plane lensing case? For a simple demonstration, we consider the two-plane situation. The effective convergence and effective curl in the two-plane lensing system are

$$\kappa_{\rm eff} = \kappa_1(\vec{\theta}_1) + \kappa_2(\vec{\theta}_2) - \frac{D_{12}D_{\rm s}}{D_2 D_{1\rm s}}\kappa_1(\vec{\theta}_1)\kappa_2(\vec{\theta}_2) \tag{1.27}$$

$$\zeta_{\rm eff} = 2\frac{D_{12}D_{\rm s}}{D_2 D_{1\rm s}}\gamma_1(\vec{\theta}_1)\gamma_2(\vec{\theta}_2)\cos 2\phi_1(\vec{\theta}_1)\cos 2\phi_2(\vec{\theta}_2), \tag{1.28}$$

where we use subscripts 1 and 2 to refer the corresponding quantities of plane 1 and plane 2 respectively. It is clear that $\zeta_{\rm eff}$ is not always zero in the two-plane case, which indicates that theoretically the deflection angle cannot be derived from a single lensing potential. In other words, multi-plane lensing effects cannot be perfectly represented by only one lensing plane. Although $\kappa_{\rm eff}$ cannot capture all the features in multi-plane cases, it is still a meaningful quantity which represents the closest single plane approximation to the mass distribution of line-of-sight objects. For an example, Fig. 1.2 shows the $\kappa_{\rm eff}$ and $\zeta_{\rm eff}$ of a set of small dark matter haloes sampled within the light-cone between the observer and the source galaxy, where the main deflector's deflections have been subtracted*. As shown, though all the input low-mass perturbers should be round, their shapes on the effective convergence map have been stretched into "banana" shapes due to multi-plane lensing effects. Also, we can see that the effective curl map is not always zero though in most regions its value is very small, which confirms our conclusions above.

### 1.2.3 An open-source lensing package: PyAutoLens

PyAutoLens is an open source python package which is designed specifically for strong lensing modelling (Nightingale et al., 2018, Nightingale et al., 2021b)†. Its core feature is automated strong lensing modelling via linking a series of pipelines, that will enable it to analyze the hundreds of thousands strong lensing systems expected to be discovered this decade (Nightingale et al., 2021b, Etherington et al.,

*The image is generated through PyAutoLens, which is introduced Section 1.2.3.
†https://github.com/Jammy2211/PyAutoLens

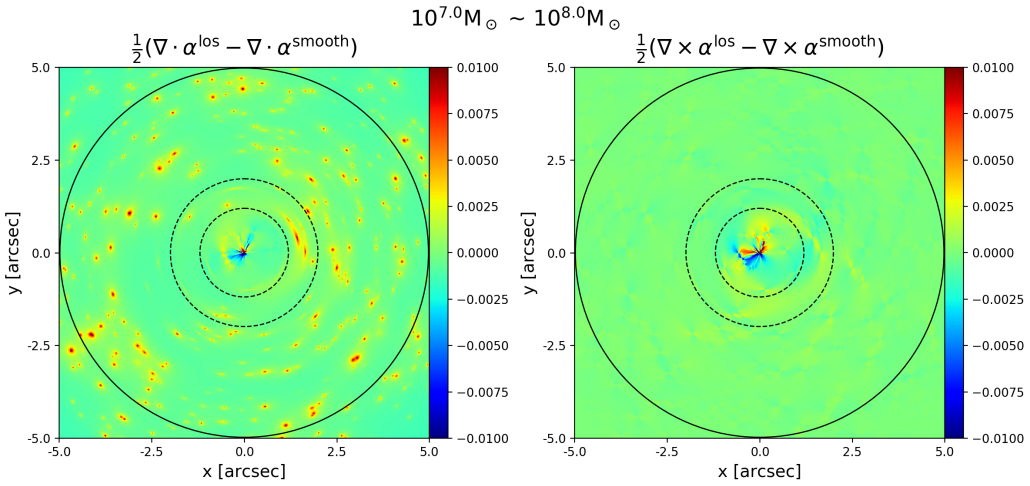


Figure 1.2: The effective convergence (left) and effective curl (right) maps of some low-mass perturbers at multi-planes. The solid circle is the boundary of the light cone.

2022). It can handle both imaging and interferometric data, with specific optimizations to simplify ray-tracing procedures and accelerate computation. To account for the complexity of strong lensing systems, a variety of commonly used analytical and pixelized models for the lens and source are available in the code. Multi-plane ray-tracing is also added, where one can easily set up objects with their redshifts as free parameters. In addition, the parameter fitting process is taken care of by PyAutoLens's sibling package PyAutoFit, which incorporates different parameter sampling methods, such as MCMC, Nested Sampling etc., depending on the different levels of complexity of fitting tasks (Nightingale et al., 2021a). Depending on the sampling package, if possible, PyAutoFit enables distribution of the fitting task over multiple processors, which significantly reduces the time cost especially when complex models are applied. Throughout this work, if not specified, we use PyAutoLens for the lensing related computation, such as simulating, fitting and analyzing.

## 1.3 Strong lensing of low-mass dark matter haloes

So far, studies of the strong lensing of low-mass dark matter haloes can be roughly categorized into two types of analysis depending on source size and the kind of data available.

### 1.3.1 Point-like source

If the source is an extremely compact object, like a quasar, when lensed, one will observe multiple point sources. Low mass "invisible" dark matter haloes along the line of sight induce anomalies in the flux ratios amongst multiple images, and by analysing those anomalies one can constrain the dark matter particle mass (Mao and Schneider, 1998, Metcalf and Madau, 2001, Dalal and Kochanek, 2002, Amara et al., 2006, Xu et al., 2012, Nierenberg et al., 2014, Xu et al., 2015, Nierenberg et al., 2017, Gilman et al., 2019, Hsueh et al., 2020, Gilman et al., 2020a). However, because of the limited amount of information contained in the fluxes and positions of multiple images of a point-like source, there are degeneracies between the smooth model assumed for the lens and the inferred properties of the low-mass perturbing haloes. Also, some differences between the fitted macro model and the true lens mass cannot be constrained due to the limited information, which might affect what one infers about the low-mass perturbers.

### 1.3.2 Extended source

If the source is extended (e.g. an ordinary galaxy), it appears after lensing as multiple arcs or a complete Einstein ring. Sufficiently massive dark matter haloes along the line of sight perturb local regions of the arc in a way that is measurable using techniques such as the pixelized potential correction method (Vegetti et al., 2012, 2014, 2018, Ritondale et al., 2019). However, this explicit subhalo modelling has demanding requirements on image quality and resolution and so far only three

such detections of dark haloes with pseudo-Jaffe* masses below $10^{10}\,M_\odot$ have been made so far: the first was made by Vegetti et al. (2010), who detected a $3.51 \pm 0.15 \times 10^9\,M_\odot$ subhalo using Hubble Space Telescope (HST) imaging; The second was made by Vegetti et al. (2012) via Keck Adaptive Optics, with an inferred mass of $1.9 \pm 0.1 \times 10^8\,M_\odot$; Finally, Hezaveh et al. (2016) found a $9.1 \pm 2.5 \times 10^8\,M_\odot$ subhalo using Atacama Large Millimeter/submillimeter Array (ALMA) interferometric observations.

Attempts to detect dark haloes have been made in approximately 30 lenses (Vegetti et al., 2014, Ritondale et al., 2019), however no other clean signals have been found due to limited data quality. Among those 30 attempts, for some systems significantly improved fits are found when a low-mass perturber is added as part of the fitted model, but a later sanity check reveals these to be "false-positive" signals, which are thought to come from the mismatch in the complexity of model and the actual lens galaxy's mass distribution. It is noted so far most analysis on subhalo lensing are assuming the lens galaxy to be a single elliptical power law (Tessore and Metcalf, 2015) with an external shear, while in reality a galaxy's projected mass distribution is far more complex than a simple power law. Recently Cao et al. (2021) fitted the power law model to strong lenses simulated using mass models derived from dynamical models of nearby SDSS-IV MaNGA (Bundy et al., 2015) early type galaxies and showed this can bias the measurement of the local density slopes around the Einstein ring by 13%. Also, Gomer and Williams (2021) and Van de Vyvere et al. (2022) discuss how departures from elliptical symmetry may affect flux ratio observations in lensed quasars. For the lensing of low-mass perturbers, it remains unclear how much the inferred properties of the low-mass perturber are affected by deviations of the lens from an elliptical power law profile.

*The masses reported are masses of pseudo-Jaffe profiles (Muñoz et al., 2001). If modelled by an NFW, the virial mass obtained is usually $0.5 \sim 1.0$ dex higher than the pseudo-Jaffe mass (Despali and Vegetti, 2017).

### 1.3.3 Sensitivity Mapping

To convert individual detections to constraints on the halo mass function, one needs to derive "sensitivity" maps to combine results for individual haloes in many systems (e.g. Vegetti and Koopmans, 2009a, Li et al., 2016b). To be specific, for one particular strong lensing system, the sensitivity map quantifies the chance of detecting a low-mass perturber at a given position, redshift, mass (and even concentration). The challenge of deriving the sensitivity map exists in fully sampling the huge parameter space of a potential low-mass perturbers, especially when including the dimension of redshift. To overcome it, Li et al. (2017) propose an effective mass, $M_{\rm eff}(M_{\rm los})$, for a line-of-sight halo of mass, $M_{\rm los}$, which is determined by fitting a lensing image perturbed by an NFW halo at the lens redshift to the image perturbed by a line-of-sight halo of mass, $M_{\rm los}$, at redshift, $z_{\rm los}$. In other words, if a subhalo of mass, $M_{\rm eff}(M_{\rm los})$, can be detected, a line-of-sight halo of mass, $M_{\rm los}$, should also be detected. In this way, one can calculate the effective mass function of all perturbers. Li et al. (2017) showed that, for CDM, the number of detectable line-of-sight perturbers is $3-4$ times larger than the number of subhalo perturbers. A similar analysis was performed by (Despali et al., 2018), who derived a fitting formula for $M_{\rm eff}$ by fitting the deflection angle of a lensing system containing a line-of-sight perturber to that of a system containing a subhalo. The analysis was performed for lenses with different image and redshift configurations. In agreement with the results of Li et al. (2017), they found that the contribution from CDM line-of-sight haloes is about 3 times that from subhaloes for lenses with $z_{\rm l} = 0.2$ and $z_{\rm s} = 1.0$, and about 10 times that from subhaloes for lenses with $z_{\rm l} = 0.5$ and $z_{\rm s} = 2.0$. In addition, by statistically studying the perturbations of low mass haloes, Çağan Şengül et al. (2020) also showed that line-of-sight perturbers tend to dominate the signal for systems with a source at redshift $z_{\rm s} = 0.5$ or higher.

## 1.4 Thesis Outline

This thesis focuses on constraining the halo mass function through strong gravitational lensing and trying to solve some of the issues mentioned above. The rest of the thesis is organised as follows: in Chapter 2, we extend the statistical method of extracting abundance information of dark haloes from point-like source case to the case of extended sources, where in principle degeneracy between macro model and an ensemble of low-mass perturbers could be largely broken; In Chapter 3, we revisit the topic of sensitivity mapping used to convert individual low-mass perturber detections into constraints on the halo mass function. We investigate previous ways of approximating lensing effects of line-of-sight low-mass perturbers as one on the lens plane and give new estimations on the relative detectability of line-of-sight versus on-plane low-mass perturbers; In Chapter 4, we come back to the long-term existing question on how a galaxy's complexity beyond a single elliptical power would affect the inference on the detections of low-mass perturbers. In the work, we build up mock strong lensing systems with lens galaxies from hydrodynamical simulations and test two kinds of lens mass models, an elliptical power law model and a stellar-dark matter two component model. Finally, in Chapter 5, we summarize our results and discuss on some future work.

Chapter 2

# A forward-modelling method to infer the dark matter particle mass from strong gravitational lenses

**Abstract**

A fundamental prediction of the cold dark matter model of structure formation is the existence of a vast population of dark matter haloes extending to sub-solar masses. By contrast, other dark matter models, such as a warm thermal relic, predict a cutoff in the mass function at a mass which, for popular models, lies approximately between $10^7$ and $10^{10}$ $M_\odot$. We use mock observations to demonstrate the viability of a forward modelling approach to extract information about low-mass dark haloes lying along the line-of-sight to galaxy-galaxy strong lenses. This can be used to constrain the mass of a thermal relic dark matter particle, $m_{\rm DM}$. With 50 strong lenses at HST resolution and a maximum pixel signal-to-noise ratio of $\sim 50$, the expected median $2\sigma$ constraint for a CDM-like model (with a halo mass cutoff at $10^7$ $M_\odot$) is $m_{\rm DM} > 4.10\,{\rm keV}$ (50% chance of constraining $m_{\rm DM}$ to be better than 4.10 keV). If, however, the dark matter is a warm particle of $m_{\rm DM} = 2.2\,{\rm keV}$, our 'Approximate Bayesian Computation' method would result in a median estimate of $m_{\rm DM}$ between 1.43 and 3.21 keV. Our method can be extended to the large samples of strong lenses that will be observed by future telescopes, and could potentially rule

out the standard CDM model of cosmogony. To aid future survey design, we quantify how these constraints will depend on data quality (spatial resolution and integration time) as well as on the lensing geometry (source and lens redshifts).

## 2.1 Introduction

A key difference between cold and warm dark matter models can be found in the smallest haloes each can produce. Strong gravitational lensing provides a good way to detect and measure these small haloes. As mentioned in Section 1.3, depending on the type of strong lensing data, there are two different methods: a statistical method for extracting information from flux ratio anomalies of lensed quasars about ensembles of low-mass dark matter haloes; an explicit modelling of low-mass haloes based on images of strongly lensed (regular) galaxies. There are advantages and disadvantages to both methods: a flux ratio anomalies analysis may suffer from the degeneracy between the macro model considered and the abundance of low-mass dark matter halos due to the limited amount of information available in the data; The explicit modelling method has a high requirement for the quality of an image and can be time-consuming when searching for multiple small haloes.

Recent studies have proposed that it is also possible to extract, statistically, the cumulative perturbation of all intervening haloes on extended lensing arcs, even though none of these haloes could be detected individually (Brewer et al., 2016). This approach can be viewed at some level as a combination of the two types of methods described above. So far, most studies in this direction have focused on determining a theoretical relation between the power spectrum of the distribution of low-mass haloes and the image residuals after fitting a smooth "macro model" to the lens galaxy mass distribution (Chatterjee and Koopmans, 2018, Díaz Rivero et al., 2018, Cyr-Racine et al., 2019). There is one example using real data, in which Bayer et al. (2018) analysed image residuals of the system SDSSJ0252+0039, ob-

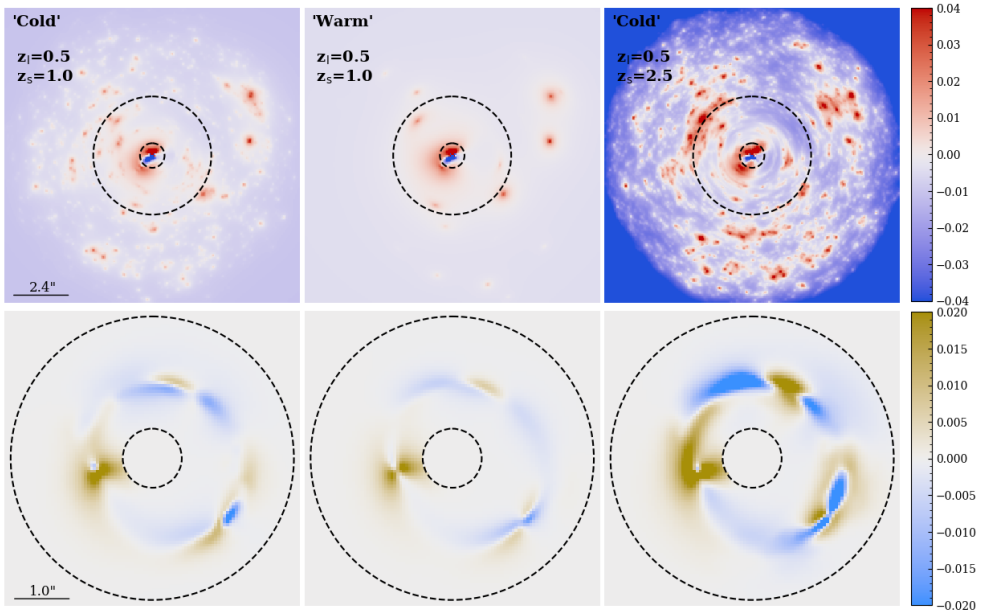


Figure 2.1: Upper panels: the effective convergence of low mass perturbers. Lower panels: the corresponding best-fit image residuals. The colour scale is in units of $e^-$ $pix^{-1}$ $s^{-1}$. The parameters of the lens and source galaxies of the three columns are the same except for the source redshift. The lensing systems in the left and middle columns have a source at $z = 1$, while that in the right column has a source at $z = 2.5$. The systems in both the left and right columns have a cutoff in the mass function at $10^7$ $M_\odot$, while the one in middle column has the cutoff at $10^9$ $M_\odot$. The inner and outer dashed circles in each panel have radii, $0.5''$ and $2.4''$, respectively.

taining a detection of power much higher than the prediction of the CDM model. There remain a number of questions as to what assumptions are appropriate for this technique. For example, to simplify the theoretical calculations, a random Gaussian field is often assumed for the convergence of low-mass perturbers, potentially omitting multiplane lensing effects (Schneider, 2014, McCully et al., 2014). Indeed, recent studies have shown that the expected signal in a ΛCDM universe is dominated by line-of-sight haloes at different redshifts to the lens galaxy as opposed to subhaloes within the lens galaxy itself (Li et al., 2016b, 2017, Despali et al., 2018, Çağan Şengül et al., 2020). Here, we will focus on how the line-of-sight low mass dark matter haloes contribute to perturbations on lensing images.

To form a visual impression of how the line-of-sight low-mass dark haloes perturb

the images, in Fig. 2.1 we show the effective convergence (defined in Section 1.2.2), as derived from the deflection angles (upper panels; Gilman et al., 2019, Çağan Şengül et al., 2020), and the corresponding residuals obtained by fitting the smooth lensing model to the image (lower panels). As may be seen from the effective convergence map, even though all low-mass dark matter haloes are modelled as spherical profiles, some are heavily stretched into arc-like features due to multiplane lensing effects*, which are difficult to compute analytically. Comparing the left two columns, the "warm" case in the middle and the "cold" case in the left have very similar residuals, particularly the large patches, even though the warm case has far fewer low-mass dark matter haloes. This suggests that the residuals are dominated by massive dark matter haloes and to distinguish between different dark matter models, we need to identify the small patches. The system shown in the third column has a higher redshift source and thus many more low-mass dark matter haloes along the line-of-sight, which results in larger and more complicated residuals.

In this chapter, we investigate whether a forward modeling procedure built around the Approximate Bayesian Computation (ABC) statistical inference method can extract meaningful information about the properties of low-mass dark matter haloes perturbing strong lensing images. As opposed to determining a concise mathematical expression, our forward modelling method relies on robust modelling of the perturbations on lensing images induced by small dark haloes which can directly build up a relation between the models of interest and the observations without any further assumptions. The approach was first applied to strong lensing by Birrer et al. (2017a) who analysed the strongly lensed quasar RXJ1131-1231. Subsequently, Gilman et al. (2019) used this approach to study flux ratio anomalies of point-like sources with a full realisation of dark matter haloes including line-of-sight dark haloes.

*In strong lensing, as viewed from the image plane, not only is the distant light warped by foreground objects, like a luminous source galaxy deflected by a lens, but also the mass on distant planes is warped by near planes, and thus we see some arc-like low-mass dark matter haloes in these convergence maps even though they are all spherical.

We apply the ABC framework to a simulated sample of 50 HST-resolution strongly lensed extended sources, which is a comparable number of lenses to the high-quality strong lensing SLACS sample (Bolton et al., 2006, but the details of our sample are different from those of SLACS). Each simulation contains a full cosmological realisation of small dark haloes whose redshift distribution requires analysis using multiplane ray tracing. To apply the ABC method we simulate and refit each of these 50 lenses 20 000 times, producing a total of 1 million lens models. The scale of this analysis necessitates an automated framework for lens modelling, for which we use the open source software PyAutoLens. We aim to determine whether the cumulative distortions due to the many dark matter haloes perturbing the light of the lensing arcs can be extracted to determine the halo mass function and hence the dark matter particle mass. Our main goal is to demonstrate that this signal is present in HST imaging of strong lenses and that it can, in principle, be extracted using modern lens modeling techniques given realistic levels of noise. However, our study is based on idealized systems: we make a number of simplifying assumptions for the structure of the lens and source and neglect effects such as an imperfect PSF (point spread function) model, correlated noise or inadequate lens light subtraction. These assumptions will need to be relaxed before our methodology can reliably be applied to real data, including, for example, a non-parametric source model (e.g. Warren and Dye, 2003), additional complexity in the lens model (Vegetti and Koopmans, 2009a, Nightingale et al., 2019) and a proper treatment of the PSF and of correlated noise.

We first introduce the forward modelling procedure and lensing models in Section 2.2. In Section 2.3 we show tests of the accuracy of this method, the dependency on different lensing and observational settings, and compare our method to other methods, discussing its possible future applications and shortcomings. Finally, we conclude in Section 2.4. Throughout this chapter, we adopt the cosmological parameters given by WMAP9 (Hinshaw et al., 2013).

## 2.2 Procedure and models

In this section we first provide an overview of our forward modelling procedure. We then describe the parametric models we use for the mass distributions of the main lens, dark matter haloes and light distributions of the source galaxies. We then describe how we fit our simulated images with a combination of a smooth parametric lens and source model, and how the residuals of each are used within an ABC framework to place constraints on the mass function of dark matter haloes.

### 2.2.1 The forward modelling scheme

In Fig. 2.2, we provide an overview of the forward modelling procedure. Starting from an observed strong lensing image (which in this chapter is simulated) we begin by fitting it with parametric lens and source models, omitting substructure from the lens model. This procedure gives us best-fit smooth lens mass and source light models, as well as a map of the best-fit image residuals (the observed image minus the best-fit model image). In this chapter, "best-fit" refers to the maximum likelihood model determined by means of a non-linear search.

It is impossible to fit all the dark matter substructure in a similar way, because of its low mass and low signal-to-noise (Birrer et al., 2017a). However, we can use the best-fit source and macroscopic lens model to simulate a set of images of this lens system, each including a random realization of dark matter substructure (we call this set of images the "forward models"). We refit each forward model in the same manner as we fitted the "observed" image, providing best-fit image residuals for each forward model. We compare the forward-modelled residuals with the observed residuals, as described in detail in Section 2.2.2, and apply ABC inference to obtain a constraint on the cutoff in the halo mass function.

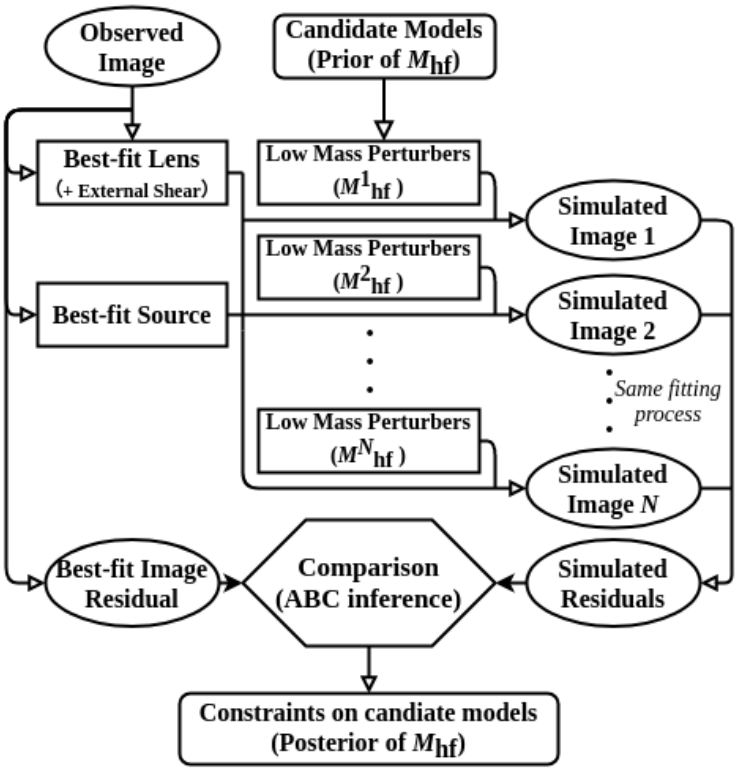


Figure 2.2: An overview of the forward modelling procedure for one lensing system. The observed image is fitted with a parametric lens mass model and a parametric source light model, producing a best-fit lens model, source model and image residuals. We use this best-fit model to generate $N$ simulated images, including random realisations of low-mass perturbing haloes in the lens model. The number of perturbers as a function of mass depends on the properties of the dark matter as encoded in the "half-mode mass", $M_{\rm hf}$. The distribution of $M_{\rm hf}$ over the $N$ "forward models" follows our prior on $M_{\rm hf}$. Each of the forward model images is fit in the same way as the observed image to produce $N$ sets of image residuals. These forward model residuals are compared with the observed residuals, using ABC to constrain $M_{\rm hf}$.

### 2.2.2 Lensing simulations

The strong lens simulations used in this chapter represent the lensing system with three components, the lens galaxy, the source galaxy, and the line-of-sight dark matter haloes.

#### 2.2.2.1 Lens and source

We simulate the smooth mass distribution of our lens galaxy as a 2D singular isothermal ellipsoid (SIE) of the form,

$$\begin{aligned} \Sigma(x,y) &= \frac{\sigma^2}{2\mathrm{G}} \frac{1}{\sqrt{x^2 q + y^2/q}} \\ &= \frac{\mathrm{c}^2}{8\pi\mathrm{G}} \frac{D_{\mathrm{A}}(0,\ z_{\mathrm{source}})}{D_{\mathrm{A}}(z_{\mathrm{lens}},\ z_{\mathrm{source}}) D_{\mathrm{A}}(0,\ z_{\mathrm{lens}})} \frac{R_{\mathrm{E}}}{\sqrt{x^2 q + y^2/q}} \end{aligned} , \tag{2.1}$$

where $R_{\mathrm{E}}$ is the projected Einstein radius, which can be related to the velocity dispersion of the profile, $\sigma$, given the lens and source redshifts ($z_{\mathrm{lens}}$ and $z_{\mathrm{source}}$, respectively) and a cosmology. The quantity, $D_{\mathrm{A}}\left(z_1, z_2\right)$, is the angular diameter distance between $z_1$ and $z_2$; $q$ is the axis ratio. For simplicity, we do not add any external shear to our mock observations. However, we include an external shear when modelling the lenses.

For the source, we adopt the Sérsic (1963) profile,

$$I(r) = I^{'} \exp\left[-b_n \left(\frac{r}{r_{\mathrm{e}}}\right)^{1/n}\right], \tag{2.2}$$

where $I^{'}$ is the scale intensity, $n$ is the Sersic index and $b_n$ is a function of $n$ defined such that $r_{\mathrm{e}}$ is the half-light radius. It is noted that the image residuals caused by small perturbations to the lens model (in our case the perturbing haloes) are effectively a product of the deflection angles due to the perturbation and the gradient of the source surface brightness (Vegetti and Koopmans, 2009a). The cuspy centre of the Sérsic profile creates an infinite surface brightness gradient which numerically causes infinite surface brightness differences. This can be overcome by oversampling the source light, but at the expense of increased computational run

time. Instead, we use a Sérsic profile with a "core" (Graham et al., 2003, Trujillo et al., 2004) to simulate the background source. This has the form,

$$I(r) = I^{'} \exp\left[-b_n \left(\frac{r^{\alpha} + r_{\rm c}^{\alpha}}{r_{\rm e}^{\alpha}}\right)^{1/(n\alpha)}\right], \tag{2.3}$$

where $r_c$ is the "core radius", which marks the transition radius from the Sérsic profile to constant surface brightness. When $r_c \to 0$, the profile reduces to the Sérsic form. The parameter, $\alpha$, quantifies how quickly the profile transitions from a regular Sérsic form to one with a constant surface brightness core. To simplify both our simulation and modelling processes, we fix $\alpha = 2$ and $r_{\rm c} = 0.01''$. With these parameters fixed, the source model has the same three free parameters as the regular Sérsic profile: $r_{\rm e}$, $n$ and $I^{'}$.

#### 2.2.2.2 Low-mass dark matter haloes

Low-mass dark matter haloes that can perturb lensing arcs can be of two types: subhaloes within the main lens, or central haloes at different redshifts that happen to lie close to the path of light from the source galaxy to the observer. We will refer to the latter as line-of-sight haloes.

The number and mass distribution of subhaloes within the lens are somewhat uncertain. Subhaloes are subject to tidal stripping and disruption; these effects are significantly enhanced in hydrodynamic simulations compared to dark matter only simulations due to the presence of the dense stellar component at the centre of the main lens (Sawala et al., 2017, Garrison-Kimmel et al., 2017, Richings et al., 2021). The degree of disruption also depends on the details of the galaxy formation model (Richings et al., 2020). In contrast, line-of-sight haloes are not subject to these environmental effects and, in the mass range of interest here, they are entirely "dark", having never formed stars.

Recent studies (Li et al., 2016b, 2017, Despali and Vegetti, 2017, Çağan Şengül et al., 2020) have shown that for the lens and source redshifts typical of SLACS lenses (Bolton et al., 2006), the lensing perturbations mainly arise from line-of-sight

haloes. This is fortunate because the irrelevance of uncertain baryon effects, makes line-of-sight haloes a particularly clean probe of a cutoff scale in the halo mass function. In this chapter, we focus on these low-mass line-of-sight haloes whose mass function is given by Eq. 1.3, where the CDM mass function, $F_{\rm CDM}\,(M_{200}, z)$, is taken as the one from Sheth et al. (2001).

We draw low-mass dark haloes in a lightcone between the observer and the source galaxy within an angular radius, $r_{\rm lc}$, chosen as,

$$r_{\rm lc} = \begin{cases} 5.0'' & (z \leq z_{\rm lens}) \\ 5.0'' - 2.0'' \times \frac{D_{\rm A}(z_{\rm lens},\, z) D_{\rm A}(0,\, z_{\rm source})}{D_{\rm A}(0,\, z) D_{\rm A}(z_{\rm lens},\, z_{\rm source})} & (z > z_{\rm lens}) \end{cases}, \tag{2.4}$$

where $D_A$ is the angular-diameter distance and $z_{\rm lens}$ and $z_{\rm source}$ are the redshifts of the lens and source galaxies respectively. The angular radius of the lightcone is fixed at $5.0''$ (this is $\sim 3$ times the Einstein radius, and including haloes at larger radii hardly affects our lensing images) in front of the main lens and gradually decreases behind from $5.0''$ to $3.0''$ at the source redshift, which ensures that all perturbers that might influence the lensed image of the source are included. The lightcone is evenly divided into redshift bins, of width $\Delta z = 0.01$, which balances the accuracy and computational cost of the calculation (see Appendix A for details). Within each bin, we sample from the halo mass function, assign density profiles from the halo mass-concentration relation corresponding to that redshift, and place these perturbing haloes randomly on the central redshift plane. Neglecting the clustering of the line-of-sight haloes is a good approximation if, over the angular extent of interest, the typical line-of-sight separation of pairs of haloes is much larger than their correlation length. This is expected to be true because: (a) the intrinsic clustering of low mass haloes is weak (Kaiser, 1984, Sheth and Tormen, 1999), and (b) the angular extent of interest is very narrow since it is set by the width of the Einstein ring image.

We generate low-mass haloes with $M_{200}$ between $10^6$ $\rm M_\odot$ and $10^{10}$ $\rm M_\odot$ within the light cone. Depending on the dark matter model, a significant fraction of the mass in the Universe can exist as collapsed objects in this mass range. To solve correctly

the strong lensing equations (which have already assumed a background universe) we add negative mass sheets onto each plane to compensate for the otherwise "double-counted" mass within perturbers in the lightcone (Petkova et al., 2014, Birrer et al., 2017b, Gilman et al., 2019). For each plane, we include a mass sheet with constant negative surface density equal to the expected density in low-mass haloes on that plane. This leads to a mass sheet with a surface density

$$\Sigma_{\rm negative} = -\frac{1}{A}\int F(M_{200}, z) M(M_{200}, z, s)\ {\rm d}M_{200}{\rm d}s\ {\rm d}V, \tag{2.5}$$

where $A$ is the physical area of the lightcone at the plane's redshift, $F(M_{200}, z)$ is the mass function and $M(M_{200}, z, s)$ is the total mass of a dark halo on the plane, which can differ from $M_{200}$ due to halo truncation. The "s" denotes some other parameters of the dark matter profile; in our case, as we discuss below, it represents the "concentration" and "truncation radius".

To ensure a finite mass for each input low-mass halo, instead of modelling haloes as NFW profiles (Navarro et al., 1996, 1997), we use tNFW profile given by Eq. 1.8 with $n = 1$. To simplify the parameterization, we also set the truncation radius to be the corresponding NFW's $r_{100}$, the radius within which the average density of an NFW profile is 100 times the critical density of the universe. With the truncation radius fixed, the tNFW profiles are determined by the same two parameters as the NFW profile, $M_{200}$ and the concentration, $c$. To further simplify the parameterization, we assume $M_{200}$ and $c$ follow the mass-concentration relation given by Ludlow et al. (2016) in the CDM case, and the relation in a WDM case is then modified as Eq. 1.7. We use the public package COLOSSUS (Diemer, 2018) to compute the mass-concentration relation in the CDM case. To fully capture the distribution of those low-mass haloes, we further include log-normal scatter in the mass-concentration relation, with a standard deviation of 0.15 dex.

Multi-plane ray tracing is necessary to calculate the effect of line-of-sight haloes on flux ratio anomalies with sufficient precision to match observations (Gilman et al., 2019). We use PyAutoLens to simulate lenses using the light and mass profiles

described above. To define our fiducial lens sample, we simulate 50 unique lensing systems with different values for the lens SIE mass model (e.g. Einstein radius, axis ratio, etc.) and source core-Sersic profile. The input $M_{\rm hf}$ is $10^7$ $M_\odot$. For all 50 systems we assume lens redshifts of 0.5 and source redshifts of 1.

We produce observations representative of HST imaging, with a pixel size of 0.05″, a Gaussian PSF with a standard deviation of 0.05″ and background sky level of $1e^-$/pix/second. We set the exposure time to be 600 s. The source surface brightness of each simulation is chosen such that the maximum signal-to-noise ratio (e.g. in the brightest pixel) has a value $\sim 50$. Table 2.1 summarizes the models and parameters for our mock observations, where closed brackets indicate the range of values from which each parameter is randomly drawn. For convenience, we use $\{T\}_{\rm fiducial}$ to denote the set of true parameter values used for our fiducial tests and a superscript $i$ to represent the parameters of the $i$-th lensing system. Mock images of our 50 strong lensing systems are shown in Fig. 2.3.

### 2.2.3 Analysis Process

Our analysis of each mock observation consists of two steps: smooth model fitting followed by ABC inference. Below we describe the detailed steps in this process and illustrate them for one system.

#### 2.2.3.1 Smooth Model Fitting

First, we fit a simple lens model to the mock lensing image. This consists of a smooth parametric model plus an external shear for the lens galaxy mass distribution (the *macro model*) and a smooth parametric model for the source. We adopt the same parametric forms we used when generating the simulated mock image, an SIE lens mass model and a core-Sérsic source.

We use PyAutoLens to fit the mock images, and adopt PyMultiNest with constant sampling efficiency mode switched on (Feroz et al., 2009, Buchner et al.,

| Parameter | Range or Value |
|---|---|
| **Lens** | Elliptical Isothermal |
| centre (x, y) [″] | (0.0, 0.0) |
| $R_{\rm E}$ [″] | [1.2, 1.6] |
| axis ratio | [0.6, 0.95] |
| position angle [°] | 30 |
| redshift | 0.5 |
| **External Shear** | |
| magnitude $A$ | 0 |
| position angle [°] | 0 |
| **Source** | Elliptical Core-Sersic |
| centre (x, y) [″] | ([−0.3, 0.3], [−0.3, 0.3]) |
| $\rm r_e$ [″] | [0.1, 0.5] |
| n | [1.5, 2.5] |
| $\rm I^{'}$ [$\rm e^{-}$ $\rm pix^{-1}$ $\rm s^{-1}$] | 7.4 |
| axis ratio | [0.5, 0.95] |
| position angle [°] | [10, 100] |
| $\rm r_c$ [″] | 0.01 |
| $\alpha$ | 2.0 |
| $\gamma$ | 0.0 |
| redshift | 1.0 |
| **Dark haloes** | Truncated NFW profile |
| $F_{\rm CDM}$ | Sheth et al. (2001) |
| $c_{\rm CDM}$ | Ludlow et al. (2016) |
| $\sigma_{\log_{10}\ \rm c_{CDM}}$ | 0.15 dex |
| tNFW $\tau$ | $r_{100}/r_{\rm s}$ |
| $\rm M_{hf}$ [$\rm M_\odot$] | $10^7$ |
| **Image** | |
| pixel size [″] | 0.05 |
| PSF $\sigma$ [″] | 0.05 |
| $\rm t_{exp}$ [s] | 600 |
| background sky [$\rm e^{-}$ $\rm pix^{-1}$ $\rm s^{-1}$] | 1.0 |
| max S/N of pixels | $\sim 50$ |

Table 2.1: Fiducial model parameters. Closed brackets indicate the range from which values are randomly drawn.

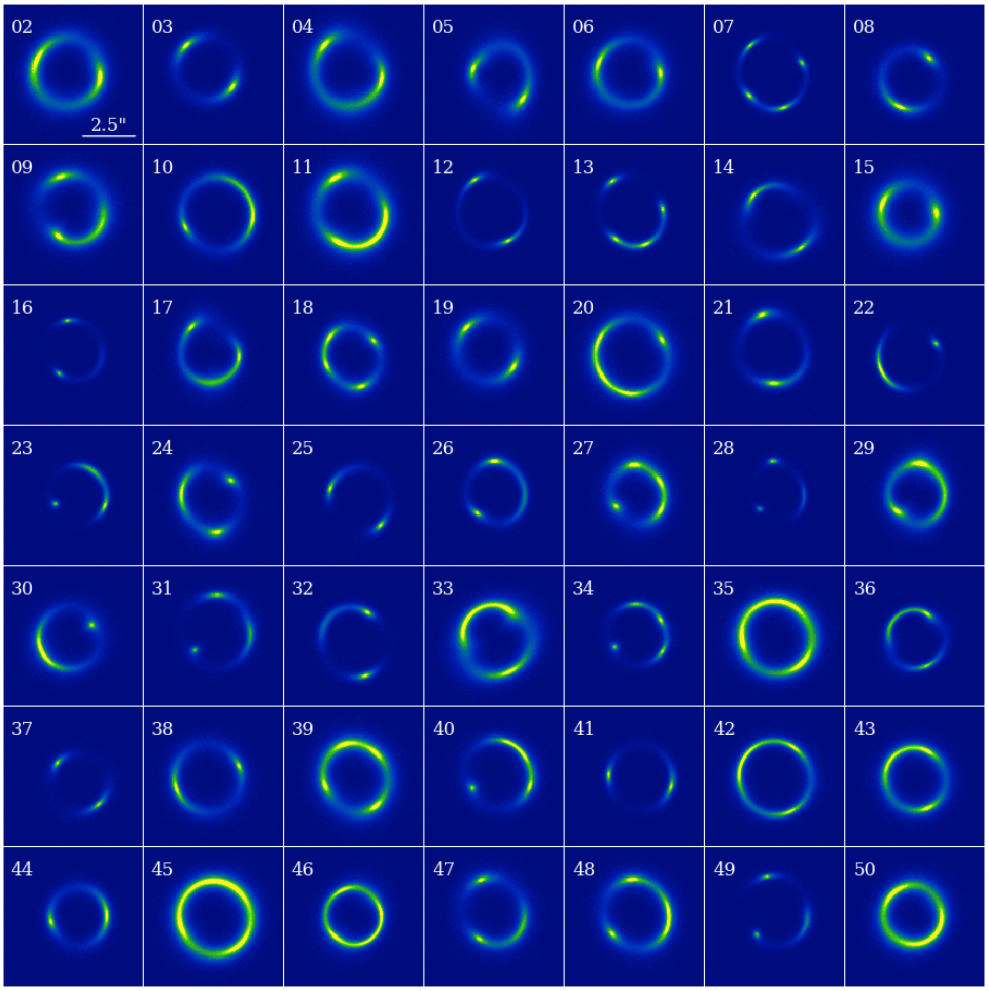


Figure 2.3: Fiducial mock strong lensing images. A total of 49 mock images are shown, with the last of our set of 50 shown in the upper panel of Fig. 2.4. The images are simulated with parameters randomly drawn according to Table 2.1.

2014) for the non-linear optimisation. Table 2.2 shows the inferred parameters for this fit, alongside the true input values for the first mock image. To distinguish between the true inputs and the best-fit values we label the latter as $\{F\}^{i}_{\rm fiducial}$, where a superscript, $i$, denotes the best-fit parameters for the $i$-th lensing system. This table shows that the inferred and input lens model are close, but not in perfect agreement; this is due to the effects of the low-mass dark matter haloes. We will show later that this small mismatch does not affect our calculation.

In the upper and lower panels of Fig. 2.4 we show the "observed" image and best-

| | $\{T\}^1_{\rm fiducial}$ | $\{F\}^1_{\rm fiducial}$ |
|---|---|---|
| **Lens** | Elliptical Isothermal | |
| centre (x, y) [″] | (0.0, 0.0) | $(-0.001^{+0.002}_{-0.002}, -0.001^{+0.003}_{-0.003})$ |
| $R_{\rm E}$ [″] | 1.342 | $1.342^{+0.002}_{-0.003}$ |
| axis ratio | 0.618 | $0.617^{+0.005}_{-0.005}$ |
| position angle [°] | 30.0 | $30.0^{+0.4}_{-0.4}$ |
| **External Shear** | | |
| magnitude | 0 | $0.002^{+0.002}_{-0.002}$ |
| position angle [°] | 0 | $159^{+37}_{-41}$ |
| **Source** | Elliptical Core-Sersic | |
| centre (x, y) [″] | $(-0.072, 0.259)$ | $(0.071^{+0.001}_{-0.001}, 0.253^{+0.001}_{-0.001})$ |
| $r_{\rm e}$ [″] | 0.244 | $0.240^{+0.005}_{-0.004}$ |
| $n$ | 1.85 | $1.81^{+0.05}_{-0.05}$ |
| $I^{'}$ [$e^-$ $pix^{-1}$ $s^{-1}$] | 7.4 | $7.3^{+0.2}_{-0.2}$ |
| axis ratio | 0.85 | $0.85^{+0.01}_{-0.01}$ |
| position angle [°] | 41 | $40^{+2}_{-2}$ |

Table 2.2: The true input and best-fit parameters for the first lensing system. The errors listed in this table are 3-$\sigma$ limits. Notice that we fit a system with additional low-mass perturbers, and thus the inconsistency of the best-fit parameters and the true values is expected. Parameters fixed during fitting are not shown here.

fit residuals for one of our 50 mock observations. To develop intuition on how the low-mass perturbers affect the image residuals, we further show the "effective convergence" of low mass perturbers and the corresponding best-fit residuals in Fig. 2.1. We assume a very small constant noise to show the residuals clearly. The three strong lensing systems shown have the same lens and source galaxy as in Fig. 2.4, except that the source for the system of the right-hand column is at $z = 2.5$. For a clear comparison, we make sure that the three systems share the same realisation of low mass perturbers. To achieve this, instead of applying the mass function described by $M_{\rm hf}$ in Eq. 1.3, we draw haloes from the mass function of Sheth et al. (2001) but discard those with $M_{200}$ below a certain value. Furthermore, we assume no correlation between $M_{\rm hf}$ and the mass-concentration

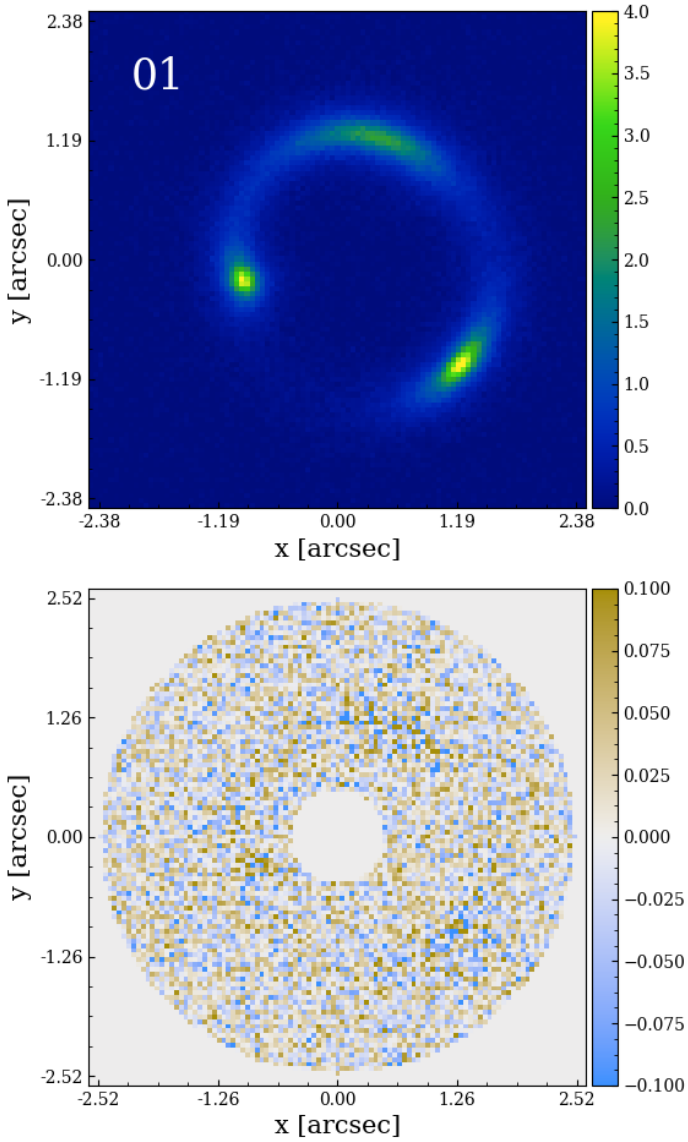


Figure 2.4: Upper panel: the mock image of the first system. Lower panel: the corresponding residuals after fitting a smooth macro model.

relation. Please note that this change of low-mass perturber realisation is only implemented for Fig. 2.1; in the rest of this chapter, we use the mass function and mass-concentration relation described by Eq. 1.3 and Eq. 1.7 respectively.

In Fig. 2.1, the systems in the left and right columns have a cutoff in the mass function at $10^7$ $M_\odot$, while the system in the middle column has a cutoff at $10^9$ $M_\odot$. As seen from the left two columns, the system with a lower cutoff in the mass function has far more low-mass perturbers and thus more subtle structure

in the residuals. When comparing the left and the right columns, we see that the number of low-mass perturbers increases significantly with the source redshift and the "profiles" of individual perturbers are more heavily distorted because of the multi-plane lensing effect. Also, for a higher redshift source galaxy, the residuals are larger.

#### 2.2.3.2 ABC inference through forward modelling

Approximate Bayesian Computation (ABC) is a likelihood-free method suitable for problems where the likelihood is difficult to express analytically, but model predictions are relatively easy to simulate. It has been widely applied in astrophysics, for example in studies of large-scale structure, planet surveys and reionization (Akeret et al., 2015, Hahn et al., 2017, Davies et al., 2018, Hsu et al., 2020). Birrer et al. (2017a), Gilman et al. (2019, 2020a,c) and Enzi et al. (2020) have also used ABC to constrain dark matter substructure using strong lensing data. To begin, one defines a summary statistic which measures the similarity between the observational data and the simulations. In principle, any statistic (as long as it contains information of interest) can be used as a measure of similarity, but different statistics may have different requirements on data quality, sampling efficiency, etc. A good statistic captures as much of the characteristic information of different models as possible: in our case, the lensing perturbations from low-mass dark matter haloes. Finding a proper summary statistic is a challenging part of ABC and it is beyond the scope of this chapter to investigate the many possible candidate summary statistics. Instead, following Bayer et al. (2018), we use the power spectrum of the best-fit image residuals to construct a summary statistic that we hope can extract information on the number of low-mass dark matter haloes perturbing the lens.

Based on the best-fit source and macro model for the lens, $\{F\}^1_{\rm fiducial}$, we simulate images of this best-fit source and lens combination with the addition of low-mass haloes along the line-of-sight. We uniformly sample $\log_{10} M_{\rm hf}/{\rm M}_\odot$ between 7 and 10 (corresponding to assuming a flat prior on $\log_{10} M_{\rm hf}$ between $10^7$ $\rm M_\odot$ and $10^{10}$ $\rm M_\odot$)

and, for each sampled $M_{\rm hf}$ value, we draw a random realisation of low-mass dark matter haloes with the appropriate mass function and mass-concentration relation. We do this for 20,000 values of $M_{\rm hf}$, producing a corresponding lensed image in each case and then fit each of these 20,000 images to obtain the best-fit image residuals. We have confirmed that our results are converged with 20,000 samples. Note that the forward-modelled images are simulated from the known lens and source galaxies, so when performing the fitting, we add narrow priors centred on the parameter values of the known best-fit lens and source models to accelerate the fitting processes. Since our only goal is to find the maximum likelihood model, once our priors contain the correct solution, the size of the priors does not affect our results. In Table 2.3, we summarize the type and size of the priors we used for the fitting processes. To make sure the priors we take are broad enough to find the maximum likelihood model, we fit 4000 different realisations with both the listed priors and 5 times larger priors and then compare the maximum likelihoods obtained. Here, "5 times larger priors" means that for the priors listed in Table 2.3, if it is a Gaussian prior, then the sigma is taken 5 times larger than the value listed. In Fig. 2.5, we show the histogram of the difference of the log maximum likelihood. As shown, the log maximum likelihood results of larger and smaller priors are very close with only $\sim 1.0$ difference, which verifies that the priors we take are broad enough to contain the maximum likelihood model.

Next, for the images of the best-fit residuals, we set pixels outside the annular region between $0.5''$ and $2.4''$ to be 0 and then Fourier transform the residual image and azimuthally average to obtain the 1-D power spectrum, $P(k)$. In the upper panel of Fig. 2.6, we show power spectra for the forward-modelled residuals as black lines (for clarity we only plot 100 of them); the red curve marks the power spectrum of the image residuals of the original observation. Each line is composed of 15 $P(k_i)$ values with the $k_i$ logarithmically spaced between $\sim 1.5$ arcsec$^{-1}$ and 85 arcsec$^{-1}$ ($\sim 2\pi$ / (4.2 arcsec) to $2\pi$ / (0.07 arcsec)).

Although we have converted the images into power spectra, we cannot simply

| | Prior |
|---|---|
| **Lens** | Elliptical Isothermal |
| centre (x, y) [″] | G(input, 0.01) |
| $R_{\rm E}$ [″] | G(input, 0.008) |
| axis ratio | G(input, 0.03) |
| position angle [°] | G(input, 2.0) |
| **External Shear** | |
| magnitude | G(0.0, 0.05) |
| position angle [°] | U(0.0, 180.0) |
| **Source** | Elliptical Core-Sersic |
| centre (x, y) [″] | G(input, 0.01) |
| $r_{\rm e}$ [″] | G(input, 0.015 × input) |
| $n$ | G(input, 0.1) |
| $I^{'}$ [e$^-$ pix$^{-1}$ s$^{-1}$] | G(input, 0.16 × input) |
| axis ratio | G(input, 0.02) |
| position angle [°] | G(input, 2.0) |

Table 2.3: Priors used in fitting processes. G$(a, b)$ represents a Gaussian prior centering on $a$ with standard deviation $b$. U$(a, b)$ represents a uniform prior between $a$ and $b$. The "input" here refers to the corresponding input value used when simulating the mock image.

use the 1D "power spectrum" as our statistic. The reason is that each power spectrum is composed of 15 different values and for ABC to converge at a point in a 15-dimensional space, a very small acceptance rate must be set, which, in turn, requires far more forward models. To further reduce the "dimensionality" of the statistic, following Fearnhead and Prangle (2012), we generate a summary statistic from a linear combination of the logarithm of the power spectrum values at different $k$,

$$\log_{10}\widehat{M}_{\rm hf} = \sum_{i=1}^{15} \beta_i \log_{10}\left[P(k_i)/\mathrm{arcsec}^2\right] + \beta_0. \tag{2.6}$$

We use $\log_{10}\widehat{M}_{\rm hf}$ as the summary statistic for the ABC inference. The coefficients $\{\beta_i\}$ (including $\beta_0$) are obtained by minimizing the differences between the input

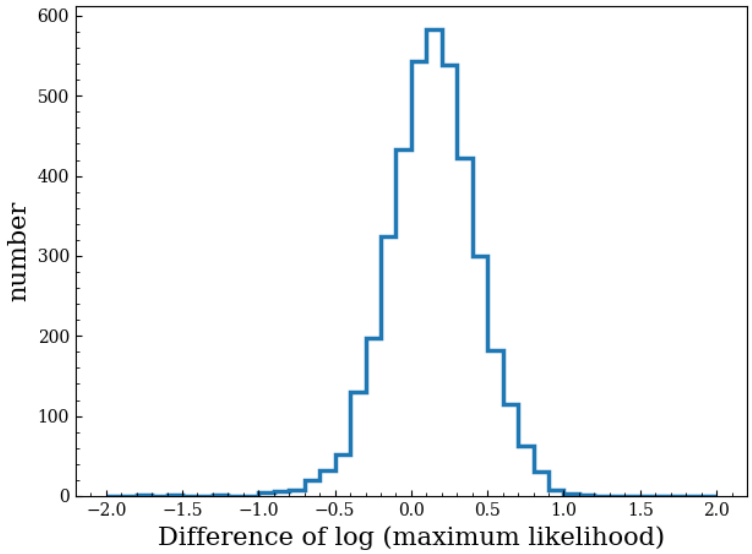


Figure 2.5: Histogram of the differences between the log maximum likelihood obtained with the priors listed in Table 2.3 and that obtained with 5 times larger priors.

$\log_{10} M_{\rm hf}$ values used in the forward models and their corresponding $\log_{10}\widehat{M}_{\rm hf}$. Specifically, we find the values of $\{\beta_i\}$ that minimise,

$$\sum_{j=1}^{20000} \left\| \log_{10}\widehat{M}_{\rm hf}^{(j)} - \log_{10} M_{\rm hf}^{(j)} \right\|^2 , \tag{2.7}$$

where $\log_{10}\widehat{M}_{\rm hf}^{(j)}$ is computed from the $j$-th forward-modelled power spectrum and $M_{\rm hf}^{(j)}$ is the corresponding input half-mode mass. Since the forward-modelled power spectrum is systematically different for different macro lensing configurations, we optimize $\{\beta_i\}$ separately for each of our 50 lensing systems. In the middle panel of Fig. 2.6, we plot the value of $\log_{10}\widehat{M}_{\rm hf}$ for each forward-modelled simulation as a black point. The horizontal dashed red line marks the value of $\log_{10}\widehat{M}_{\rm hf}$ given by the mock observation.

We accept the forward-modelled simulations with the 1% of $\log_{10}\widehat{M}_{\rm hf}$ values closest to the observed $\log_{10} M_{\rm hf}$ (Eq. 2.6), which are shown as blue points in the middle panel of Fig. 2.6. The set of $M_{\rm hf}$ values associated with those blue points are then a sample drawn from the posterior distribution of $M_{\rm hf}$ (following the ABC method); their density can be used to estimate the posterior density of $M_{\rm hf}$.

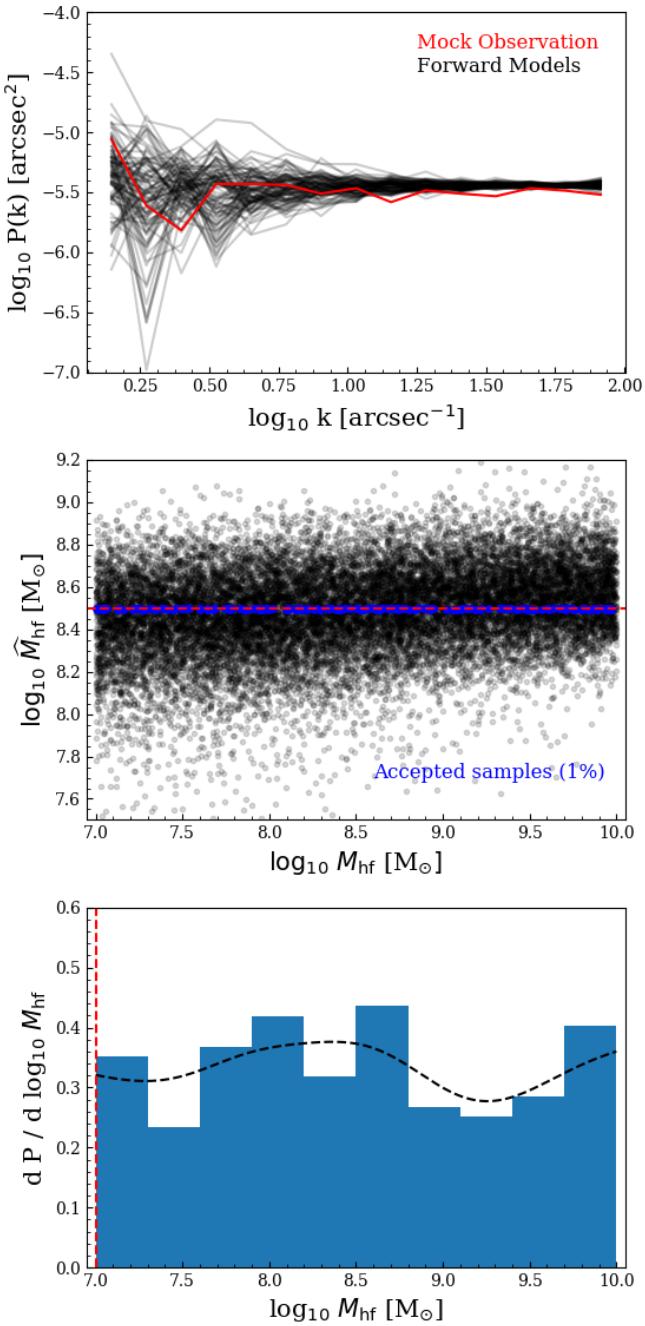


Figure 2.6: **Upper panel**: the power spectrum computed from the best-fit image residuals. The red line is the power spectrum of the mock observation. Black lines are for 100 forward models. **Middle panel**: the summary statistic, $\log_{10}\widehat{M}_{\rm hf}$, computed from the power spectra. The black points are $\log_{10}M_{\rm hf}$ for the forward models. The horizontal dashed red line marks the value for the mock observation and points 1% closest to it are marked in blue. **Lower panel:** The posterior distribution of $M_{\rm hf}$, formed by collecting together the $M_{\rm hf}$ of the blue points is shown in the middle panel. The vertical dashed red line marks the true input of $M_{\rm hf}$. The black dashed curve is a kernel density estimate corresponding to the histogram.

In the lower panel of Fig. 2.6 we plot the posterior density for $\log_{10} M_{\rm hf}$, where the vertical dashed red line shows the true input, $M_{\rm hf} = 10^7$ M$_\odot$. It is clear that with just one system and the data quality of our fiducial setup, we are not able to derive a tight constraint on $M_{\rm hf}$. While improved data quality might improve this somewhat, a single lens system will always be limited by the stochastic nature of the distribution of the low-mass dark matter haloes we are trying to detect. Just because a particular value of $M_{\rm hf}$ allows perturbers of a given mass this does not mean that there will happen to be one in a location where it produces detectable image residuals. As such, tight constraints will rely on combining results from multiple systems.

## 2.3 Results and Discussion

In this Section, we will first show that the forward modelling procedure described above can correctly recover the input value of $M_{\rm hf}$ when combining results from multiple lenses. Then we will explore how the precision of the constraints depends upon the lensing configuration and image quality of the lenses in an observed sample. We will then compare the strength of our method with the method based on quasar flux ratio anomalies.

### 2.3.1 Tests of the accuracy of the method

By repeating the procedure described above for each observed system we can obtain a constraint from our mock observations of 50 lensing systems. Just as for a real set of 50 observed systems, the posterior probability density for $M_{\rm hf}$ will not necessarily peak at the true value. To assess whether our method is biased, we create 500 sets of 50 observed lenses. Running the full procedure described above 500 times, each time for 50 different lenses, would be prohibitively expensive because of the very large number of forward models this would require. We therefore use the same set of 50 macro lens and source model parameters ($\{T\}_{\rm fiducial}$) for each of our 500 sets,

only changing the realisations of low-mass dark matter haloes between the sets of 50 observed images. This allows us to reuse the same forward models for each of our 500 sets.

In principle, we should generate a new set of forward models for each of the 500 sets (together 25000 lenses) because the particular realisation of the dark matter haloes affects the best-fit macro model, which is the model used to generate the forward model images. We will see later that even though there is a slight mismatch in best-fit models for different realisations, we can still correctly recover the true $M_{\rm hf}$. Similarly, to examine how the method behaves with different input (true) values for $M_{\rm hf}$, we further simulate 500 sets of 50 observations with $M_{\rm hf} = 10^8$ and $10^9$ $\mathrm{M}_\odot$ and apply ABC inference to them, all using the same forward models previously simulated.

Note that some care needs to be taken when combining results from multiple ABC calculations. This is because ABC produces an estimate of the posterior distribution, rather than the likelihood. Combining multiple measurements in a traditional Bayesian analysis (with a calculable likelihood function) is a case of multiplying the likelihoods of the different measurements together to get a total likelihood and then multiplying this by the prior in order to find (something proportional to) the posterior distribution. In this chapter we use a flat prior on $\log_{10} M_{\rm hf}$, and thus the posterior density (per unit $\log_{10} M_{\rm hf}$) we obtain is proportional to the likelihood. This means that the posterior densities per unit $\log_{10} M_{\rm hf}$ for individual systems (such as the blue histograms in the lower panel of Fig. 2.6) can be multiplied together to produce something proportional to the joint likelihood, which can then be multiplied by a prior (once) to get the posterior.

Before multiplying individual constraints, to reduce the noise and obtain a smooth likelihood, we apply a kernel density estimation method to the distribution of $\log_{10} M_{\rm hf}$ with a kernel width of 0.3 dex. We have tested smaller kernel sizes, but the constraints quickly become noisy without significant improvement. To correct for boundary effects, we choose the "renormalization" correction for our kernel

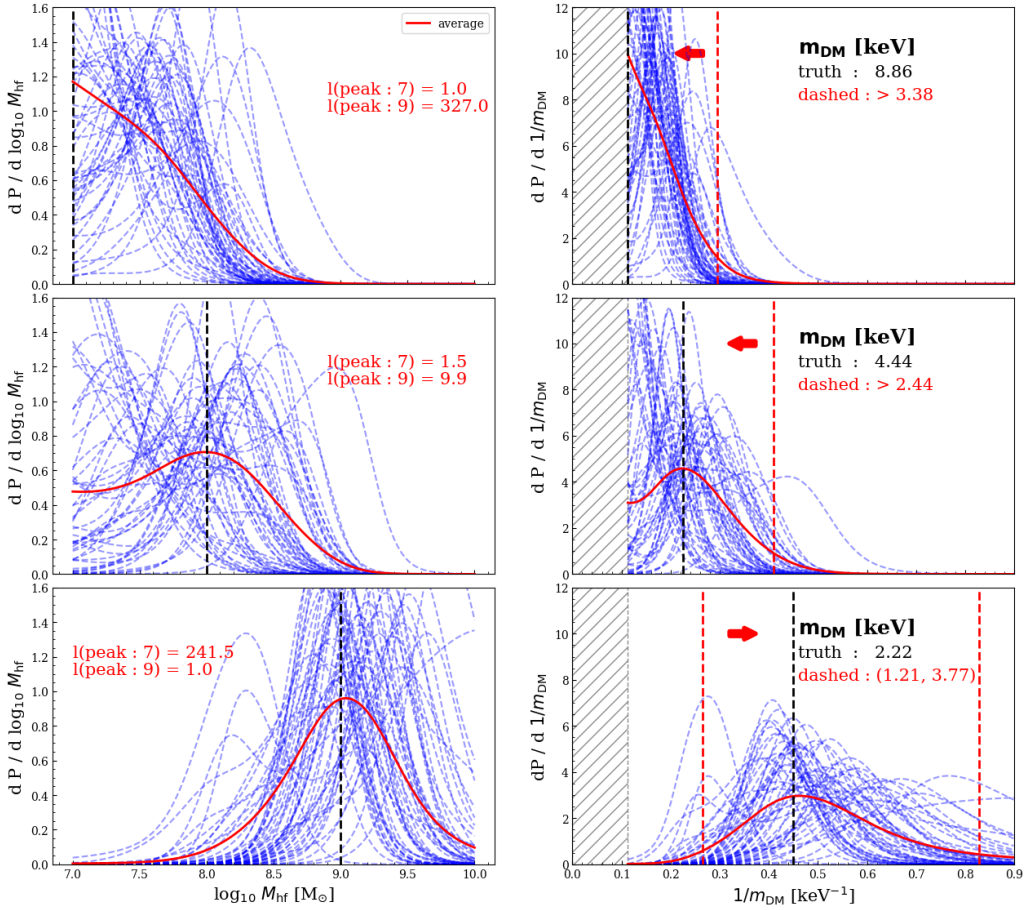


Figure 2.7: Tests on the fiducial setting. The left column shows the constraints on $M_{\rm hf}$ (adopting a flat prior on $\log M_{\rm hf}$) and the right columns the constraints on $1/m_{\rm DM}$ (adopting a flat prior on $1/m_{\rm DM}$). From top to bottom, panels correspond to true $M_{\rm hf}$ values of $10^7$, $10^8$, $10^9$ $\rm M_\odot$, marked by the black vertical dashed lines. Blue dashed curves are individual constraints for each set of 50 lensing systems (for clarity, we only plot 50 out of 500 here). The red curve is the average constraint from the 500 sets. In the right column we use the mean posteriors to place $2\sigma(95\%)$ credible interval limits (upper limits on $1/m_{\rm DM}$ for the top 2 panels and a both upper and lower limit for the bottom one). The hatched regions are where $M_{\rm hf} < 10^7$ $\rm M_\odot$, which is outside the range probed by our forward models.

density estimations.* As an example, the kernel density estimation for the fiducial result is shown as the black dashed curve in the lower panel of Fig. 2.6.

The left column of Fig. 2.7 shows our test results for three different cases with true input $M_{\rm hf}$ of $10^7$ $\rm M_\odot$, $10^8$ $\rm M_\odot$ and $10^9$ $\rm M_\odot$ from top to bottom, respectively. Each

*We use the public package **PyQt-Fit** to implement the kernel density estimation (see "https://pythonhosted.org/PyQt-Fit/").

blue line is a constraint from 50 systems (for clarity, we only show 50 blue lines in the plots). Any one set of 50 observations will not necessarily have a posterior that peaks at the true value, so in order to assess whether our results are systematically biased – as opposed to just subject to random error – we plot a mean posterior distribution from the 500 sets of 50 observations. These are the red lines in Fig. 2.7; they peak close to the input values of $M_{\rm hf}$, suggesting that our method is unbiased. Using these mean posteriors we compute the ratio of the posterior between the peak value and the values at $M_{\rm hf} = 10^7$ M$_\odot$ and $M_{\rm hf} = 10^9$ M$_\odot$. With an input value of $M_{\rm hf} = 10^7$ M$_\odot$, the recovered constraint shows that the model with $M_{\rm hf} = 10^9$ M$_\odot$ is disfavoured with a posterior density $\sim 327$ times smaller than that of the peak. In a WDM universe (e.g. with $M_{\rm hf} = 10^9$ M$_\odot$), $M_{\rm hf} = 10^7$ M$_\odot$ would be ruled out, with a mean posterior density $\sim 242$ times smaller than at the peak.

In the right column of Fig. 2.7, we show our posterior distribution in terms of $1/m_{\rm DM}$, which is the way in which constraints on the DM particle mass from the Lyman-$\alpha$ forest are typically expressed (Iršič et al., 2017). Note that the $1/m_{\rm DM}$ posteriors are not simply the $M_{\rm hf}$ posteriors transformed to a new parameterisation. Instead, we transform the likelihood as a function of $M_{\rm hf}$ to the likelihood as a function of $1/m_{\rm DM}$ following Eq. 1.4, and then adopt a flat prior on $1/m_{\rm DM}$ (as done in Lyman-$\alpha$ studies). This is different from a flat prior on $\log_{10} M_{\rm hf}$ and so the posteriors are not actually the same in the two columns of Fig. 2.7.

Depending on the "behaviour" of the red curves, we place either a $2\sigma$ (95%) upper or lower limit on $1/m_{\rm DM}$. For the cases with true $M_{\rm hf} = 10^7$ and $10^8$ M$_\odot$, we place an upper limit, while for the case with $M_{\rm hf} = 10^9$ M$_\odot$ we place both lower and upper limits. These limits are shown as vertical dashed red lines in the figure. We can see that with 50 fiducial-like lensing systems, at $2\sigma$ level, one can rule out particle candidates with $m_{\rm DM}$ less than 3.38 keV and 2.44 keV in universes with true $m_{\rm DM} = 8.86$ and 4.44 keV respectively, or rule out particles with $m_{\rm DM} > 3.77$ keV and $m_{\rm DM} < 1.21$ keV in a universe with true $m_{\rm DM} = 2.22$ keV. We view the $2\sigma$ limits in the first two panels as conservative because we do not assign any posterior

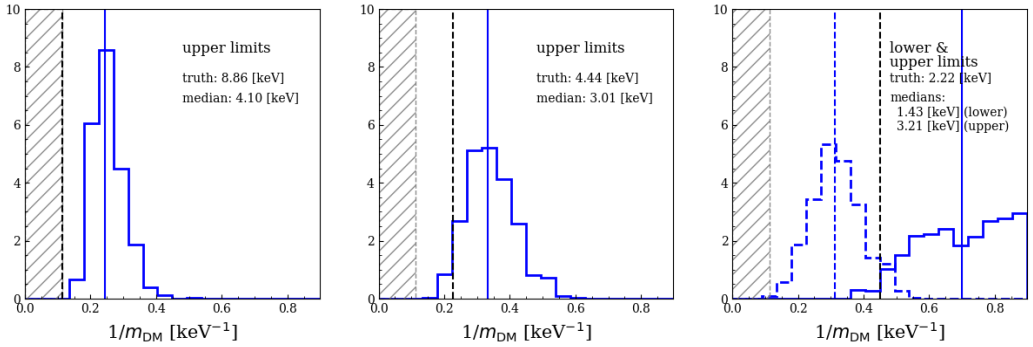


Figure 2.8: Histograms of $2\sigma$ (95%) upper or both upper and lower limits on $1/m_{\rm DM}$. From left to right the input half-mode mass is $M_{\rm hf} = 10^7, 10^8$ and $10^9$ $\rm M_\odot$, with the corresponding DM particle masses written in the relevant panel. The limits are upper limits on $1/m_{\rm DM}$ (i.e. a lower limit on the DM particle mass), except for the case of $M_{\rm hf} = 10^9$ $\rm M_\odot$ where both histograms of upper (solid line) and lower (dashed line) limits on $1/m_{\rm DM}$ are shown. The black dashed lines mark the true inputs. The vertical blue lines mark the medians of the histograms and corresponding median values are also listed.

mass to the shaded regions in our computation. If we had simply assumed that the posterior density in the shaded region was the same as at $\sim 0.12$ keV$^{-1}$, the upper limits would have been tighter.

Note that the constraints discussed above are average results. Observations of any 50 specific lensing systems would yield a constraint like one of the blue dashed lines in the figures, which might be tighter or looser than the average constraint. To demonstrate actual constraint one would expect to get with 50 observations, in Fig. 2.8 we show the histograms of $2\sigma$ limits from the 500 different realisations of a set of lensing observations (for true $m_{\rm DM} = 8.86, 4.44$ keV, we compute lower $2\sigma$ limits, and for true $m_{\rm DM} = 2.22$ keV, we compute lower and upper $2\sigma$ limits). As shown by the histograms, when true $m_{\rm DM} = 8.86$ keV, the median $2\sigma$ constraint we would get is $1/m_{\rm DM} < 0.24$ keV, and thus $m_{\rm DM} > 4.10$ keV. In other words, there is 50% chance to constrain $m_{\rm DM}$ better than 4.10 keV with 50 lenses of similar settings. If true $m_{\rm DM} = 4.44$ keV, the median $2\sigma$ constraint is $\rm m_{DM} > 3.01$ keV. If true $m_{\rm DM}$=2.22 keV, the median constraint obtained is 1.43 keV$< m_{\rm DM} <$ 3.21 keV.

### 2.3.2 Dependency on the lensing configuration

Having shown that with a large number of lensing systems the forward modelling procedure can correctly recover the true $M_{\rm hf}$ (albeit with fairly broad posteriors), we now explore how the constraints change when the properties of the lenses and sources are varied. In particular, we vary the lens and source redshifts, the image S/N ratio, and the image resolution.

To show clearly how the constraints depend upon a specific parameter, we only change one parameter value at a time. For example, to investigate how the result changes for a higher redshift source, we only change the source redshift, and leave the image resolution, Einstein radius, surface brightness, etc., unchanged from the $\{T\}_{\rm fiducial}$ values. Notice that the parameters listed in Table 2.1 are observational rather than intrinsic physical quantities, so by fixing a parameter, we refer to fixing a particular observational quantity. For example, keeping the source surface brightness unchanged from a redshift of 1 to 2.5 means that the source galaxy at $z = 2.5$ is actually intrinsically brighter because of cosmological dimming. The reason for changing quantities in this way is that we want to focus on how the results change from an observational perspective and thus provide a basic idea of what type of lensing configuration has most constraining power, which may help inform future observational designs.

In total, we have carried out five additional tests: placing the lens at a lower redshift of 0.2, denoted as $\{T\}_{\rm lz=0.2}$; placing the source at a higher redshift of 2.5, denoted as $\{T\}_{\rm sz=2.5}$; doubling the exposure time, denoted as $\{T\}_{\rm exp=1200}$; lowering the resolution, with pixel size of $0.1''$ and PSF $\sigma$ of $0.08''$, similar to the expected resolution of images from the Euclid Space Telescope (Collett, 2015), denoted as $\{T\}_{\rm Euclid}$; assuming a similar resolution to that of the China Space Station Telescope (CSST), with pixel size of $0.075''$ and PSF $\sigma$ of $0.08''$, denoted $\{T\}_{\rm CSST}$. To first focus on the changes caused by different settings, without being affected by set-of-observations to set-of-observations noise, we compare the mean

posteriors from 500 sets of 50 observed systems (i.e. the equivalents of the red lines in Fig. 2.7).

In the left column of Fig. 2.9 we plot the expected $M_{\rm hf}$ posteriors for different lensing configuration using different colours. Blue, green, red, cyan, orange and purple correspond to the settings, $\{T\}_{\rm fiducial}$, $\{T\}_{\rm lz=0.2}$, $\{T\}_{\rm sz=2.5}$, $\{T\}_{\rm exp=1200}$, $\{T\}_{\rm Euclid}$ and $\{T\}_{\rm CSST}$, respectively. Different rows show results assuming different true inputs of $M_{\rm hf}$, which are marked as vertical dashed black lines. As in Fig. 2.7, we plot $1/m_{\rm DM}$ posteriors in the right column and place upper (in the top two panels) or both lower and upper (in the bottom panel) $2\sigma$ limits on $1/m_{\rm DM}$, which are marked as vertical dashed lines. The red, green and blue curves show how the results vary with the lens and source redshifts.

Increasing either the source or lens redshift improves the constraints because (at fixed Einstein radius) the volume in which low-mass dark matter haloes are projected close to the observed Einstein ring increases as either redshift is increased. The comparison between the cyan and blue curves shows that increasing the S/N ratio (exposure time) results in a better constraint. Also, better angular resolution gives better constraints when comparing the fiducial setting (blue curve) and the Euclid / CSST resolution setting (orange / purple curves), but the improvement is not significant. Although a worse constraint is obtained with lower image resolution, we see that even with lower angular resolution we can distinguish between models with $M_{\rm hf}$ of $10^7$ $\rm M_\odot$ and $10^8$ $\rm M_\odot$. The advantage of Euclid and CSST will be sample sizes that are vastly larger than 50. Note that future Euclid/CSST observations will likely be different from the sample we simulate here: they will have, for example, different lens/source redshift distributions, data quality and Einstein radii. Those differences can potentially make our predictions here different from future real observations.

Similarly, we use average constraints above to demonstrate the result dependency on lensing configurations, while for the constraints from individual sets of 50 strong lensing systems with different lensing configurations, we refer the $2\sigma$ limit histo-

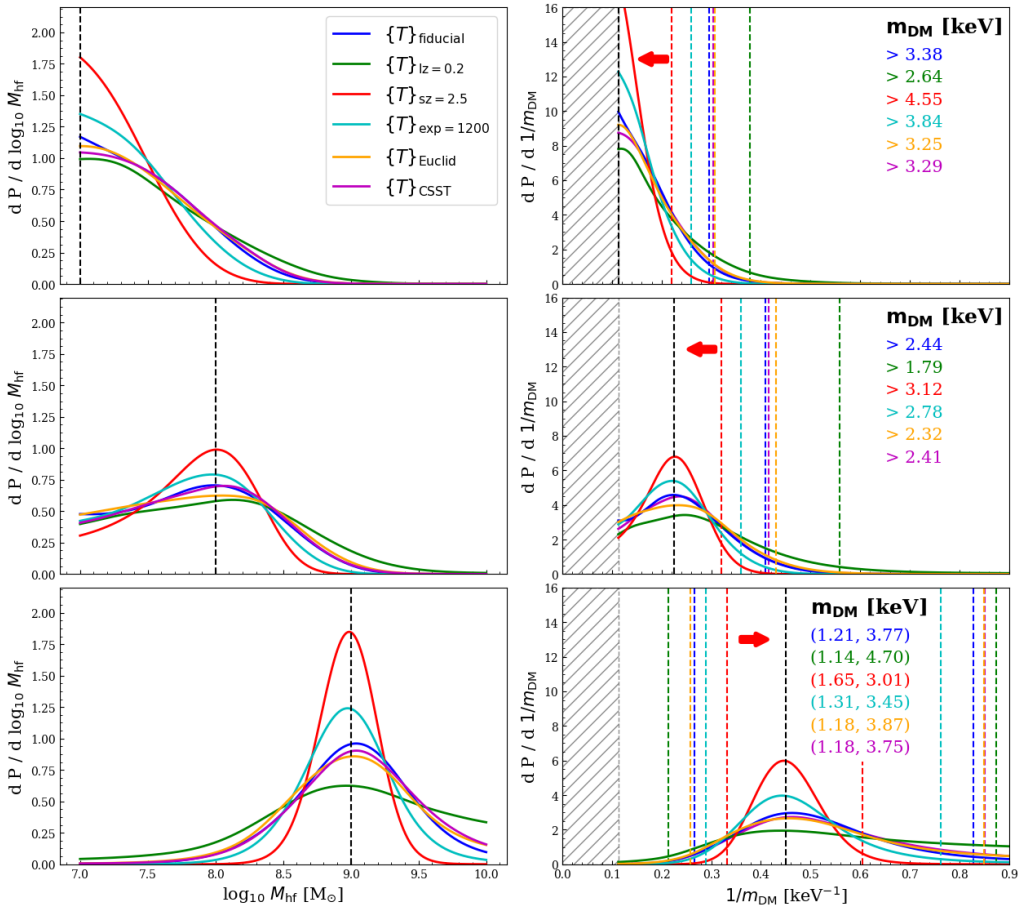


Figure 2.9: Average constraints from 50 lensing systems with different settings. As in Fig. 2.7, the left panels show the constraints on $M_{\rm hf}$ and the right panels the constraints on $1/m_{\rm DM}$. Blue, green, red, cyan, orange and purple lines correspond to the results of settings, $\{T\}_{\rm fiducial}$, $\{T\}_{\rm lz=0.2}$, $\{T\}_{\rm sz=2.5}$, $\{T\}_{\rm exp=1200}$, $\{T\}_{\rm Euclid}$ and $\{T\}_{\rm CSST}$ respectively. The vertical dashed black lines mark the true input values and the color lines the corresponding $2\sigma$ upper limits (top 2 panels) or both upper and lower limit (bottom panel) on $1/m_{\rm DM}$.

grams in Fig. 2.10. Colors of the histograms follow the meaning of Fig. 2.9. The vertical dashed line mark the true input and the left regions below our test range are plotted in shadow. For each setting, we list the medians of $2\sigma$ constraints in corresponding colors. As shown, the dependency reflected from the histograms is the same as that from the average constraints in Fig. 2.9. Among all the settings, the setting with a higher redshift source gives the best constraint, where when true $m_{\rm DM} = 8.86$ keV, the median $2\sigma$ constraint one could get is $m_{\rm DM} > 5.20$ keV.

To summarize, the tests shown here agree with the expectation that lensing systems

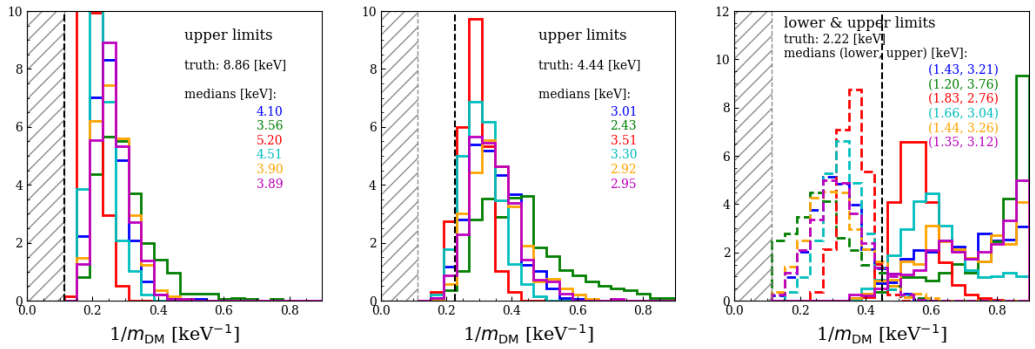


Figure 2.10: Histograms of $2\sigma$ (95% upper) limits (solid lines) and lower limits (dahsed lines, only in the rightmost panel) on $1/m_{\rm DM}$. The vertical black dashed lines mark the true input $m_{\rm DM}$ in each panel. The colours of the histograms follow the meaning of in Fig. 2.9. The medians of the histograms are also listed in corresponding colors in the panels.

with longer exposure times, higher resolution, and more low-mass dark matter haloes (higher source redshifts and a larger area around the Einstein arcs) give tighter constraints.

### 2.3.3 Model assumptions and limitations

Our method makes a number of simplifying assumptions which we now summarize and describe in more detail.

By simulating low-mass dark matter haloes with the mass function of Eq. 1.3 we neglect lensing perturbations from subhaloes within the lens galaxy. This is a good approximation since, as Li et al. (2017) have shown, for realistic lensing configurations the signal is dominated by line-of-sight haloes, rather than by subhaloes in the lens. In any case, this assumption makes our results conservative, as including subhaloes would boost the lensing perturbations, increasing the signal we can extract from the lens model residuals. On the other hand, there are uncertainties regarding subhaloes that do not affect line-of-sight haloes, for example, the extent of tidal disruption (Despali et al., 2018, Richings et al., 2020); marginalising over these uncertainties would weaken the constraint on $M_{\rm hf}$.

We neglect any uncertainties on the amplitude and shape of the (CDM) halo mass

function. The amplitude is fixed by the value of the cosmological parameter, $\sigma_8$, which is known to better than 1% from cosmic microwave background data (Planck Collaboration et al., 2020). The shape is known very precisely from cosmological simulations (Wang et al., 2020). There is, however, some degeneracy between the amplitude of the halo mass function and the half-mode mass. Some lensing studies, such as that of Gilman et al. (2019) based on flux ratio anomalies, have included the amplitude of the mass function as a free parameter to be fit at the same time as the subhalo mass function.

In this chapter we have assumed an SIE lens mass model, whereas in studies of real lenses a power-law mass model with external shear is widely used (e.g. Vegetti et al., 2014, Dye et al., 2014). This gives the mass model more freedom to fit the residuals, reducing the signal left over from substructures. Even then, the mass model may only provide an approximate fit to the lens and result in residuals not associated with subhaloes, at which point even more complex mass profiles (Nightingale et al., 2019), or a potential corrections-based approach may be required (Vegetti and Koopmans, 2009a). We assume a core-Sérsic model for the source light, whereas studies using real data often use a non-parametric approach that reconstructs a source's irregular morphology (see Warren and Dye, 2003, Suyu et al., 2006). Gilman et al. (2020b) show how such an approach may absorb part of the residual signal of the low-mass perturbers, reducing the available information on the halo mass function. PyAutoLens has all the necessary functionality to test these assumptions and this will be the topic of future work.

Our method implicitly attributes all image residuals to the presence of perturbing dark matter haloes when, in reality, there could be other sources of mismatch between a true lens and source model and the best-fit macro model. In the idealized setup used here we have shown that this allows us to obtain a correct measurement of the input half-mode mass. In reality, other sources of perturbations will contribute to the power spectrum of the image residuals, including a deficient model for the smooth component of the lens, an inaccurate description of the telescope PSF and

artefacts or correlated noises introduced by the data reduction process. Not taking these effects into account may bias our inference of the subhalo mass function. Currently, the impact of any individual effect is unclear and further investigation is required, noting that all effects that impact the signal can, in principle, be included in our forward modeling procedure and marginalized over.

On a positive note, our use of the power spectrum to define a summary statistic to extract the signal from the residuals is likely to be suboptimal. A more carefully crafted summary statistic or a machine learning-based approach (see Brehmer et al., 2019, Diaz Rivero and Dvorkin, 2020) can potentially improve the signal that can be extracted from a lens system and thus provide better constraints on $M_{\rm hf}$ than shown here. It could also make the estimation less sensitive to systematic sources of residuals as shown by Birrer et al. (2017a), and so increase the constraining power of the forward modelling method.

### 2.3.4 Comparison with flux ratio anomalies

A theoretical investigation of the constraining power of flux ratio anomalies was performed by Gilman et al. (2019), who subsequently applied their method to real observations, placing constraints on both the dark matter mass function and the mass-concentration relation (Gilman et al., 2020a,c). It is interesting to compare our approach with that of Gilman et al. (2019). Note, however, that, as we just discussed, these authors treat the amplitude and slope of the halo mass function as free parameters, whereas our tests assume a halo mass function with only one free parameter, $M_{\rm hf}$. In our tests, for a universe with true $M_{\rm hf} = 10^7$ M$_\odot$, our fiducial calculation gives an upper $2\sigma$ constraint (average constraint shown in Fig. 2.7), $M_{\rm hf} = 10^{8.25}$ M$_\odot$, which is slightly smaller than the upper constraints quoted by Gilman et al., $M_{\rm hf} = 10^{8.34}$ M$_\odot$, for a 2% uncertainty on flux measurements (see Figure 8 of Gilman et al., 2019). Given the different assumptions in the two studies this comparison serves to show that the constraints that they provide are roughly comparable.

When considering the relative performance of our method and those based on flux ratio anomalies it is pertinent to consider the mass scales to which each method is sensitive. The "coldest" case in our tests assumes $M_{\rm hf} = 10^7$ $M_\odot$ and our signal is heavily influenced by the lensing effects of larger perturbers with $M_{200} \sim 10^{7-8}$ $M_\odot$. The small detection area of flux ratio anomalies results in a lack of sensitivity to subhaloes with these relatively high masses (as these subhaloes are rare), but the "point-like" sources (with highly variable surface brightnesses over a small region) provide sensitivity down to dark matter haloes with $M_{200} \sim 10^6$ $M_\odot$, a scale that is not accessible with our approach. However, another problem faced by flux ratio anomalies is that the sparsity of information means that the degeneracy between anomalies caused by substructure and by a complex smooth halo is not easily broken, which can bias the inference on the abundance of substructures (Xu et al., 2015, Hsueh et al., 2018). The two approaches are therefore complementary and, together, can provide constraints on the halo mass function over a broad range of masses.

## 2.4 Conclusions

In this chapter we have presented a method based on forward modelling applied to the analysis of resolved strong lensing arc data that can constrain a cutoff in the dark matter halo mass function. The key idea is to simulate a large number of strong lensing images (forward models) based on the best-fit macro model, with the addition of perturbations to the lens model from low-mass dark matter haloes (whose number depends on the assumed nature of the dark matter). These images can then be fit in the same manner as the original observed image, and the best-fit image residuals for the observed system can be compared with the best-fit image residuals for the forward models. This comparison is made by means of the power spectrum of the image residuals within the Approximate Bayesian Computation framework and leads to a posterior distribution for the half-mode mass ($M_{\rm hf}$) which

describes the cutoff in the halo mass function. Our main results may be summarized as follows:

- For mock observed lenses constructed from parametric source light profiles and lens mass models, we confirm that information on low-mass dark matter haloes can be extracted from the power spectrum of the best-fit image residuals. As demonstrated in Fig. 2.7, with a large number of observed lenses, a forward modelling procedure can correctly recover the true input half-mode mass, $M_{\rm hf}$ in average (the red curves). However, the scatter in the constraint is significant even though results for 50 systems have been combined together (blue curves), which may be attributed to the large intrinsic scatter in realisations of low-mass dark matter haloes. Taking the scatter into accounts, we compute the histograms of $2\sigma$ limits (see Fig. 2.8) and find that, with 50 lensing systems, for our fiducial settings (see Table 2.1), if the true (thermal) $m_{\rm DM}$ is 8.86 keV ($M_{\rm hf} = 10^7$ M$_\odot$), the median $2\sigma$ constraint on $m_{\rm DM}$ is that $m_{\rm DM} > 4.10$ keV (or there is 50% chance that the $m_{\rm DM}$ can be constrained better than 4.10 keV at $2\sigma$ level). Conversely, in a WDM universe where the true (thermal) $m_{\rm DM}$ is 2.22 keV ($M_{\rm hf} = 10^9$ M$_\odot$), one could get a median measure of $m_{\rm DM}$ to be between 1.43 keV and 3.21 keV at $2\sigma$ level.

- We have tested the dependency of the method on different lensing configurations and image quality settings. As shown in Fig. 2.9 & 2.10, the dependency agrees with expectations: higher redshift sources and/or larger areas around the Einstein arcs, and better data quality (longer exposure time and/or higher resolution) all result in a tighter constraint. Among our tests, the one with sources placed at $z = 2.5$ produced the strongest constraint: in a universe with true $m_{\rm DM} = 8.86$ keV ($M_{\rm hf} = 10^7$ M$_\odot$), particles with mass less than 5.20 keV can be ruled out at the $2\sigma$ level (see medians of the histograms in Fig. 2.10). Although a slightly worse constraint is obtained from images with the resolution of Euclid/CSST, 50 systems can still provide a constraint on

$M_{\rm hf}$, and with Euclid/CSST data we will have many more than 50 strong lenses. We defer a thorough test using mock strong lensing samples similar to those expected from Euclid/CSST to future work.

Throughout this study we have made several simplifying assumptions, particularly in using parametric models for the lens mass distributions and the source light profiles. The effects of removing these assumptions will need to be investigated before we can safely apply our technique to real observations. We have shown that, in principle, information on low-mass dark matter haloes can be statistically extracted from the power spectrum of the image residuals. In the near future, we hope that using a more powerful summary statistic together with more advanced lens modelling techniques (such as pixelized sources) can improve the power of this technique. With thousands of new strong lensing observations expected from future space telescopes, there is every prospect of pinning down the mass of the dark matter particles using this forward modelling technique.

Chapter 3

# Re-investigating sensitivity mappings of line-of-sight and on-lens low-mass haloes

**Abstract**

We rederive the number density of intervening line-of-sight haloes relative to lens subhaloes in galaxy-galaxy strong lensing observations, where these perturbers can generate detectable image fluctuations. Previous studies have calculated the detection limit of a line-of-sight small-mass dark halo by comparing the lensing deflection angles it would cause, to those caused by a subhalo within the lens. However, this overly simplifies the difference in observational consequences between a subhalo and a line-of-sight halo. Furthermore, it does not take into account degeneracies between an extra subhalo and the uncertain properties of the main lens. More in keeping with analyses of real-world observations, we regard a line-of-sight halo as detectable only if adding it to a smooth model generates a statistically significant improvement in the reconstructed image. We find that the number density of detectable line-of-sight perturbers has been overestimated by as much as a factor of two in the previous literature. For typical lensing geometries and configurations, very deep imaging is sensitive to twice as many line-of-sight perturbers as subhaloes,

but moderate depth imaging is sensitive to only slightly more line-of-sight perturbers than subhaloes.

## 3.1 Introduction

Strong lensing systems that exhibit giant arcs or Einstein rings can appear measurably perturbed if any of the light from the source passes sufficiently close to a small dark halo (Koopmans, 2005, Vegetti and Koopmans, 2009a,b, Vegetti et al., 2012, Hezaveh et al., 2016, Li et al., 2016b). In order to detect a small dark halo explicitly, one needs to model the tiny perturbations to the image that are caused by a small halo. The measurement is difficult but applying sophisticated data analysis and modelling tools to high resolution imagery, it is possible to detect small haloes projected near the Einstein radius of the lens and infer their mass (e.g. Koopmans, 2005, Vegetti and Koopmans, 2009a). So far three haloes with pseudo-Jaffe mass smaller than $10^{10}$ $M_{\odot}$ have been detected.

To constrain the nature of the dark matter with this technique it is, of course, necessary to know the expected number of lensing perturbers in CDM and other models of interest. The perturbers can be either subhaloes of the main lens or "field" line-of-sight haloes that are not part of the main lens but appear projected near its Einstein radius. To reduce the complexity, an "effective" mass concept was proposed to approximate the lensing perturbation of a line-of-sight halo as a subhalo. By doing so, people have computed that the expected number detectable line-of-sight low-mass perturbers is several times of that of the subhaloes (Li et al., 2017, Despali et al., 2018, hereafter, L17 and D18 respectively), which is an encouraging result because it greatly simplifies the theoretical analysis. Unlike for subhaloes, whose mass function is affected by environmental effects, calculating the mass function of dark central haloes in the mass range of interest - below the threshold for star formation - is straightforward since these haloes have never been affected by baryons. Thus, a standard calculation of the mass function based

on dark-matter-only simulations (Frenk et al., 1988) gives very precise results (see Zavala and Frenk, 2019, for a recent review).

By contrast, the mass function of subhaloes is determined by a number of processes, such as tidal stripping or tidal shocking, that alter the mass distribution and can destroy the subhalo. To calculate these processes requires modelling the host galaxy in detail, including its baryonic components. This is, of course, a much more complicated problem than simply following the evolution of dark matter haloes. Significant advances, however, have been achieved in recent years with a new generation of cosmological hydrodynamics simulations that can produce realistic galaxy populations (e.g. Vogelsberger et al., 2014, Schaye et al., 2015). Here, we will make extensive use of the high-resolution hydrodynamics simulation of Richings et al. (2021) of a galaxy and its environment which includes the relevant baryon physics processes.

L17 and D18 both made an important assumption: that the perturbation induced by a subhalo can always be well fitted by the perturbation induced by a line-of-sight halo with an NFW profile. This assumption, however, may not be exactly true because the deflection angles produced by a line-of-sight halo can be very different from that of a subhalo in certain redshift ranges. Furthermore, these earlier studies did not carry out complete modelling of the lensing process, for example, assuming realistic noise levels, and this may further bias the results.

In this chapter, we revisit the importance of the contribution of line-of-sight perturbers by modelling a set of realistic strong lensing mock images. In earlier studies, the comparison of deflection angles was used to decide whether a perturber is detectable or not, through the concept of an "effective mass". Here we derive the detectable mass threshold for line-of-sight perturbers by directly evaluating the difference in log-likelihood between a model with a perturber and a model without a perturber. The new threshold is now directly obtained from modelling image fluxes and thus it is more straightforward and robust, where it takes into account factors from flux modelling processes previously not considered, like the degeneracy

between the perturber and the macro model. We also investigate the dependence of the relative contribution of the two types of object on the redshift and the signal-to-noise (S/N) ratio of the observations.

An independent study of the sensitivity function using PyAutoLens is provided by Amorisco et al. (2022). This work reassuringly reaches the same conclusion as us on the dependence of the sensitivity function on the redshift of the perturbing halo, despite using a different approach to calculate the sensitivity function and mock strong lens datasets with different properties. Looking at only line-of-sight haloes, this study highlights the impact that the intrinsic scatter in halo concentrations has on the sensitivity function, and shows that the dependency of the concentration–mass relation on the dark matter model improves strong lensing as a probe of dark matter. In this chapter, we explicitly include subhaloes within the lens galaxy (in addition to line-of-sight haloes), accounting for their different mass function and density profiles due to baryonic physics. Thus, we set out to answer whether the line-of-sight or lens galaxy subhalos dominate the constraints on dark matter.

The structure of the chapter is as follows. In Section 3.2, we describe how we construct mock lenses, how we compute the sensitivity map and the method we use to translate sensitivity maps into constraints on the halo mass function. In Section 3.3, we present our results and in Section 3.4, we summarize our conclusions. Throughout the chapter we adopt the Planck cosmological parameters (Planck Collaboration et al., 2016): $H_0 = 67.7\,\mathrm{km\,s^{-1}\,Mpc^{-1}}$, $\Omega_\mathrm{m} = 0.307$ and $\Omega_\Lambda = 0.693$.

## 3.2 Method

### 3.2.1 Mock Lenses

We construct five sets of mock lenses, including examples with different image configurations, redshifts, noise levels and angular resolution. For simplicity we set the density distribution of all primary lenses to be SIEs (Eq. 2.1). We do not add

external shear in the mock lenses. However, when modelling the lens we do include the external shear as part of our mass model (Witt and Mao, 1997).

To simulate the source galaxies, similar to last chapter, we assume a core-Sérsic as Eq. 2.3, of which the small core in our model helps to remove potential numerical inaccuracies induced by the cuspy nature of the regular Sérsic profile. Throughout our tests in this chapter we also fix $\alpha = 2.0$ and $r_c = 0.01''$.

The fiducial mock image setup has a nearly complete Einstein ring with the lens galaxy at redshift, $z = 0.5$, and the source galaxy at $z = 1$. The emission of the lens galaxy is omitted here. The mock image has similar angular resolution to HST imaging, where the pixel size is $0.05''$ and a Gaussian PSF is assumed where $\sigma = 0.05''$ (FWHM of $\sim 0.118''$). For the noise level, we try to set it to be similar to the best cases in the SLACS sample (Bolton et al., 2006), where the maximum S/N in the image pixels is around 40 for a 2000s exposure. We adopt a background sky noise level of 0.1 $e^-\,pix^{-1}\,s^{-1}$, which is estimated from HST images of SLACS lenses. To add noise to each mock image, the background sky is added to the lensed source image, the data is converted to units of counts and Poisson noise values are drawn and added to every pixel. The source intensity is adjusted to make the maximum pixel S/N be $\sim 40$ and the data is then converted back to $e^-s^{-1}$. The lens and source parameters of the fiducial setting is shown in the third column of Table 3.1.

Based on this fiducial setup, we also change the appropriate parameters to explore the effects of different image configurations, lens galaxy redshifts, noise levels and angular resolution. We summarize our mock images (without adding any low mass haloes) in Fig. 3.1, where each setting's name is labelled in the upper left of each panel. The details of each setting are as follows:

- ER-EXP2000 — This is our fiducial setting, a nearly complete Einstein ring with a radius of $1.5''$, corresponding to an Einstein mass of $6.4 \times 10^{11}$ $M_\odot$ within 9.4 kpc.

| | | Einstein Ring | Quad |
|---|---|---|---|
| Lens | (x, y) [($''$, $''$)] | (0.0, 0.0) | (0.0, 0.0) |
| | $R_{\rm E}$ [$''$] | 1.5 | 1.5 |
| | q | 0.95 | 0.65 |
| | $\theta$ [°] | 30 | 30 |
| External Shear | magnitude | 0.0 | 0.0 |
| | $\theta$ [°] | 0.0 | 0.0 |
| Source | (x, y) [($''$, $''$)] | (0.1, 0.1) | (-0.05, 0.1) |
| | $r_{\rm e}$ [$''$] | 0.2 | 0.2 |
| | q | 0.52 | 0.7 |
| | $\theta$ [°] | 30 | 30 |
| | $I^{'}$ [$e^{-}$ $pix^{-1}$ $s^{-1}$] | 2.2 | 2.3 |
| | $n$ | 2.5 | 2.0 |
| | $r_{\rm c}$ [$''$] | 0.01 | 0.01 |
| | $\alpha$ | 2.0 | 2.0 |

Table 3.1: Parameters of the lens and source galaxies for the Einstein Ring and Quad images in our mock simulations.

- ER-EXP8000 — It has the same setting as our fiducial mock except the exposure time increases to 8000s, of which the maximum pixel S/N is $\sim 80$.

- ER-EXP2000-LOWZ — The main lens in this case is located at redshift, $z = 0.22$, while the source is still at $z = 1$. When changing the lens redshift, we keep its Einstein radius (in arcsec) and noise level unchanged. At this redshift, a $1.5''$ Einstein radius corresponds to an Einstein mass of $1.3\times10^{11}$ $M_{\odot}$ within 5.5 kpc.

- QUAD-EXP2000 — In this setting, we simulate an image with quadruple arcs with the same noise level and angular resolution as the fiducial case. The lens and source parameters of this configuration are listed in the fourth column of Table 3.1.

- ER-CSST — We also simulate a configuration with lens and source properties as in the fiducial case but with the same image resolution as the China Space Station Telescope (CSST). The CSST resolution is slightly worse than for the HST, with a pixel size of $0.075''$ and a PSF $\sigma$ of $0.08''$ (FWHM of $\sim 0.188''$). We note that the hardware design of the CSST is not fully determined yet, so

for our purpose here, which is to study purely resolution effects, we assume it has similar noise conditions as the HST except for the resolution. Since the pixel area is 2.25 times larger, the background sky noise is also increased to 0.225 $e^- \, pix^{-1} \, s^{-1}$. The image simulated here may therefore be treated as a pixel binned version of the fiducial mock image using a larger pixel and PSF size of the CSST.

- ER-JWST — The image resolution of this case is close to that of James Webb Space Telescope (JWST) images, which have a pixel size of $0.03''$ and a PSF $\sigma$ of $0.013''$ (FWHM of $\sim 0.03''$). Note that now the pixel areas are 0.36 times those of the previous case; the noise is also changed consistently to be 0.036 $e^- \, pix^{-1} \, s^{-1}$.

In Table 3.2 we summarize the key features of the five mock settings (the quantities of the last three columns are defined in our results part, Section 3.3).

We perturb the images of the mock lenses with two types of objects. One are small-mass dark matter haloes along the line-of-sight and the other are subhaloes within the host halo of the lens galaxy. We model the line-of-sight haloes with spherical NFW profiles (Eq. 1.5) following the mass-concentration relation given by Ludlow et al. (2016).

For subhaloes associated with the lens, we simulate them as a tNFW profile with $n = 2$ in Eq. 1.8 (see Eq. A.26∼A.33 of Baltz et al., 2009, for relevant equations). Particularly, the total mass of the subhalo can be written as (Eq. A.29 of Baltz et al., 2009)

$$M_{\rm tot} = 4\pi\rho_{\rm s} r_{\rm s}^3 \frac{\tau^2}{2\left(\tau^2+1\right)^3}\left[2\tau^2\left(\tau^2-3\right)\ln\tau - \left(3\tau^2-1\right)\left(\tau^2+1-\tau\pi\right)\right], \quad (3.1)$$

where $\tau \equiv r_{\rm t}/r_{\rm s}$. $r_{\rm t}$ and $r_{\rm s}$ are the truncated radius and scale radius, respectively.

We derive the mean relation between $r_s$, $r_t$ and $M_{\rm tot}$ using the high-resolution hydrodynamical simulation by Richings et al. (2021). This is a zoom, high resolution resimulation of a halo with $M_{200}$ (the mass within $r_{200}$, the radius where the

| Label | Configuration | $z_l$ | $z_s$ | Exposure time (s) | $\sigma_{PSF}$ | Pixel size | $N_{los}$ | $N_{sub}$ | $N_{los}/N_{sub}$ |
|---|---|---|---|---|---|---|---|---|---|
| ER-EXP2000 | Einstein Ring | 0.5 | 1.0 | 2000 | 0.05 | 0.05 | 0.85 | 0.66 | 1.29 |
| ER-EXP8000 | Einstein Ring | 0.5 | 1.0 | 8000 | 0.05 | 0.05 | 2.50 | 1.24 | 2.02 |
| ER-EXP2000-LOWZ | Einstein Ring | 0.22 | 1.0 | 2000 | 0.05 | 0.05 | 0.39 | 0.38 | 1.03 |
| QUAD-EXP2000 | Quad | 0.5 | 1.0 | 2000 | 0.05 | 0.05 | 0.64 | 0.51 | 1.25 |
| ER-CSST | Einstein Ring | 0.5 | 1.0 | N.A.[1] | 0.08 | 0.075 | 0.72 | 0.60 | 1.20 |
| ER-JWST | Einstein Ring | 0.5 | 1.0 | N.A.[1] | 0.03 | 0.03 | 1.06 | 0.75 | 1.41 |

[1] For our purpose to investigate how image resolution affect our results, we set them to have equivalent depth of observation as our fiducial setting.

Table 3.2: Column 1 shows the label of six mocks. Column 2-6 show the settings of lens configuration, including lens redshift, source redshift, exposure time, PSF size and pixel size. Column 7-8 show the expected detection of line-of-sight haloes, the subhaloes per system, and Column 9 shows their ratio. Parameters of the Einstein Ring and Quad lens configurations are listed in Table 3.1.

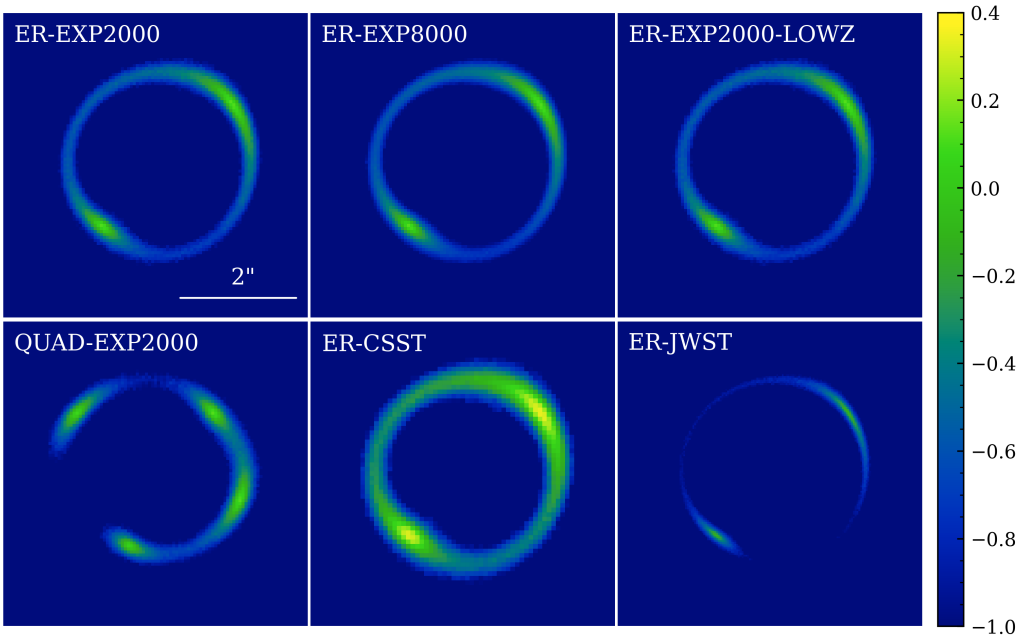


Figure 3.1: Mock observations of the galaxy-galaxy strong lens systems that we investigate. The name of each setting is shown on the top left of each panel. "ER-EXP2000" is our fiducial mock image. "ER-EXP8000" has a 8000s exposure. "ER-EXP2000-LOWZ" has a main lens located at z = 0.22. "QUAD-EXP2000" is an image with quadruple arcs. "ER-CSST" uses the resolution of CSST, which has a pixel size of 0.075″ and a PSF sigma of 0.08″ (FWHM of 0.188″). "ER-JWST" uses the resolution of JWST, which has a pixel size of 0.03″ and a PSF sigma of 0.013″ (FWHM of 0.03″). Parameters of the lens and source parameters for the Einstein Ring and Quad images are listed in Table 3.1. The key features of the systems are listed in Table 3.2. The images are shown in $\log_{10}$ scale, and the unit of the color bar is $e^-$ $pix^{-1}$ $s^{-1}$.

enclosed density is 200 times the critical density of the Universe) of $10^{13.1}$ $M_\odot$ at $z = 0.18$ selected from the EAGLE simulation volume (Schaye et al., 2015) and resimulated with 17 times better gas mass resolution than EAGLE, $m_g = 1.8 \times 10^5$ $M_\odot$, and about 100 times better dark matter mass resolution than EAGLE, $m_{\rm DM} = 8.3 \times 10^4$ $M_\odot$. Such high resolution allows us to resolve the internal structure of subhaloes more massive than $10^8$ $M_\odot$. Haloes were identified using the friends-of-friends algorithm (Davis et al., 1985) and subhaloes using the **SUBFIND** algorithm (Springel et al., 2001); the density profiles of subhaloes in the mass range $10^8 \sim 10^{11}$ $M_\odot$ were fit with the tNFW formula to derive the values of $r_{\rm s}$, $r_{\rm t}$ and $M_{\rm tot}$.

Since in actual observations, only subhaloes around the Einstein radius matter, we only select subhaloes whose projected positions fall in an annular region between $0.5''$ and $3.0''$ from the lens centre to derive the relations between $r_s$, $r_t$ and $M_{\rm tot}$. To improve the statistics, we rotated the simulated halo 10000 times at random. For the mock lenses at $z = 0.22$ and $z = 0.5$ we make use of the snapshots at $z = 0.183$ and $z = 0.503$ respectively. To make sure the derived relations are not dominated by any particular subhalo, e.g. by one very close to the Einstein radius in 3D, we carry out bootstrap tests whereby we repeat the same procedure 200 times and each time we derive the linear relations from a random re-sample of all subhaloes. The linear relation is computed by minimizing a $\chi^2$ defined as:

$$\chi^2 = \sum_{\rm i=1}^{\rm N} W_{\rm i} \left(y_{\rm i} - (m \times x_{\rm i} + c)\right)^2 , \tag{3.2}$$

where $m$, $c$ are the linear relation slope and intercept, $(x_{\rm i}, y_{\rm i})$ is the coordinate of the $i$-th data point and $W_i$ is the number of times the $i$-th data point is repeated in the sample. We then take the median linear relations from the 200 tests to model the subhaloes.

Taking the snapshot at $z = 0.183$ as an example, in Fig. 3.2, we plot the values of $M_{\rm tot}$, $r_{\rm s}$ and $\tau\,(r_{\rm t}/r_{\rm s})$ for subhaloes as blue circles. The area of each circle reflects how many times each subhalo fell on the annular region around the Einstein radius, which is taken as a weight for the point when deriving the linear relation. For this lens system we find,

$$\begin{aligned} \log_{10}\left(\frac{r_{\rm s}}{\rm kpc}\right) &= (0.60 \pm 0.09)\log_{10}\left(\frac{M_{\rm tot}}{\rm M_\odot}\right) - (4.85 \pm 0.77) \\ \log_{10}(\tau) &= (-1.21 \pm 0.10)\log_{10}\left(\frac{r_{\rm s}}{\rm kpc}\right) + (0.59 \pm 0.04)\,. \end{aligned} \tag{3.3}$$

For the lens at $z = 0.5$ we find,

$$\begin{aligned} \log_{10}\left(\frac{r_{\rm s}}{\rm kpc}\right) &= (0.49 \pm 0.06)\log_{10}\left(\frac{M_{\rm tot}}{\rm M_\odot}\right) - (3.90 \pm 0.54) \\ \log_{10}(\tau) &= (-1.21 \pm 0.09)\log_{10}\left(\frac{r_{\rm s}}{\rm kpc}\right) + (0.55 \pm 0.03)\,, \end{aligned} \tag{3.4}$$

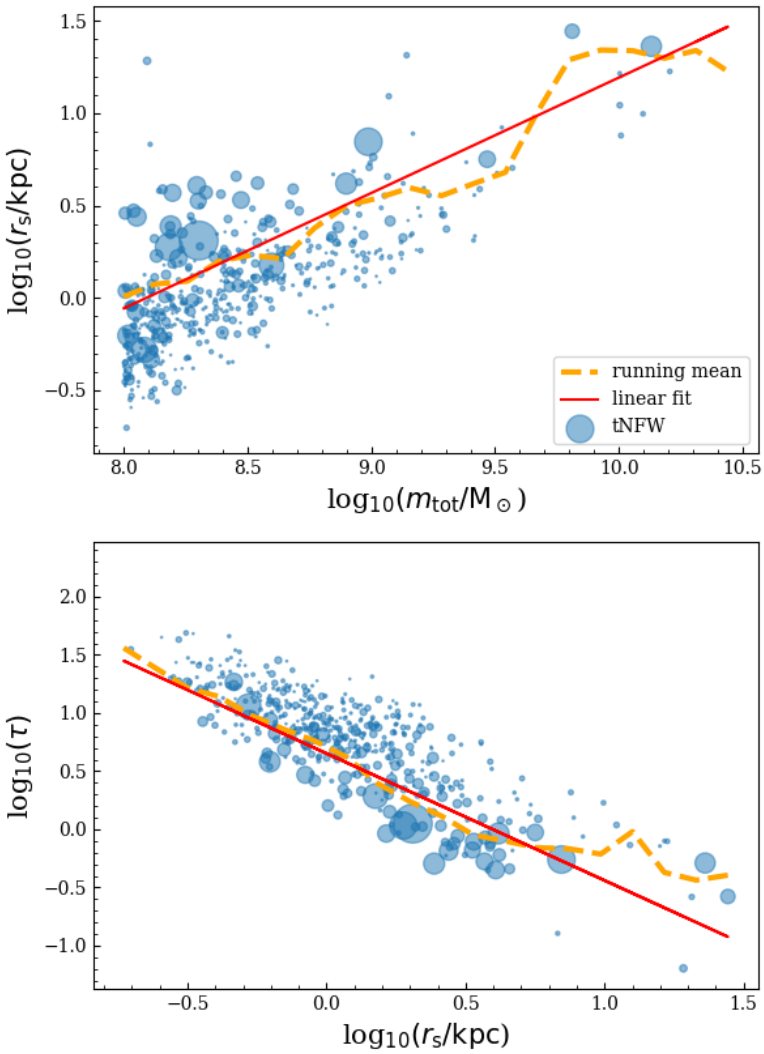


Figure 3.2: Relations between $M_{\mathrm{tot}}$, $r_{\mathrm{s}}$ and $\tau$ for subhaloes in an annulus between $1.0''$ and $3.0''$ encompassing the Einstein radius, at snapshot $z = 0.183$. The relations were obtained by rotating the lensing galaxy and its subhaloes 10000 times and selecting those subhaloes that fall in the region of interest in projection. The area of each blue point represents how many times a subhalo falls in this region. The dashed orange and solid red lines show the running means and best fit linear relations for the data taking account of the weight of each data point.

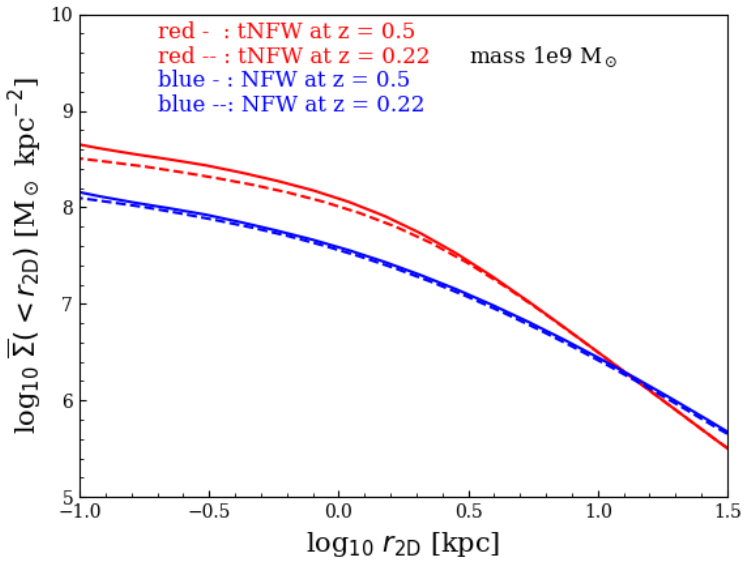


Figure 3.3: Interior mean surface density profiles of tNFW and NFW at $z = 0.22$ (dashed lines) and $z = 0.5$ (solid lines). Red lines are the tNFW profiles and blue lines show the NFW profiles. All the haloes plotted here have mass of $10^9$ $M_\odot$. For tNFW, the mass refers to the total mass, while for NFW, the mass refers to $M_{200}$.

where the errors are the $1\sigma$ scatter determined from the bootstrap resampling.

In Fig. 3.3, we show the interior mean surface density profiles of tNFW subhaloes of mass $M_{\rm tot} = 10^9$ $M_\odot$ for two different lens redshifts, and the same profiles of central haloes of mass $M_{200} = 10^9$ $M_\odot$ for two different lens redshifts. The profiles of the tNFW model were derived from the mean linear relations between $M_{\rm tot}$, $r_s$, and $r_t$ described above. Clearly, the tNFW profiles are more compact and have higher amplitude than the NFW profiles of the same mass.

### 3.2.2 Sensitivity Mapping

A process called sensitivity mapping is performed to quantify the detectability of a perturbing halo that is nearby a strongly lensed source. One begins by modeling a strong lens dataset to infer an accurate model for the lens's mass and source's light (Nightingale et al., 2019). Using this model, one can then simulate a new realization of the strong lens which includes a dark matter perturber at a given

$(x, y)$ position in the image-plane and with an input mass and redshift. This simulated dataset assumes the same image resolution and PSF of the true dataset and also has consistent signal-to-noise properties.

The mock dataset is now fitted with two lens models: (i) a lens mass model which does not include a dark matter perturber and; (ii) a lens mass model which does. By comparing a goodness-of-fit measure of each model-fit (e.g. the maximum log likelihood value) one therefore quantifies how sensitive the lens dataset is to a dark matter perturber, given its input location and mass. If the lens model including the perturber has a much improved goodness-of-fit compared to the model which does not, the perturber was necessary to fit the data accurately, indicating that the strong lens data is sensitive to perturbers at the location and with that mass. If the goodness-of-fits are comparable, the perturber does not improve the lens model and therefore it is too far from the lensed source or too low mass to be detectable.

It is necessary to perform two full fits to each mock dataset, to infer the maximum log likelihood of each model, for two reasons. First, the image fluxes we are fitting have noise and thus the maximum likelihood model may not be the true input model (although see Amorisco et al., 2022). Second, due to the existence of a small perturber in the mock data and the possible degeneracy between it and the main lens mass, when fitting a model without a small perturber, the maximum likelihood model is offset with respect to the true input and can only be found via a full fit.

By repeating this process on a grid of perturber ($x$,$y$) location, mass and redshift one produces a sensitivity map. In this work, we assume a grid of 27 steps in the $y$ and $x$ directions, and a grid of 25 steps in redshift between $z = 0.02$ and $z = 0.98$. For a given object, its angular size decreases with redshift, so the angular size of the sensitive region also decreases with redshift. To save computational resources, we decrease the angular size of the explored region as the redshift increases. Furthermore, for the same reason, rather than exploring a grid of mass values, we look for the lowest value of the perturber's mass that corresponds to the goodness-of-fits threshold of detection by a binary search algorithm (in $\log_{10}$

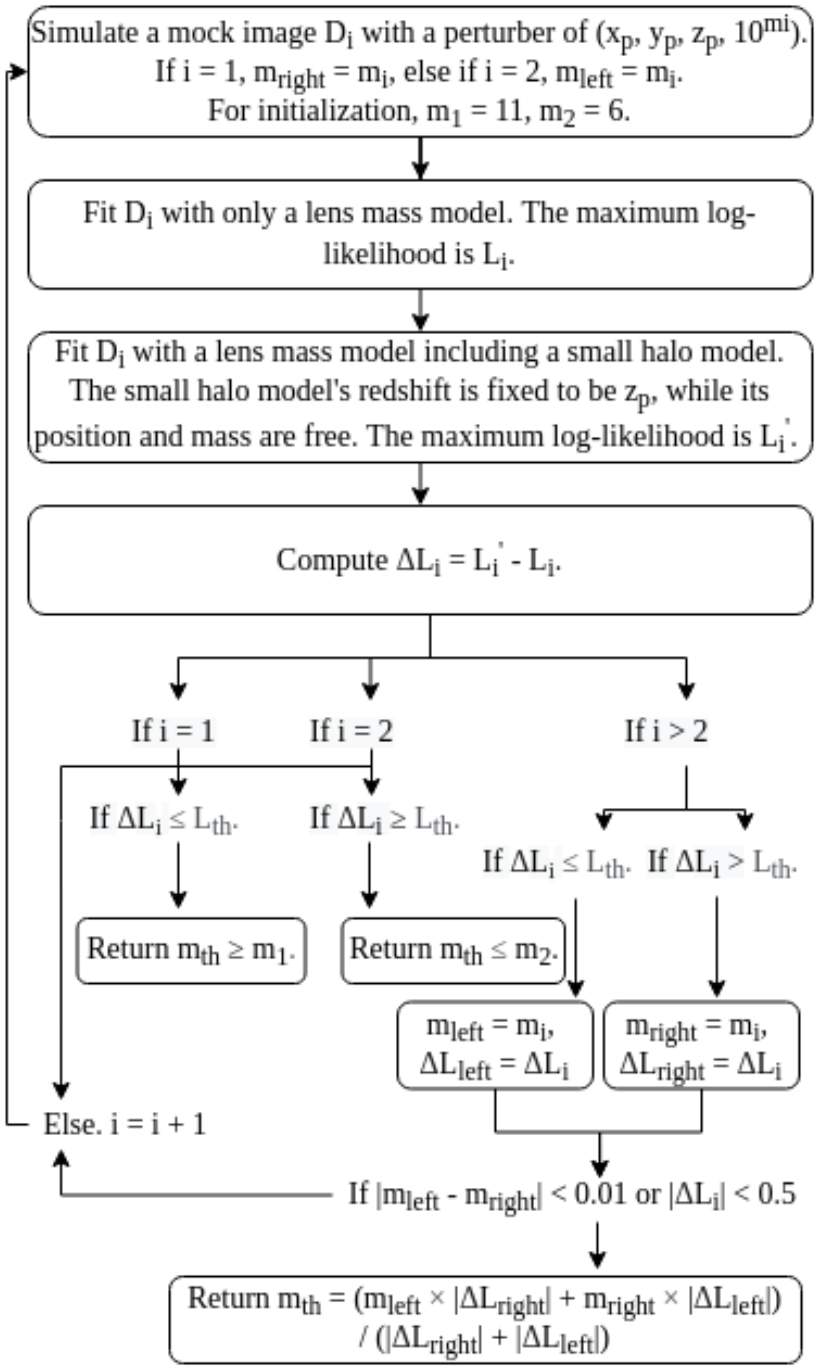


Figure 3.4: The binary search procedure for $m_{\rm th}$ at ($x_{\rm p}$, $y_{\rm p}$, $z_{\rm p}$). $L_{\rm th}$ is the detection threshold and throughout this paper, we take it to be 10.

scale). The mass boundaries for the binary search are $10^6$ $M_\odot$ and $10^{11}$ $M_\odot$ and the stop criterion for the iteration is that $|\Delta \log_{10}(m)| < 0.01$. For every grid cell, we simulate a new strong lens dataset and fit it with the two lens models described above using the nested sampling algorithm `dynesty` (Speagle, 2020). For efficiency, we use tight priors on every model-fit that exploit our knowledge of what values of lens mass model and source model were used when simulating the data. This could negatively impact `dynesty`'s estimate of the Bayesian evidence, therefore we opt to simply compare maximum log likelihood values when producing a sensitivity map. At the end, the "sensitivity map" is a grid of ($x_\mathrm{p}$, $y_\mathrm{p}$, $z_\mathrm{p}$, $m_\mathrm{th}$), which means that a perturber at ($x_\mathrm{p}$, $y_\mathrm{p}$, $z_\mathrm{p}$) is detectable when it has a mass over the threshold mass, $m_\mathrm{th}$. Please note when fitting the mock image with a lens mass model including a perturber model, the perturber model's redshift is fixed to be $z_\mathrm{p}$ while its position and mass are free (the concentration follows Ludlow et al. (2016) which is a function of $m$ and $z_\mathrm{p}$.). Fig. 3.4 summarizes the procedure of computing $m_\mathrm{th}$ for at ($x_\mathrm{p}$, $y_\mathrm{p}$, $z_\mathrm{p}$). Our method is conceptually analogous to that of Amorisco et al. (2022), albeit there are differences in the fitting algorithm used.

### 3.2.3 Detection threshold

L17 and D18 have derived the detection threshold of a line-of-sight perturbing halo by directly modelling the lensing effect of a subhalo, i.e. a perturber at the redshift of the lens. If a line-of-sight halo of mass, $m$, best fits the lensing effect of a subhalo of mass, $m_\mathrm{sub}$, then this is defined as the effective mass of the line-of-sight halo. If a line-of-sight halo has an effective mass larger than the detection threshold for the subhalo, it is considered detectable. However, in many cases, the line-of-sight halo at redshift $z$ is not a good description of the image perturbation. As a result, although one can always find a particular value of $m$ for a line-of-sight halo that gives the smallest $\chi^2$ in the fit of the image distortion generated by the subhalo, the two models are not equivalent.

In Fig. 3.5, we show how the deflection angles produced by our lens are altered by

the addition of a perturbing halo. The main lens is a singular isothermal sphere (SIS) located at $z = 0.5$, at the centre of the image, and the source is at $z = 1.0$. The upper panel shows the deflections caused by a $M_{200} = 10^9$ $M_\odot$ NFW halo located on the main lens plane; the colour indicates the amplitude of the deflections (in units of $0.001''$) and the arrows mark their directions. In this case there are no non-linear multi-plane lensing effects, and so the change in the deflection angles due to a perturbing halo are just the deflection angles of the perturbing halo itself, which point towards the perturber's centre. In the lower panel we plot the change in the total deflection angles when a $M_{200} = 10^{8.67}$ $M_\odot$ NFW halo at $z = 0.2$ perturbs the lensing due to the main lens (subtracting the total deflection angle with the deflection caused only by the main lens). Because of multi-plane lensing effects (Schneider et al., 1992, Fleury et al., 2021) the change in the deflection angles are no longer isotropic about the perturber centre (Gilman et al., 2019, He et al., 2022b). Tracing from the observer backwards, the deflection of light rays by the perturber alters where those rays intersect the main lens plane, which in turn alters the deflection angles those rays receives from the main lens. It is clear that the lensing effects of line-of-sight perturbers at different redshifts cannot be reproduced by appropriately scaled subhaloes since the deflection patterns in the two cases are completely different. Note that the mass of the line-of-sight perturber in the lower panel was chosen to best reproduce the deflection angle field in the annulus between $1.0''$to $2.0''$of the case in the top panel with a $10^9$ $M_\odot$ halo in the main lens plane (following Eq. 15 in D18), so according to L17 and D18, the perturbers in the two panels have the same "effective mass", but clearly they have quite different effects.

Degeneracies between the effects of the low-mass perturber and the main lens can also affect our estimation. As suggested in Fig. 3.5, the deflection angles far from the perturber's centre can be easily absorbed by slightly shifting and stretching the main lens. Furthermore, the degeneracies between the effects of perturbers and the main lens galaxy can be different at different redshifts due to their distinct

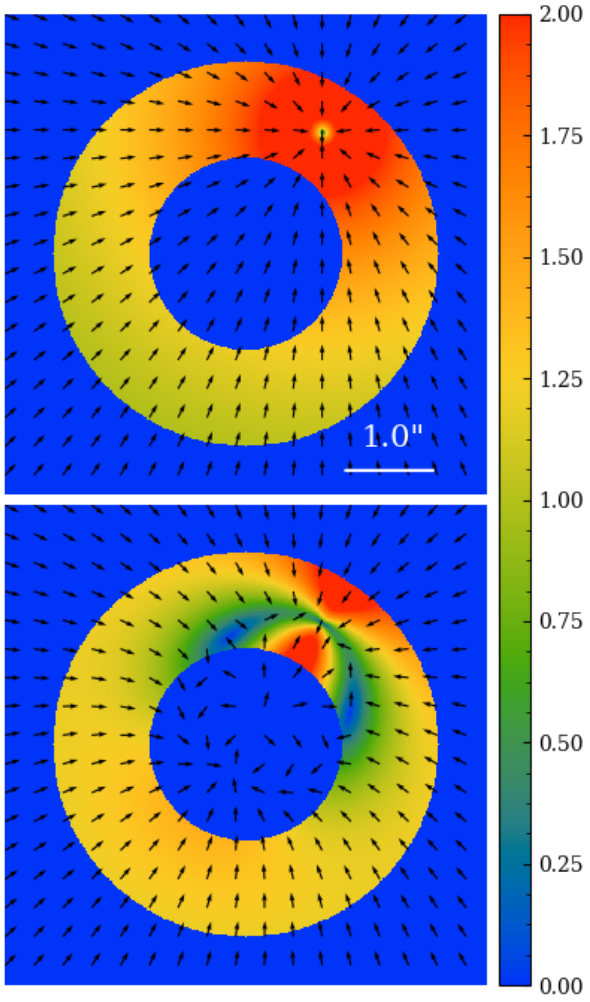


Figure 3.5: Comparison of the deflection angles caused by a $10^9$ $M_\odot$ NFW halo at lens plane ($z = 0.5$) (upper panel) and a line-of-sight NFW halo in front of the lens plane ($z = 0.2$) whose mass is $10^{8.67}$ $M_\odot$, as derived by fitting the deflection angle of the NFW halo at the main lens plane (lower panel). Both panels are derived by subtracting the total deflection angles of both main lens and perturber with the deflection generated only by the main lens. The colours show the amplitude of deflections (in units of $0.001''$). The arrows represent the direction of deflection angle vectors. In the lower panel, the asymmetric pattern of arrows at the centre of the main lens is subject to numerical noise because the deflection angle at the exact centre of an SIS is not well defined, where the profile's density is infinite and the density gradient (deflection angle) is not continuous. Since the perturber and the SIS are not on the same plane in the lower panel case, the inaccurate angles next to the SIS's centre are then not perfectly subtracted, which results in the asymmetric pattern of arrows in the centre. The arrows in other locations are reliable.

deflection patterns, making the problem even more complicated.

In order to take into full account the complex effects discussed above, in this paper we no longer compare deflection angles as L17 and D18 did. Instead, to quantify the lensing effects of perturbers at different redshifts we directly fit image fluxes, a procedure that more closely reproduces what would happen on real data. We now define a new threshold for detection through the log-likelihood* improvement brought about by including a perturber when fitting lensing images. Specifically, we first fit the mock image with only a main lens and record the maximum log-likelihood value. We then fit the same image with a model containing both a main lens and a perturbing halo and record the log-likelihood of the best-fit model as well. If the log-likelihood difference between the two fits is larger than a pre-established threshold, we consider the perturber to be detectable.

In the tests we have carried out, the uncertainty in the modelling comes exclusively from the statistical noise in the image data. The log-likelihood difference can be directly related to a significance level, with a log-likelihood difference of 10 roughly corresponding to $4 \sim 5\sigma$ significance. Note that in real observations, a threshold based on the log-likelihood difference or the Bayesian evidence might not be readily related to the true significance of a detection due to the possible presence of various systematic effects in the data and analysis method (Vegetti et al., 2012, Ritondale et al., 2019).

### 3.2.4 Number density of perturbers

For each mock lens, we calculate the number of line-of-sight perturbing haloes within a radius of 3 arcsec. The total number of line-of-sight perturbers with a mass in the range $[m_{\rm low}, m_{\rm high}]$ in a light cone corresponding to the $i^{\rm th}$ pixel can be written as,

*The log likelihoods are defined using a natural (base e) logarithm.

$$N_{\rm los} = \int_0^{z_s} \int_{m_{\rm low}}^{m_{\rm high}} \frac{{\rm d}^2 N}{{\rm d}m\,{\rm d}V} \frac{{\rm d}V_{\rm sens}}{{\rm d}z}\,{\rm d}m\,{\rm d}z\,, \tag{3.5}$$

where $\frac{d^2N}{dmdV}\,(z)$ is the halo mass function at redshift $z$ (e.g. Sheth et al., 2001) and

$${\rm d}V_{\rm sens} = \Omega_{\rm sens}(m,z)\,\chi^2 \frac{{\rm d}\chi}{{\rm d}z}\,{\rm d}z\,, \tag{3.6}$$

where $\Omega_{\rm sens}(m,z)$ is the total solid angle corresponding to the areas on the redshift plane of $z$ that are sensitive to perturbers more massive than $m$.

For comparison, we also calculate the number of detectable subhaloes for each mock image. For CDM, high-resolution N-body simulations have shown that the mass function of subhaloes follows a power law (Springel et al., 2008). Thus, the cumulative perturber density of subhaloes in the mass range, $[m_1, m_2]$, in a host halo of mass, $M_{200}$, may be written as,

$$\Sigma_{\rm sub,cdm}(m_1 < m < m_2 | M_{200}) = \frac{\Sigma_0}{1-\alpha}\left(\left(\frac{m_2}{{\rm M}_\odot}\right)^{1-\alpha} - \left(\frac{m_1}{{\rm M}_\odot}\right)^{1-\alpha}\right)\,, \tag{3.7}$$

where $\alpha = 1.9$ (Springel et al., 2008, Gao et al., 2012) and $\Sigma_0$ is a normalization parameter that depends on $m_{200}$ and can be determined from cosmological simulations. In this work, we estimate this normalization using the same simulation (Richings et al., 2021) that we used to extract the density structure of subhaloes.

To obtain a sufficiently large sample of subhaloes within the region of interest in order to derive the subhalo mass function, we follow the same strategy as before: we rotate the lens 10000 times, and only select those subhaloes that fall on the region of interest in projection. We compute the average number of subhaloes of mass $10^7 \sim 10^{11}$ ${\rm M}_\odot$ for each projection. To obtain an estimate on the error, we repeat the same procedure 200 times, each time resampling from all the subhaloes in the simulation before projecting along 10000 different lines-of-sight. We take the median value and $1\sigma$ limits as our estimate. Assuming $\alpha = 1.9$, for a lens at $z = 0.22$, we derive the normalization (from the snapshot at $z = 0.183$) to be $(6.7 \pm 0.6) \times 10^5\,{\rm arcsec}^{-2}$. For a lens at $z = 0.5$, we derive the normalization (from the snapshot at $z = 0.503$) to be $(2.3 \pm 0.2) \times 10^6\,{\rm arcsec}^{-2}$.

To ensure that our result based on this one particular simulated halo is not an outlier, we compute the normalisation of the subhalo mass function from haloes in the EAGLE simulation in a similar way as above. Due to the poorer resolution of EAGLE, when calculating the normalisation we only count subhaloes of mass $10^9 \sim 10^{11}$ $M_\odot$. We select haloes in EAGLE with mass within 0.1 dex of that of the main halo used in this study and apply the same method to compute $\Sigma_0$. For $z = 0.22$, there are 78 haloes and $\Sigma_0 = (4.3 \pm 1.5) \times 10^5$ arcsec$^{-2}$, where the errors indicate the $1\sigma$ (34%) scatter. For $z = 0.5$, there are 63 EAGLE haloes and $\Sigma_0 = (1.8 \pm 0.9) \times 10^6$ arcsec$^{-2}$. We see that the number of EAGLE subhaloes around halos of a given mass has a large scatter and there can be differences of $2 \sim 3$ times within EAGLE itself. At $z = 0.22$, the value of $\Sigma_0$ obtained for the halo analysed here is $1\sigma$ high compared to the distribution in EAGLE, while at $z = 0.5$, the results are in even better agreement. In conclusion, the value of $\Sigma_0$ derived in this work is comparable to values for EAGLE haloes and our results based on one particular resimulation should be representative.

## 3.3 Results

In Fig. 3.6 we show the sensitivity function for our mock lens images as a function of redshift. Each sub-panel displays a map of $m_{\rm th}$ (see colour bar) for line-of-sight haloes placed at a given redshift plane, for 5 redshifts. In all cases, the source is at $z = 1$ and the lens at $z = 0.5$, except in the third row, where the lens is at $z = 0.22$. For all mock lenses, the threshold mass of a detectable perturber is lowest near the lens redshift and raises rapidly towards both higher and lower redshifts; however, the general pattern of the sensitivity maps remains similar at each redshift. This pattern varies considerably from one lensing system to another. Visually, it appears similar to the corresponding pattern of the lensing image. The value of $m_{\rm th}$ is lowest in the region where the surface brightness is highest and highest in the region where there is no light. Although the sensitivity maps for

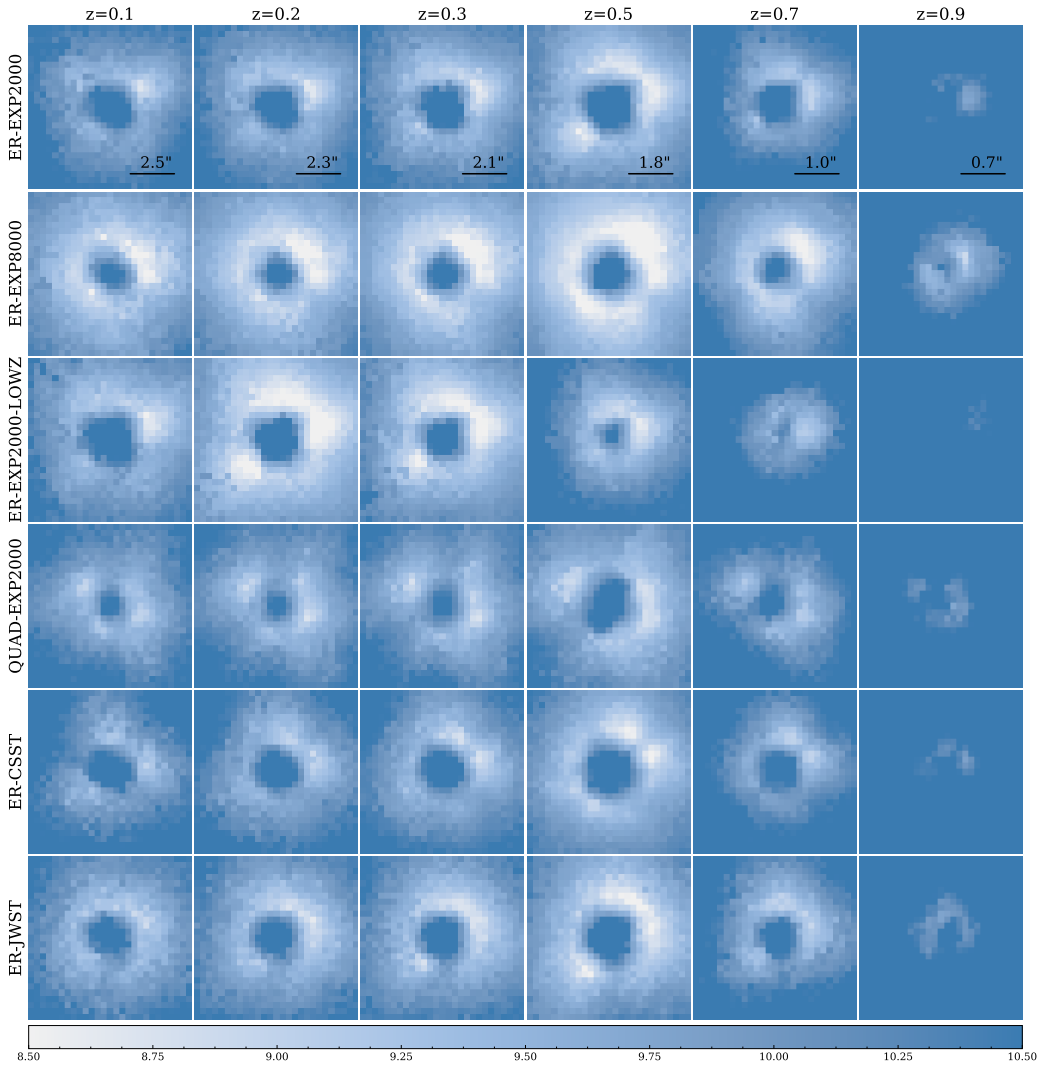


Figure 3.6: The sensitivity function of LOS perturbers. Each subpanel shows the detection limit for a perturber (a line-of-sight NFW halo) placed at a given redshift plane. The colour bar gives the scale of $\log_{10}(m_{\rm th}/{\rm M}_{\odot})$. 6 panels on the same row show the sensitivity function for a mock lens at 6 redshifts: 0.1, 0.2, 0.3, 0.5, 0.7, 0.9. For every column, the image size is marked by a scale bar in the top row. The label of each mock is given at the left of each row. In all cases the source is at $z = 1$ and the lens is at $z = 0.5$, except in the third row, where the lens is at $z = 0.22$. The image sizes decrease with the redshift is because the angular size of regions of interests decreases with the redshift.

different systems are quite different, the trend of their evolution with redshift is similar.

The ability to detect low-mass dark haloes increases significantly with the exposure time of the imaging. For our fiducial 2000s exposures, our lensing systems are

sensitive to line-of-sight perturbers of mass $\sim 10^8$ $M_\odot$ only around the lens redshift. For 8000s, however, perturbers of mass $\sim 10^8$ $M_\odot$ can be detected over a much broader redshift range, from $z = 0.1$ to $z = 0.7$. In the bottom two rows of Fig. 3.6, we show the sensitivity function for the imaging quality achievable with the CSST and JWST, which have different resolutions. We find that with a lower image resolution, CSST lensing images are still sensitive to perturbers of mass $\sim 10^8$ $M_\odot$, although the overall sensitivity is somewhat lower than with HST resolution. While for the JWST resolution imaging, the sensitivity is higher.

We now turn our attention to the all-important question of whether the distortions to the Einstein rings are dominated by line-of-sight perturbers or by subhaloes. We trace the position of each pixel on the image plane at a series of redshifts and calculate the threshold mass for detection, $m_{\rm th}\,(z)$. In Fig. 3.7, we plot the ratio, $\log_{10}\,(m_{\rm th}(z)/m_{\rm th}(z_l))$, as a function of redshift, $z$, for our different mock lensing systems. The colour bands are the regions enclosing 70% of the pixels, while the means are shown as solid lines. For comparison, we also plot the relation and scatter derived by D18 in grey. In D18 (as well as in L17), a line-of-sight halo at lower redshift is easier to detect than a halo of the same mass at the lens redshift. Our new calculations predict the different behaviour. For all configurations, the detection threshold mass increases with $\Delta z = |z - z_{\rm l}|$. For lenses at redshift $z_{\rm l} = 0.5$, the detection threshold for line-of-sight haloes at $z = 0.1$ is $\sim 0.3$ dex higher than for haloes at $z_{\rm l}$.

To predict the number density of detectable subhaloes, we calculate sensitivity maps for subhaloes with truncated NFW profiles, as described in Section 3.2.1. In Fig. 3.8, we compare sensitivity maps for subhaloes (right) to those for line-of-sight haloes placed at the lens redshift of the same lensing system (left). The maps on the left are the same as in the subpanels of Fig. 3.6 at the corresponding (lens) redshift, while the right panels show the detection limits for subhaloes. The mass of an NFW halo is defined to be $M_{200}$, while the mass of the subhalo (tNFW) is defined as the total mass given by Eq. 3.1. As expected, the threshold mass for

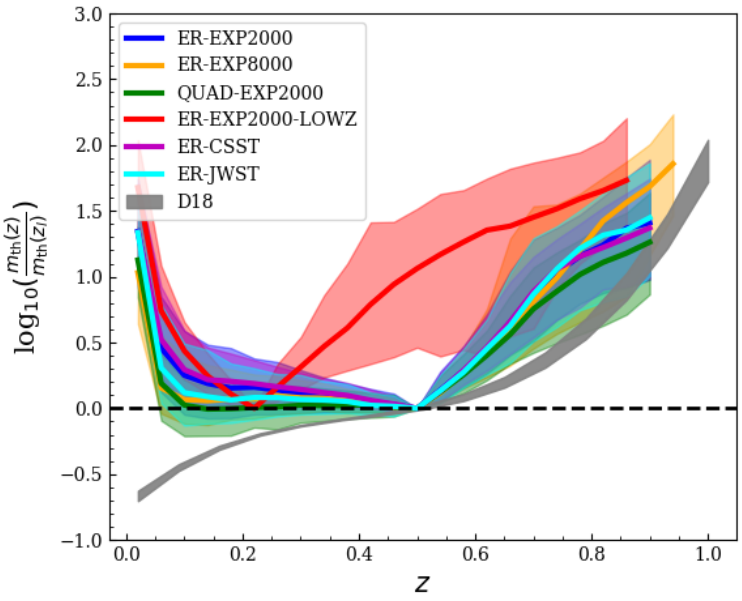


Figure 3.7: The mass threshold-redshift relation, $\log_{10}\left(\frac{m_{\rm th}(z)}{m_{\rm th}(z_l)}\right)$, as a function of redshift, $z$, for all of our mock settings. Four of them have a lens at $z = 0.5$ and a source is at $z = 1$, while one has a lens at $z = 0.22$. The relation is calculated for each pixel on the image plane. The shaded regions enclose 70% of the pixels. For comparison, the relation and the scatter derived by D18 for our fiducial setting are shown in grey. The relations shown here are only for line-of-sight NFW perturbers and there is no subhalo (tNFW perturbers) involved in this comparison.

detecting a subhalo is lower than that for detecting an NFW halo of the same mass by about 0.5 dex, because a subhalo is much more compact than a halo of the same mass. In the following calculations, we will use the sensitivity maps for the tNFW haloes to estimate the number of detectable subhalo perturbers.

In the left panel of Fig. 3.9, we show, as solid lines, the expected cumulative number of detectable line-of-sight perturbers derived, as a function of redshift; different colours correspond to different systems. We can see that the number of detections rises sharply around the lens redshift and then becomes flat. For the two different mock lenses at $z_{\rm l} = 0.5$, with a 2000s exposure (blue and green lines), 0.85 and 0.64 line-of-sight haloes can be detected per lens. The differences between the two configurations are small, which may be due to the fact that the two mock images have a similar number of high S/N pixels. For the lens at $z_{\rm l} = 0.22$, the number of expected detections decreases to about 0.39 per lens (red line), which

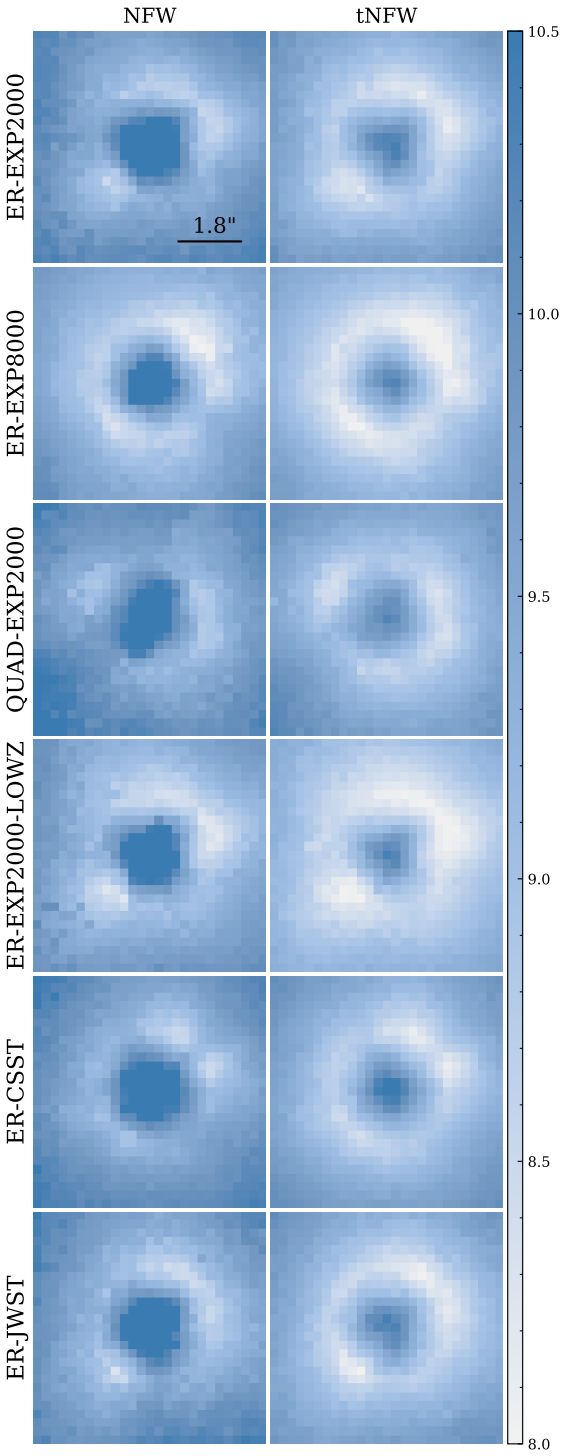


Figure 3.8: Sensitivity maps for NFW line-of-sight perturbers (left) and for tNFW subhalo perturbers (right). In all cases the source is at $z = 1$ and the lens at $z = 0.5$, except in the fourth row, where the lens is at $z = 0.22$. All perturbers are on the same redshift plane of the main lens.

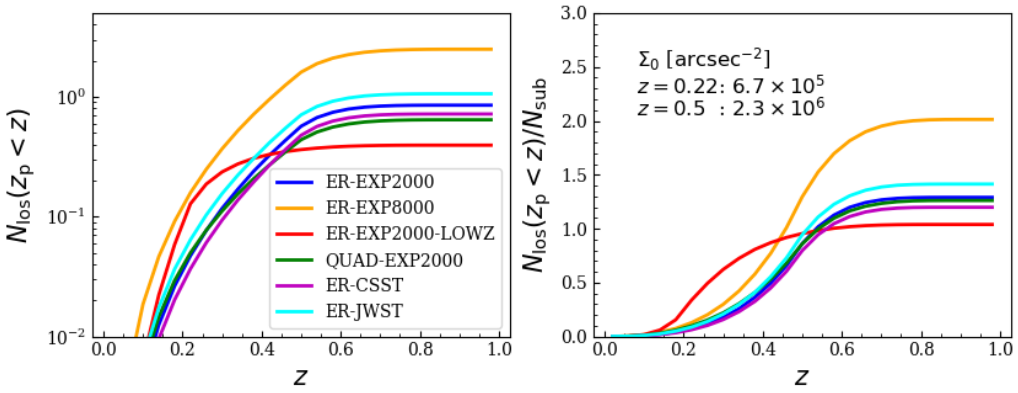


Figure 3.9: The cumulative number of detectable line-of-sight perturbers per lens for different lens configurations as a function of redshift (left). The number of line-of-sight haloes relative to the number of detectable subhaloes as a function of redshift (right). In all cases the source is at $z = 1$ and the lens at $z = 0.5$, except for the red line, where the lens is at $z = 0.22$. The normalization of the subhalo mass function at two main lens redshifts is also listed on the right panel.

is $\sim 45\%$ of that of the $z_l = 0.5$ lenses. Fig. 3.9 also shows that a high S/N ratio (orange line) helps reveal low-mass perturbers: if the exposure time increases to 8000s, the number of detectable line-of-sight perturbers increases to 2.5 per lens. We also see that by increasing the image resolution, the detectability of small perturbers increases. With CSST resolution only $\sim 0.72$ line-of-sight perturber can be detected per lens, but with a higher resolution as the JWST, the detectable number increases to 1.06 per lens.

On the right panel of Fig. 3.9, we show the relative importance of line-of-sight haloes and subhaloes. According to our calculation, for mock lenses at $z_l = 0.5$, the predicted number of detectable line-of-sight haloes is about 1.3 times the number of detectable subhaloes. For the low redshift mock, $z_l = 0.22$, the line-of-sight halo contribution is lower and close to that of subhaloes. For the high S/N mock, the relative importance of line-of-sight haloes increases, such that it becomes $\sim 2.0$ times the number of detectable subhaloes.

## 3.4 Discussion and Conclusion

In this chapter we have revisited a key question relevant to the search for low-mass haloes in strong lensing systems: what is the relative contribution to the sensitivity function of line-of-sight (main) haloes versus subhaloes in the lens. The main difference between this and previous works is that, instead of fitting the deflection angle map or an idealized image set, we have quantified the expected number of line-of-sight perturbers by means of realistic modelling carried out on a set of mock lensing images with realistic levels of noise. Contrary to previous work, we find that the lensing effect of a line-of-sight perturber is largest if the perturber is located near the lens redshift, and the strength of the signal decreases rapidly as the redshift difference between the perturber and the lens plane increases. Two reasons account for the difference: firstly, previous work assumed that the effects of a perturber at one redshift could be accounted for by a perturber at a different redshift, while Fig. 3.5 demonstrates that the effects can be quite different because of multi-plane lensing effects; secondly, previous work did not take into account the degeneracy between the main lens and the small halo in the fitting process, whereby changes to the main lens model can absorb a significant part of the small perturber's lensing signal. Our calculation shows that the contribution from line-of-sight haloes is still important, but does not dominate the total number of detectable perturbers for most of our mock lenses as was previously thought: previous studies overestimated the expected total number of perturbers.

In a sense, our new results present an unwanted challenge for the interpretation of future detections of low-mass haloes. Unlike the line-of-sight field dark matter haloes of interest (whose masses are below the minimum required to make a galaxy) which are unaffected by baryons and thus retain their pristine structure, subhaloes are changed by their environment, e.g. tidal stripping and disruption. A detailed quantification of these processes needs understanding in detail the structure of the galaxy, including its baryonic component. This requires full modelling of galaxy

formation such as that presented by Richings et al. (2020) for a lens system of the kind in which we are interested for low-mass halo and subhalo detection.

In this chapter we have assumed, for simplicity, that the distribution of line-of-sight haloes is not correlated with the lens host halo. In reality, line-of-sight haloes are more strongly, and anisotropically clustered around the region of the host halo than average (Richings et al., 2021). In a recent paper, Lazar et al. (2021) investigated the number density of line-of-sight perturbers in the simulations from the FIRE* and IllustrisTNG† projects; they find that the number of haloes correlated with the lens is about 35% larger than average, in agreement with the results of Richings et al. (2021). Future work aimed at constraining the nature of the dark matter from strong lensing data will need to take this sort of correlation into account.

One caveat of our work is that we do not consider the scatter in the mass-concentration relation. For a halo or subhalo of a given mass, the higher the concentration, the higher the central density and lensing signal. A recent study by Minor et al. (2021) shows that this effect can introduce a bias of 3 for a subhalo of mass $10^9$ $M_\odot$ and 6 for one of mass $10^{10}$ $M_\odot$. In a more recent study, Amorisco et al. (2022) show that the scatter in the mass-concentration relation boosts the detection of line-of-sight perturbers and helps distinguish between CDM and WDM. A halo of mass less than $m_{\rm th}$ but of higher than average concentration may still produce a strong enough lensing signal to be detected and vice versa. When the halo or subhalo mass function rises at the low mass end, the effect of scatter in the mass-concentration relation can boost the number of detectable perturbers significantly, helping distinguish different dark matter models. We remind our readers that the results discussed here are for analyses of resolved lensing systems where the sources are extended. Effects of mass-concentration relation and multi-plane lensing have been taken into account in previous similar studies on constraining low-mass perturbers' abundance in lensing systems with an unresolved source (Gilman et al.,

*http://fire.northwestern.edu
†https://www.tng-project.org

2019, 2020c).

In this chapter, we also show that the ability to detect low-mass haloes increases with the exposure time of the image. For example, increasing the exposure time from 2000s to 8000s, increases the number of total detectable perturbers by a factor of 2. At face value, deeper imaging may seem not quite as efficient an observing strategy as observing more lenses. However, longer exposure times crucially increase the sensitivity to haloes of lower mass, which are important in constraining the identity of the dark matter.

Chapter 4

# Effects of lens galaxy's complexity on subhalo inference with a cosmological simulation

**Abstract**

We test commonly-used techniques for explicitly detecting subhaloes superposed in images of strongly lensed galaxies. For the lens we take a simulated galaxy in a $\sim 10^{13}$ $M_\odot$ halo grown in a high-resolution cosmological hydrodynamical simulation, which we view from two different directions. Though the resolution is high, we note the simulated galaxy still has an artificial core which adds additional complexity to the baryon dominated region. To remove particle noise, we represent the projected galaxy mass distribution by a series of Gaussian profiles which precisely capture the features of the projected galaxy. We first model the lens mass as a (broken) power-law density profile and then search for small haloes. Of the two projections, one has a regular elliptical shape, while the other has distinct deviations from an elliptical shape. For the former, the broken power-law model gives no false positives and correctly recovers the mass of the superposed small halo, but for the latter we find false positives and the inferred halo mass is overestimated by $\sim 4-5$ times. We then use a more complex model in which the lens mass is decomposed into stellar and dark matter components. In this case, we show that we

can capture the simulated galaxy's complex projected structures and correctly infer the input small halo. By improving the lens mass model, we argue this enables more robust subhalo inference that can detect lower mass subhaloes, strengthening the technique's ability to test alternative models of dark matter.

## 4.1 Introduction

Strong gravitational lensing serves as a promising tool to probe the existence of small invisible dark matter haloes. These dark haloes perturb the images of lensed galaxies when they fall along the path of light from the source to the observer (Koopmans, 2005, Vegetti and Koopmans, 2009a,b). The perturber's mass of interest is usually less than 0.1% that of the lens galaxy, necessitating percent level accuracy of the main lens's mass, which places stringent requirements on the model of the lens galaxy's mass distribution. Inaccuracies in the lens mass model may create "false-positive" detections, where the low-mass perturber could "fill in" for the mass model's missing complexity. Previous studies have discussed false-positive subhalo detections (Vegetti et al., 2010, Ritondale et al., 2019), where they apply strict criteria to ensure all detections are genuine. This includes requiring a high enough increase of Bayesian evidence that tests on mock data demonstrate the signal cannot be due to an inaccurate mass model (Vegetti et al., 2012) and verifying that a consistent low-mass perturber detection is made when pixelised corrections to the gravitational potential are applied (Koopmans, 2005, Vegetti and Koopmans, 2009a, Vegetti et al., 2010, 2012). In certain lenses these potential corrections clearly account for missing complexity in the lens galaxy's mass, thereby correctly flagging a candidate detection as a false positive.

This motivates the investigation of more complex lens models, which could improve the inference on low-mass perturbers by accounting for this missing complexity in the lens galaxy's mass. The detections of low-mass perturbers so far all assume a simple parametric model for the lens's mass, the elliptical power-law (Tessore and

Metcalf, 2015) with an external shear (Hezaveh et al. (2016) also included a fourth-order multipole term). However, recent studies have highlighted deficiencies with this model: Cao et al. (2021) fitted this model to strong lenses simulated using mass models derived from dynamical models of nearby SDSS-IV MaNGA (Bundy et al., 2015) early type galaxies and showed this can bias the measurement of the local density slopes around the Einstein ring by 13%; Gomer and Williams (2021) and Van de Vyvere et al. (2022) discuss how departures from elliptical symmetry may affect $H_0$ inference in lensed quasars; Nightingale et al. (2019) have also showed that departures from elliptical symmetry are observed in the luminous emission of three strong lenses.

In this chapter, we therefore use a hydrodynamic simulation to test the robustness of different parametric lens mass models, focusing on their efficacy for the task of detecting individual low-mass perturbers. To keep it simple, through this chapter, we limit our tests only on subhaloes, perturbers within the lens galaxy, and leave those line-of-sight perturbers for our future work. By using a simulation, we can compare the lens galaxy's true complex mass distribution to the lens model we fit and if it fails understand why. We perform two tests: (i) we do not add a subhalo to the lens galaxy when generating the mock data and investigate whether a lens model with a subhalo produces a false-positive signal; (ii) we include a subhalo when creating the mock data and test how accurately its mass and position are recovered. We first apply an extension of the commonly used power law profile to fit the main lens (O'Riordan et al., 2019, 2020, 2021), followed by a "decomposed" model which models the lens mass as a combination of stars and dark matter (Dye and Warren, 2005, Nightingale et al., 2019). Our goal is to understand whether modelling the lens mass as a power law profile is sufficient for detecting subhaloes, and if not, whether there is a better model that can provide a correct inference.

Hydrodynamic simulations have previously been used to simulate galaxy-galaxy strong lensing images (Metcalf and Petkova, 2014, Xu et al., 2017, Mukherjee et al., 2018, Despali et al., 2020, Enzi et al., 2020, Mukherjee et al., 2021, Ding et al., 2021).

Converting particle data into a corresponding deflection angle field (necessary for lensing) is non-trivial. A common problem is that the mass profiles of galaxies found in hydrodynamic simulations have a sub-kpc core in their centre. The strong lens imaging then produces a bright central image feature, which is not observed in real strong lenses (Bolton et al., 2012, Shu et al., 2016). These cores are believed to be due to the limited resolution of the simulations, with previous works assuming a particle resolution of $\sim 10^5$ $M_\odot$. Our simulation, which has a particle resolution $\sim 10$ times that of Illustris-1, still forms a core and central image. We incorporate this feature into our lens modeling such that we can still investigate dark matter subhalo detection. We also mitigate systematic effects related to particle noise in the simulation (Xu et al., 2009) and truncation effects which introduce an artificial shear (Van de Vyvere et al., 2020, Ding et al., 2021).

Testing with galaxies from the Illustris simulation (Vogelsberger et al., 2014), Xu et al. (2017) demonstrated that deviations of simulated galaxies from a simple elliptical power-law profile affect inference on the Hubble constant. More recently, Enzi et al. (2020) used 10 galaxies from the Illustris-1 simulation to test the power-law lens assumption for substructure lensing, and showed no degeneracy between the complexity of the true mass distribution of their mock lenses and the inferred substructure abundance. However, their work focused on the statistical properties of subhaloes' signals and did not test individual subhalo detection. To fully understand how the use of simple parametric lens models affects the detection of individual substructure, testing with mock lenses extracted from simulations is necessary.

This chapter is structured as follows: in Section 4.2, we introduce our simulation data and the way we simulate strong lensing images from particle data. In Section 4.3, we introduce how we model the lensing images and search for subhaloes. In Section 4.4, we show the power law fitting results. In Section 4.5, we introduce a more complex lens model where we model the lens' stellar and dark components separately and then we show how it behaves for our tests. In Section 4.6, we dis-

cuss our results. Finally, in Section 4.7, we summarize our results. Throughout the chapter we adopt the Planck cosmology (Planck Collaboration et al., 2016), of which $H_0 = 67.7\,\mathrm{km\,s^{-1}\,Mpc^{-1}}$, $\Omega_m = 0.307$ and $\Omega_\Lambda = 0.693$.

## 4.2 Mock Lensing Images

### 4.2.1 Particle data

We create our lens galaxy by using data from the same cosmological hydrodynamical zoom-in simulation of a $\sim 10^{13}\,M_\odot$ galaxy group as we use to derive subhalo abundances in chapter 3 (Richings et al., 2021). However, in this chapter, we only need the macro structure of the main galaxy and thus we only select particles belonging to the main halo identified by the SUBFIND algorithm (Springel et al., 2001) with particles belonging to subhaloes excluded. The simulated galaxy is selected from the EAGLE 100 Mpc box-size simulation (Schaye et al., 2015) and was first identified by Despali and Vegetti (2017) as having similar properties to lenses from the Sloan Lens ACS (SLACS) survey (Bolton et al., 2006). The friends-of-friends (FOF) ID of the halo is 129. To resolve dark matter haloes with masses down to $\sim 10^6\,M_\odot$, this zoom-in simulation applies a novel technique whereby there are many more dark matter particles than gas particles. Unlike the common construction of initial conditions in hydrodynamic simulations, where each dark matter particle in a dark-matter-only simulation is split into a pair of dark matter and gas particles, the simulation we use initializes 7 dark matter particles per gas particle, resulting in dark matter and gas particle mass of $8.3\times10^4\,M_\odot$ and $10.7\times10^4\,M_\odot$, respectively. At $z = 0$, the dark matter halo of the zoom-in simulation's galaxy group has a mass of $M_{200} = 10^{13.14}\ M_\odot$ and size of $r_{200} = 506$ kpc. The Plummer-equivalent gravitational softening length is 0.05 kpc.

In Fig. 4.1, we show the convergence profile of different components of the simulated galaxy assuming the lens and source galaxy to be at $z = 0.2$ and 2.5, respectively.

Inside the central $\sim 0.7$ arcsec, the baryonic mass is larger than the dark matter mass, and the central density of stellar mass is around 4 times higher than that of the dark matter. A constant-density core with a size of $\sim 0.1$ arcsec exists in the central region, which is a result of the finite resolution of the simulations. This phenomenon has been seen in several other studies that simulate strong lens images from simulation data (Mukherjee et al., 2018, Enzi et al., 2020, Ding et al., 2021), and it can produce a dim central image in simulated strong lensing images that is rarely seen in real observations (Winn et al., 2004, Quinn et al., 2016). The core feature introduces additional complexity beyond realistic massive ellipticals and thus might lead to an overestimation on the baryonic effects in our tests. Fortunately, for the lens configurations considered in this work, the central image is sufficiently dim and small that one can mask it out without it impacting the lens modelling and subhalo inference, an approach also followed by Enzi et al. (2020). To do this, we artificially increase the assumed error on the flux in the region containing the central image to such high values that they are effectively removed from the goodness-of-fit measurement.*

### 4.2.2 Simulating strong lensing images

#### 4.2.2.1 Mock lenses

To simulate images that are strongly lensed by the particle distribution from a hydrodynamical simulation one needs a method which can determine the corresponding deflection angle map. There are two common ways of approaching this: (i) derive the projected density distribution of the particle data and solve for its potential via a Fast Fourier Transform (FFT) or; (ii) assume analytic profiles representing each particle enabling deflection angles to be easily computed, such that

*We previously attempted to remove the central image by applying a mask that removed the data in the central region altogether. However, we found that this introduced systematics due to edge effects associated with the source-plane pixelisation. Pixels at the edge of the mask (which have non-negligible flux due to the central image) were not appropriately regularized because their neighbours were not traced to the source plane (see Nightingale et al., 2018).

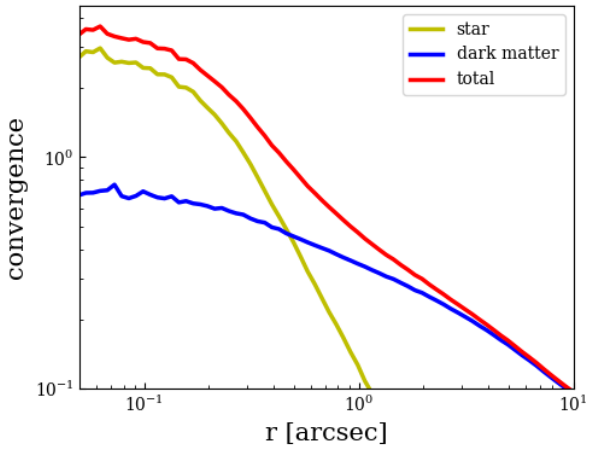


Figure 4.1: Convergence of different components of the simulated galaxy. Yellow, blue and red represents the stars, dark matter and total matter respectively, assuming the lens at z = 0.2 and source at z = 2.5. At the redshit of the lens $z = 0.2$, 1 arcsec corresponds to 3.3 kpc in angular size.

the overall deflection field is the sum over all particles. For the latter method, the computational cost can be greatly reduced by using a $k$-d tree algorithm (Bentley, 1975), making it faster than the FFT method at comparable resolution (Metcalf and Petkova, 2014, Petkova et al., 2014). However, neither method offers a well posed way of quantifying particle noise in the deflection angles, which can closely resemble the deflection angles of a dark matter subhalo in a strong lens (Xu et al., 2009). Besides the particle noise, these above methods also face the boundary truncation effect, which is that when truncating the particle data in an improper way (e.g. a square boundary applied to an elliptically shaped galaxy), an artificial shear component is introduced (Van de Vyvere et al., 2020). The shear magnitude depends on the galaxy's profile, the truncation area size and the truncation scheme used, and an improper truncation on the particle mass data can induce several percent bias to $H_0$ inference (Van de Vyvere et al., 2020, Ding et al., 2021).

To avoid particle noise and the boundary truncation effect, we therefore instead fit analytic profiles to the simulated galaxy's particle data and use these profiles to compute our lens galaxy's deflection angle field. We approximate the projected mass distribution of the simulated galaxy using the multiple Gaussian expansion

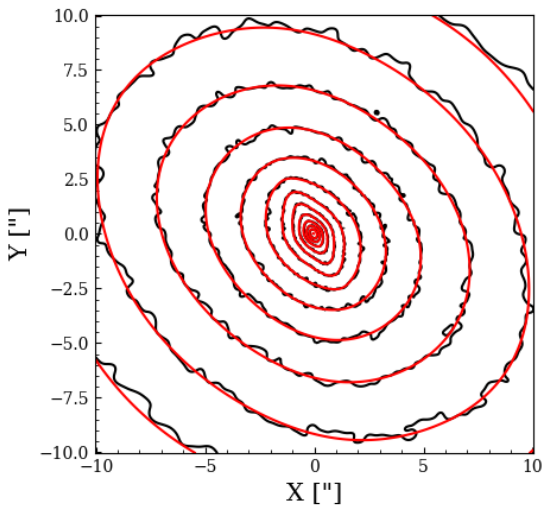


Figure 4.2: Iso-density contours of the projected stellar mass distribution of our simulated galaxy. The contours measured directly from the particle data using GLAMER (Metcalf and Petkova, 2014, Petkova et al., 2014) are shown in black, while those for the best-fit MGE are in red. The contours are evenly log-spaced in projected density. From inside to outside, each contour decreases by 0.4 order. Note that only very inner part (within 5 arcsec) of this image is observable and the reason we plot it on a much larger region is to show that the MGEs represent the lens' stellar mass well to a very large range. For clarity, later plots are all zoomed in to the region around the Einstein radius.

(MGE) method, which is widely used for modelling galaxy surface brightness profiles in studies of galaxy stellar dynamics (e.g. Cappellari, 2008, Li et al., 2016a, 2019, He et al., 2020). Li et al. (2016a) applied the expansion method to both galaxies and dark matter haloes in Illustris simulation, showing that it has flexibility to capture irregular and asymmetric features in a galaxy's light or mass distribution. The deflection angles (and other lensing quantities) of an elliptical Gaussian profile can be easily computed (Shajib, 2019), making lens simulations convenient and fast.

We compute the deflection angles of the simulated galaxy separately for its stellar and dark matter components, and then add them together to get the total deflection angles. The gas component is omitted because its contribution to the total mass in the galaxy's central region is negligible. We add subhaloes to the deflection angle map via an analytic mass profile.

We set the lens galaxy to be at redshift $z = 0.2$, and the source galaxy at $z = 2.5$. We first use GLAMER (Metcalf and Petkova, 2014, Petkova et al., 2014) to generate convergence maps, where each particle is represented by a smoothed b-spline in 3D. For each star particle the smoothing length is the distance to its 8th nearest (stellar) neighbour and for each dark matter particles it is the distance to its 64th nearest (dark matter) neighbour. We then use the MGE code of Cappellari (2002) to decompose the convergence maps into multiple Gaussian profiles, where the Gaussian components share the same centre but are free to have different amplitudes, sizes, position angles and axis ratios. As an example, Fig. 4.2 shows contours tracing the particle data input (dark lines) and MGE best-fit (red lines) of the simulation's projected stellar mass distribution. The MGE-fitting code decomposes the stellar component into 13 individual Gaussian profiles and Fig. 4.2 shows asymmetric features such as the twist in ellipticity are well captured by the MGEs. The relative errors between the input profile and best-fit MGEs are smaller than $\sim 5\%$. We apply the same routine to the simulation's dark matter particles and then add the best-fit Gaussian profiles together to represent the simulated galaxy's total projected mass distribution.

In the top-left panel of Fig. 4.3, we show the convergence (i.e. the projected density divided by the critical surface density for lensing) of the MGE representation of the simulated galaxy, where a pointy "American football-like" shape can be seen. To investigate how lens model fits change depending on the shape of the convergence, we rotate the same galaxy to view it along a different line of sight, intentionally choosing a viewing angle that produces a rounder convergence map, which is shown on the bottom left panel of Fig. 4.3. Following equation (43) of Shajib (2019), we compute MGE deflection angles for both projections, which are then used to simulate strong lensing images. For an accurate computation of each image pixel's flux, we treat every pixel with a $4 \times 4$ subgrid so that for each image pixel 16 light rays are traced to the source plane, with the pixel flux set to their mean value.

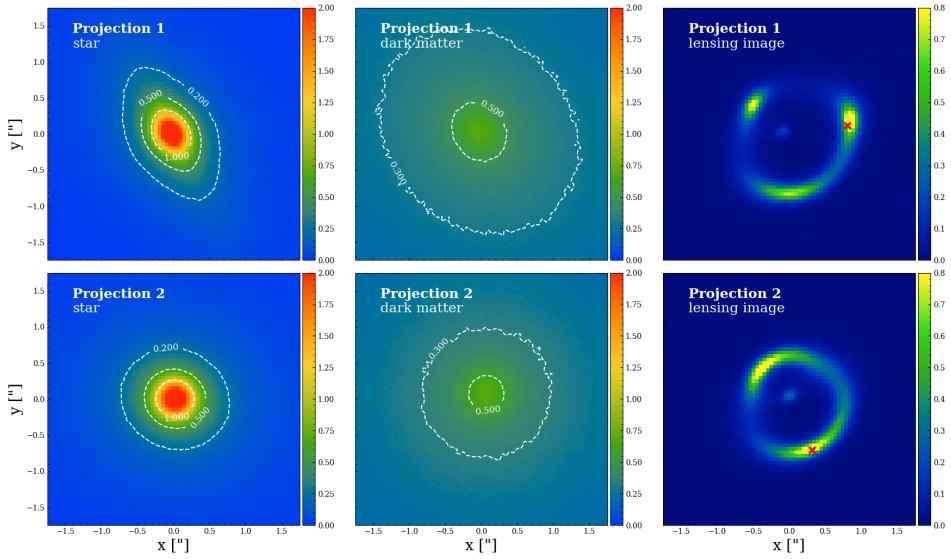


Figure 4.3: Input stellar (left column) and dark matter (middle column) convergence maps of our simulated galaxy along two different lines of sight (the two rows). The corresponding strong lensing images are shown in the right column. The top row is for the line of sight that produces pointy shaped iso-convergence contours, and the bottom row shows the projection with a rounder convergence field. The red crosses on the mock images mark the positions where we will later place subhaloes.

#### 4.2.2.2 Mock sources

Similarly, we simulate source galaxies using the cored Sérsic profile as Eq. 2.3 with $n = 2$. The choice of our mock source, a single elliptical cored Sérsic profile is simple compared to observed lenses where source galaxies are more complex and show features such as multiple star forming clumps, spiral structures and extremely compact centres. Our choice here is to make it straight forward to test the effects of using different lens mass models. Our lens modelling procedure uses pixelised source reconstructions which are able to fit the more complex sources seen in real data (Nightingale et al., 2019).

#### 4.2.2.3 Subhaloes

Some of our mock lensed images include a dark matter subhalo in the lens galaxy near one of the arcs. We represent subhaloes using the spherical NFW profile

(Eq. 1.5) assuming the mass-concentration relation of Ludlow et al. (2016). Following equation (A.18) of Baltz et al. (2009), we analytically compute its deflection angles and add it to that inferred via the MGE fit to the stellar and dark components. Mock lenses are generated with an input subhalo of two different masses, $M_{200} = 5 \times 10^8$ $M_\odot$ or $M_{200} = 5 \times 10^9$ $M_\odot$.

#### 4.2.2.4 Data Quality

We simulate mock images similar to observations of the HST/ACS Wide Field Camera, with a pixel size of 0.05″and a Gaussian PSF with a standard deviation of 0.05″*.

We set the normalisation of the source's surface brightness to give a S/N of $\sim 80$ in the brightest pixel of the lensed source's image, whilst adjusting the background noise level to closely match that expected from a few HST orbits. For our mocks, the background sky noise is 0.1 $e^-\text{pixel}^{-1}\text{s}^{-1}$. This S/N represents observations that are around double the highest S/N sources observed currently with Hubble, for example the SLACS sample. Using such high S/N data is a choice we made to ensure our tests of deficiencies in the lens mass model are easier to distinguish from noise in the mock data. The right column of Fig. 4.3 shows the two mock images, where a source galaxy is lensed by the two different line-of-sight projections (the corresponding projected densities are shown on the left). For mock datasets which include a subhalo, the positions marked by red crosses showing the locations of the subhalo that we add. In Table 4.1, we summarize the relevant parameters used to simulate these images.

*The actual PSF $\sigma$ for HST/ACS is ∼0.034″and the pixel size is 0.04″, so our tests are slightly worse than real HST observations in terms of resolution. However, in terms of the PSF modelling, we assume we have perfect knowledge of the PSF, which goes in the other direction of being optimistic.

| | Projection 1 | Projection 2 |
|---|---|---|
| **Input Lenses** | | |
| Stellar MGE number | 13 | 11 |
| Dark MGE number | 5 | 5 |
| redshift | 0.2 | |
| **Input Sources** | **Cored Sérsic** | |
| centre(x, y) [(″, ″)] | (0.08, -0.03) | |
| axis ratio | 0.55 | |
| position angle [°] | 30 | |
| $I^{'}$ [$e^{-}$ $pix^{-1}$ $s^{-1}$] | 2.0 | |
| $r_e$ [″] | 0.11 | |
| $n$ | 2.0 | |
| $r_c$ [″] | 0.01 | |
| redshift | 2.5 | |
| **Input Subhaloes (if added)** | **Spherical NFW profile** | |
| centre(x, y) [(″, ″)] | (0.81, 0.12) | (0.32, -0.71) |
| $M_{200}$ [$M_\odot$] | $5 \times 10^8$ or $5 \times 10^9$ | |
| mass-concentration relation | Ludlow et al. (2016) | |
| redshift | 0.2 | |
| **Image Settings** | | |
| pixel size [″] | 0.05 | |
| PSF $\sigma$ [″] | 0.05 | |
| background noise level [$e^{-}$ $pix^{-1}$ $s^{-1}$] | 0.1 | |
| exposure time [s] | 8000 | |
| maximum pixel S/N | $\sim$ 80 | |

Table 4.1: Parameters used to simulate the mock lensing images.

## 4.3 Method

### 4.3.1 Mass Models

#### 4.3.1.1 Broken Power Law

The simulated lens galaxy has an artificial $\sim 0.1\,\mathrm{kpc}$ constant density core, which forms a spurious central, demagnified image. We mask this central image by manually decreasing the contribution of central image pixels to the likelihood calculation, but must also ensure our mass model parameterization is able to represent the cored density, to avoid biasing our reconstruction of the lensed source's arcs (Enzi et al., 2020). We therefore assume the elliptical broken power law (eBPL) profile (O'Riordan et al., 2019, 2020, 2021) with convergence

$$\kappa(r) = \begin{cases} \kappa_{\mathrm{b}} \left(r_{\mathrm{b}}/r\right)^{t_1}, & r \leq r_{\mathrm{b}} \\ \kappa_{\mathrm{b}} \left(r_{\mathrm{b}}/r\right)^{t_2}, & r > r_{\mathrm{b}} \end{cases} , \tag{4.1}$$

where $r_{\mathrm{b}}$ is the break radius, $\kappa_{\mathrm{b}}$ is the convergence at the break radius, $t_1$ is the inner slope and $t_2$ is the outside slope. When $r_{\mathrm{b}} = 0$, the eBPL reduces to the standard power law profile with 3D density $\rho(r) \propto r^{-\gamma}$, as used in many lens studies. The ellipticity is introduced by setting $r = \sqrt{(x/q)^2 + y^2}$, where $q$ is the axis ratio. In practice, we parameterize a model's axis ratio and position angle, $\theta$, in terms of two components of ellipticity:

$$e_1 = \frac{1-q}{1+q} \sin 2\theta \ , \qquad\qquad e_2 = \frac{1-q}{1+q} \cos 2\theta \ . \tag{4.2}$$

With two additional parameters describing the profile's centre, the eBPL model has 8 free parameters. Degeneracies between certain parameters in the eBPL profile, for example the two different slopes, make it challenging to fit efficiently and avoid inferring local maxima. We therefore assume priors that lessen these degeneracies and simplify parameter space, where we constrain $r_{\mathrm{b}} \leq 0.4''$, $t_1 \leq 0.5$ and $t_2 > 0.5$. For some cases, we further limit the Einstein radius to be larger than $0.5''$. All eBPL

models are fitted with an additional external shear in the lens model, which provides further flexibility in stretching and squeezing of the mass profile that can capture some asymmetric features in the lens's convergence (Cao et al., 2021). Similar to the ellipticity parameterization, the external shear is also parameterized with two components $\gamma_{1\text{ext}}$ and $\gamma_{2\text{ext}}$, where the shear's magnitude, $\gamma_{\text{ext}}$, and position angle, $\theta_{\text{ext}}$, can be recovered as

$$\gamma_{\text{ext}} = \sqrt{\gamma_{1\text{ext}}^2 + \gamma_{2\text{ext}}^2} \, , \qquad \tan 2\theta_{\text{ext}} = \frac{\gamma_{2\text{ext}}}{\gamma_{1\text{ext}}} \, . \tag{4.3}$$

For modelling of a subhalo, we take the same NFW form we use to simulate the image.

#### 4.3.1.2 Source reconstruction

The final lens models of our analysis – from which all results in the main content of this chapter are taken – reconstructs the source galaxy using a pixelisation that adapts to the source's surface brightness distribution (see Nightingale et al., 2018, for a discussion of systematics this approach removes compared to other pixelisations). However, before using this pixelised source, a number of initial fits are performed which estimate the parameters of the lens mass model efficiently (for details see the next subsection). These fits assume either a parametric source which is modelled using the Sérsic profile ($r_{\text{c}} = 0$ in Eq. 2.3) or a pixelised source where the density of pixels adapts to the magnification, leading to smaller pixels in more magnified areas of the source plane. In appendix B we also show that we reproduce our main conclusions assuming a parametric cored-Sérsic source model.

### 4.3.2 Fitting procedure

We use a technique built in PyAutoLens called "non-linear search chaining" to compose pipelines which break the lens modelling procedure into a series of simpler model fits. This allows us to begin modelling our data with a simple lens

model (e.g. an isothermal mass profile and a Sérsic source) and via a sequence of non-linear searches gradually increase the model complexity, so as to eventually fit the desired more complex lens model (in this work, mass models which include a dark matter subhalo and with a source reconstructed on the brightness-based pixelisation). Non-linear search chaining is implemented via the probabilistic programming language PyAutoFit (Nightingale et al., 2021a). We use the nested sampling algorithm Dynesty to perform all model fits.

We employ the Source, Light and Mass (SLaM) pipelines that are distributed with PyAutoLens *. The SLaM pipelines were used in the work of Cao et al. (2021) and Etherington et al. (2022) and our analysis closely follows theirs, albeit we end with an additional pipeline that determines whether including a subhalo in the lens model increases the Bayesian evidence relative to the model without a subhalo. Like in Cao et al. (2021), we do not need to model the lens light and therefore employ a model fitting procedure consisting of four distinct pipelines which each focuses on fitting a specific aspect of the model. These pipelines are, in order: (i) the parametric source pipeline; (ii) the pixelised source pipeline; (iii) the lens mass pipeline and; (iv) the subhalo pipeline. Each pipeline consists of one or more non-linear searches that fit a unique lens model parameterization, which Fig. 4.4 shows a flow chart of, which we will now explain in detail.

#### 4.3.2.1 Parametric source pipeline

The parametric source pipeline aims to initialize a robust model for the lens galaxy's mass by fitting a source galaxy that has a smooth analytic form. The primary reason for this pipeline is that a robust model for the lens galaxy's mass is necessary to avoid pixelised source reconstructions inferring the unphysical solutions described by Maresca et al. (2021), where the reconstruction inferred is a demagnified version of the lens data. This pipeline assumes an SIE mass model (Eq. 2.1) with an external shear and a Sérsic profile for the source surface brightness.

*https://github.com/Jammy2211/autolens_workspace

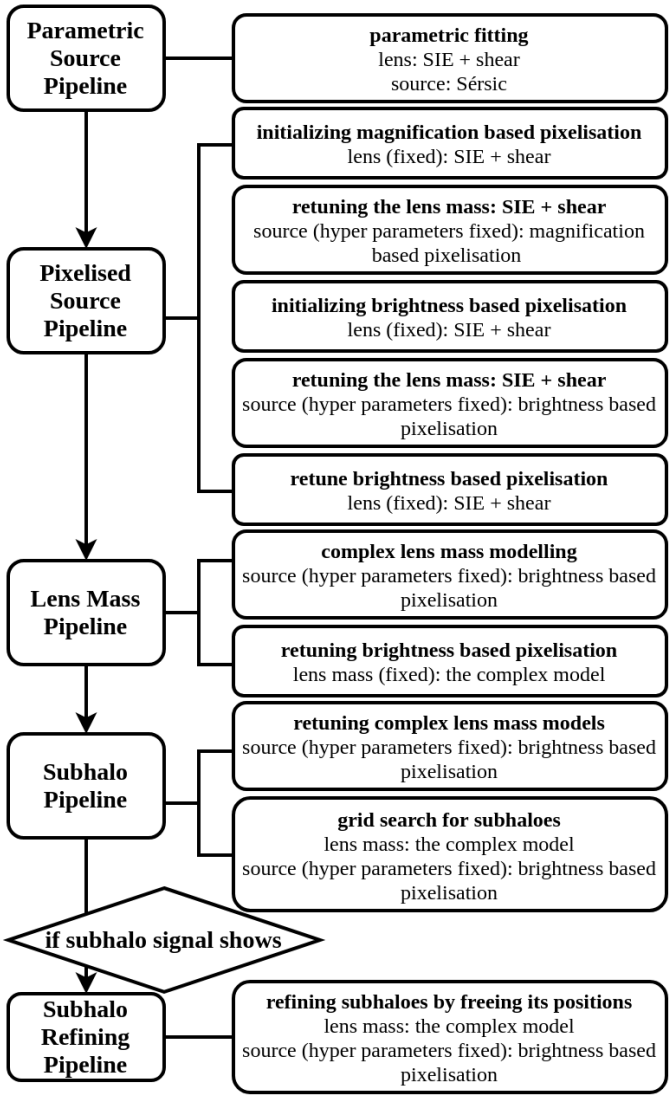


Figure 4.4: The fitting procedure we use to search for subhaloes.

#### 4.3.2.2 Pixelised source pipeline

The pixelised source pipeline is composed of four search phases. The first search fits for parameters describing the resolution of the magnification based pixelisation and the regularization coefficient of the constant regularization scheme, with the lens mass model fixed to the result of the parametric source pipeline. The second search re-fits the lens mass model using the pixelisation and regularization inferred previously. The third search fits for parameters that derive the surface brightness based pixelisation and the luminosity weighted regularization scheme, where the

lens mass model is fixed to the best-fit values inferred in the previous search. The fourth search again re-optimizes the lens mass model now using the brightness based pixelisation and regularization and we finally re-fit the pixelisation and regularization parameters again one last time, ensuring that the source reconstruction is tailored to the properties of the source it is fitting.

#### 4.3.2.3 Mass pipeline

This pipeline fits a more complex lens mass, either the eBPL model plus an external shear or the decomposed model that separately models the stellar and dark components plus an external shear. This pipeline consists of two searches. It first fits the new lens mass model with fixed source pixelisation parameters. The priors of the (broken) power law model's centres, elliptical components, Einstein radius are updated using information of the previous best-fit models. We set those priors to be Gaussian priors centering on corresponding best-fit values of previous models and their widths are set manually using values which balance reducing the size of parameter space to ensure an efficient fit whilst being broad enough not to remove physically plausible solutions. For other parameters (like the break radius, inner (outer) slopes, and external shear) we assume broad uniform priors that are not informed by the previous mass model fits. Having now fitted this more complex mass model, we again update the source pixelisation and regularization parameters using the best-fit lens mass model of the first step. This is the final fit which updates the pixelisation and regularization parameters, with all remaining fits focusing on the lens (and subhalo) mass models.

#### 4.3.2.4 Subhalo pipeline

This pipeline performs Bayesian model comparison to determine if a lens model with a subhalo is preferred over a lens model without a subhalo. The pipeline begins by fitting the same lens mass model (with fixed source pixelisation and

regularization parameters) inferred at the end of the mass pipeline, with all priors inherited from this fit. This provides us with an estimate of the Bayesian evidence of the lens model without a subhalo. We then fit lens models which include an NFW subhalo. For the subhalo's mass, we assume a uniform prior on $\log_{10}(m_{200}/\mathrm{M}_{\odot})$ between 6 and 11.

Due to the complexity of our parameter space (which consists of the mass models of both the main lens galaxy and a subhalo) we found it was common for the inferred posterior to correspond to a local likelihood maximum (as opposed to the global maximum). To mitigate this, we scan for subhaloes using a grid of non-linear searches, where each search confines the $(x, y)$ image-plane coordinates of the subhalo to a small 2D square segment of the image-plane. We perform 25 independent model fits, corresponding to a $5\times5$ grid, which divides the image region between $-1.0''$ and $1.0''$ into sub regions with sizes of $0.4'' \times 0.4''$. The parameters of the main lens are fit for simultaneously along with the subhalo parameters in each of these 25 fits.

To determine whether the lens model with a subhalo is favoured by the data over the model without a subhalo, we must choose a statistical quantity with which to compare them. Obvious choices are the Bayesian evidence or differences in maximum log likelihood values. Similar to chapter 3, we choose to use the maximum log likelihood to compare models which do and do not include a subhalo. However, the Bayesian evidence is as an output of `dynesty` and we have verified that our results are unchanged using this quantity. We denote the difference between the two maximum log likelihoods to be $\Delta L$, such that if $\Delta L$ in certain cells of the subhalo search are large it suggests the existence of a subhalo within one of those certain grids. Instead, if all log likelihood differences are very small, then it indicates no subhaloes of a sufficiently high mass to be detected are present in the image. For this paper, we take the threshold as follows: if $\Delta L \leq 5$, we call it a non-detection; if $5 < \Delta L \leq 10$, we call it a plausible detection; if $\Delta L > 10$, we call it a detection.

If the subhalo grid search has a plausible detection ($\Delta L > 5$) the subhalo pipeline

performs one more fit, which fits for both the main lens and subhalo parameters. The subhalo's $(x, y)$ position is no longer confined to a square segment of the grid search and we instead place a Gaussian prior on the $x$ and $y$ positions. The 2D Gaussian prior is centred at the maximum-likelihood subhalo position inferred previously using the grid search, with a relatively large standard deviation of $0.5''$. For the subhalo's mass, we retain a prior uniform in $\log_{10} M$ between $10^6$ $M_\odot$ and $10^{11}$ $M_\odot$.

## 4.4 Power Law Tests

We first use our simulated lenses to test the broken power law profile, which is commonly assumed in strong lensing studies to model the mass distribution of the lens galaxy (Vegetti et al., 2014, Collett and Auger, 2014, Dye et al., 2015, Ene et al., 2018). Our tests are divided into two parts: (i) how do power-law fits behave for the case where no subhalo is present in the mock data; (ii) can the power-law correctly recover the subhalo's properties when there is one present in the mock data. For convenience, we call the tests where no subhalo is added "smooth tests", and tests where there is a subhalo added "subhalo tests".

### 4.4.1 Smooth test results

In Fig. 4.5, we show the input and recovered images from the best-fit smooth model when fitted to simulated images that do not include a subhalo (this corresponds to the first model fit in the subhalo pipeline and will act as the model we compare to models including a subhalo in a moment). For visual clarity, we have removed the central image caused by the core of the simulated galaxy, however note that this region is included in the model-fit with high error values. For both projections, the reconstructed images in the middle panel are similar to the input images shown on the left. The normalized residuals (residuals divided by the noises) shown in the right panel confirm the good fit, showing no clear or obvious correlated residuals.

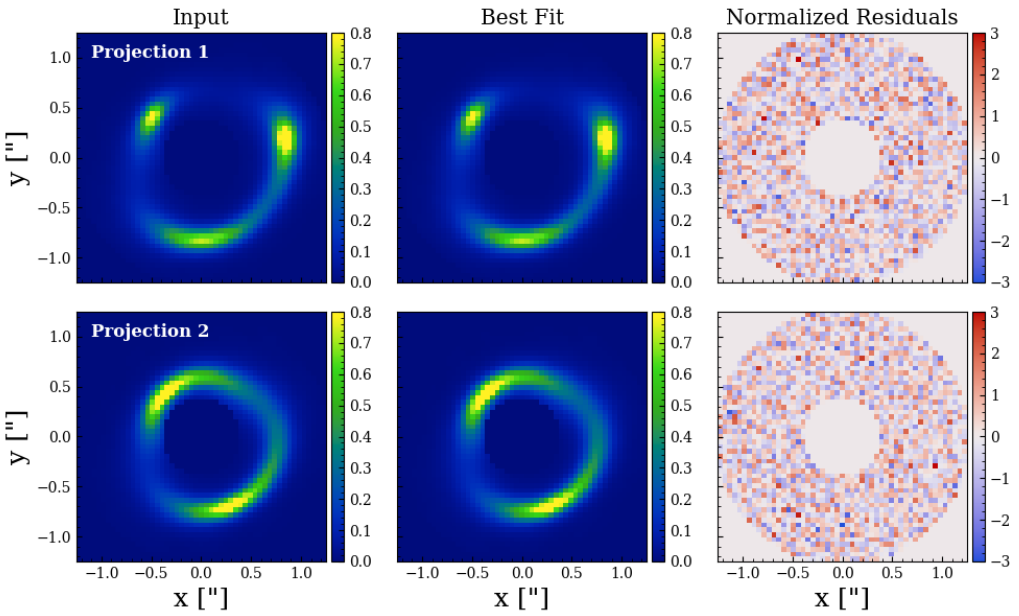


Figure 4.5: **Left column:** the mock lensing images. **Middle column:** the best recovered images using an eBPL to model the lens mass. **Right column:** the corresponding normalized residuals (residuals divided by the noises). The top row show the case of Projection 1 and the bottom row show the case of Projection 2. The color bar unit for the left two column images is $e^-$ $pix^{-1}$ $s^{-1}$. The units of the y and x axes are arcsec.

It is noted that the best-fit eBPL model's break radius for projection 1 and 2 are $\sim 0.2''$and $0.1''$respectively, which confirms that the core is able to affect the lensing even though the central image has been masked out. Using an eBPL model is therefore necessary to account for the core.

We now consider the results of the subhalo search. The left column of Fig. 4.6 shows the results of the subhalo phase, using the quantity $\Delta L$ (defined in Section 4.3.2.4) inferred in every cell of the subhalo-position grid. The upper and lower panels show the results of Projection 1 and 2 respectively. For Projection 1, where the input galaxy has a pointy shaped convergence, grids around the top-left luminous arc have $\Delta L$ over 10, and the highest $\Delta L$ is $\sim 21.4$ for the left most grid cell of the third row from bottom. For the grid cell with $\Delta L \sim 21.4$, a subhalo with $m_{200}$ of $10^{9.8^{+0.4}_{-0.5}}$ $M_\odot$ is inferred around that region. Given that the simulated lens galaxy we fitted here does not contain a subhalo, this signal is a false-positive. However,

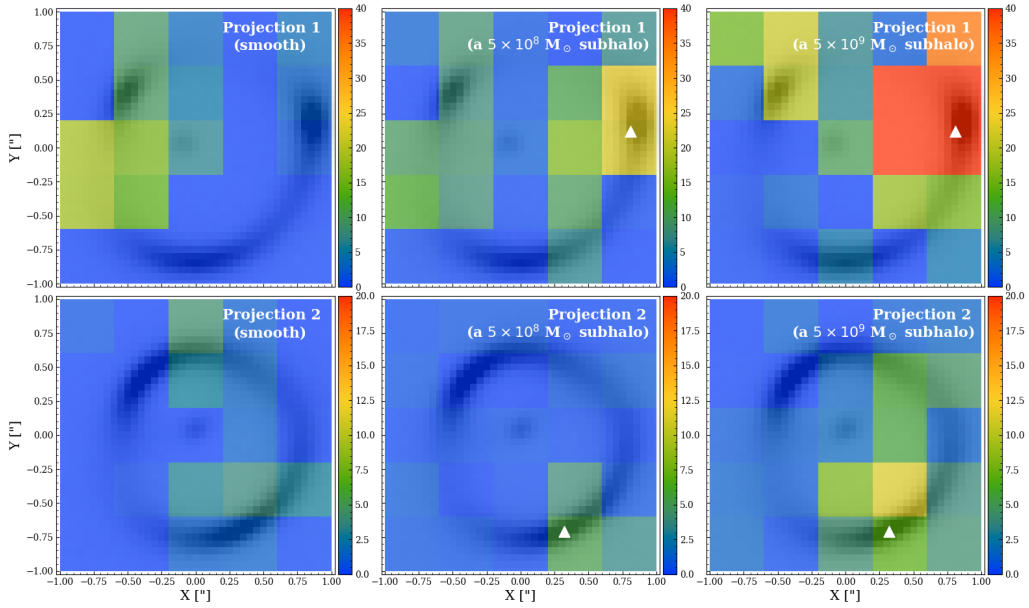


Figure 4.6: When modelling the lens mass distribution with an eBPL, substructures are (too) easily detected. Colours indicate the increase in maximum log likelihood, $\Delta L$, when a subhalo is included inside $0.4'' \times 0.4''$ squares during a fit to a lens that has: no subhaloes (left), a subhalo of mass $5 \times 10^8$ $M_\odot$ (middle), or a subhalo of mass $5 \times 10^9$ $M_\odot$ (right). Top and bottom rows show the results for Projection 1 and 2 (with different colour scales). White triangles mark the true locations of the subhaloes. Note the false-positive detections in the left panels; the best-fit subhalo masses in the other panels are also overestimated by a factor four to five.

for Projection 2 which has a rounder convergence, no grid has a $\Delta L > 5$. Assuming our criteria of requiring $\Delta L > 5$ the inclusion of an additional subhalo model using the eBPL is therefore correctly not favoured by the data and the eBPL gives the correct answer for this projection. However, it should be noted $\Delta L$ values of $\sim 3-4$ are still visible, indicating that at a very low level the subhalo is still improving the fit to the data.

Having shown the performance of using an eBPL to fit images without a subhalo present, we now test whether the same pipeline can correctly recover a subhalo's properties when a subhalo is included when generating the mock data. For both projections, we add an NFW-like subhalo of $M_{200} = 5 \times 10^8\,M_\odot$ or $5 \times 10^9\,M_\odot$ at the positions marked by the red crosses in Fig. 4.3.

Similar to our earlier analysis, we first check the $\Delta L$ maps. The middle column of

Fig. 4.6 shows $\Delta L$ maps for the cases where a $5 \times 10^8$ $M_\odot$ subhalo is added and the right panels show the results for a $5 \times 10^9$ $M_\odot$ subhalo. The upper and lower panels show the results of Projection 1 and 2 respectively. For Projection 1, grid cells near the subhalo's true input location (marked as white triangles in the image) show clear increases in $\Delta L$. For the $5 \times 10^8$ $M_\odot$ subhalo case, the maximum $\Delta L$ is $\sim$ 24.0 (for the rightmost cell on the fourth row from bottom) and for the $5 \times 10^9$ $M_\odot$ case, the maximum $\Delta L$ is $\sim$ 81.4 (also for the rightmost cell on the fourth row from bottom). Note that the colourbar saturates (for cells with $\Delta L > 40$) in the top-right panel.

Based on the detections shown in the $\Delta L$ maps, we continue the subhalo pipeline and fit a model where we no longer confine the subhalo within a particular square cell, and instead use a 2D Gaussian prior on the subhalo position, centered on the best-fit position from the "grid-search" phase, with a standard deviation of 0.5″. In Fig. 4.7, we show the posterior of the subhalo parameters for both the case with a $5 \times 10^8$ $M_\odot$ subhalo (red) and a $5 \times 10^9$ $M_\odot$ subhalo (blue). The true input values are marked by the dashed lines. As shown, for both cases, the subhalo's mass is significantly overestimated and the true input subhalo masses are excluded by 99% confidence regions. When the input subhalo has a mass of $5 \times 10^8$ $M_\odot$, the recovered subhalo mass is overestimated by $\sim$ 5 times with a value of $10^{9.4^{+0.4}_{-0.4}}$ $M_\odot$ inferred, whereas for the input subhalo with $5 \times 10^9$ $M_\odot$, the recovered mass is overestimated by around 4 times and has a value of $10^{10.3^{+0.2}_{-0.2}}$ $M_\odot$.

### 4.4.2 Subhalo test results

For Projection 2, with an input subhalo of $5 \times 10^8$ $M_\odot$, the maximum $\Delta L$ is only 3.4, therefore no subhalo is detected and we do not analyse the posterior on the subhalo properties. When the input subhalo mass is $5 \times 10^9$ $M_\odot$, the maximum $\Delta L$ is 9.7 providing us with a plausible detection. We take this plausible detection and refine the fit, with the resulting posterior for the subhalo parameters plotted in Fig. 4.8 . For Projection 2, the subhalo's mass is recovered to be $10^{10.1^{+0.5}_{-1.2}}$ $M_\odot$ where the

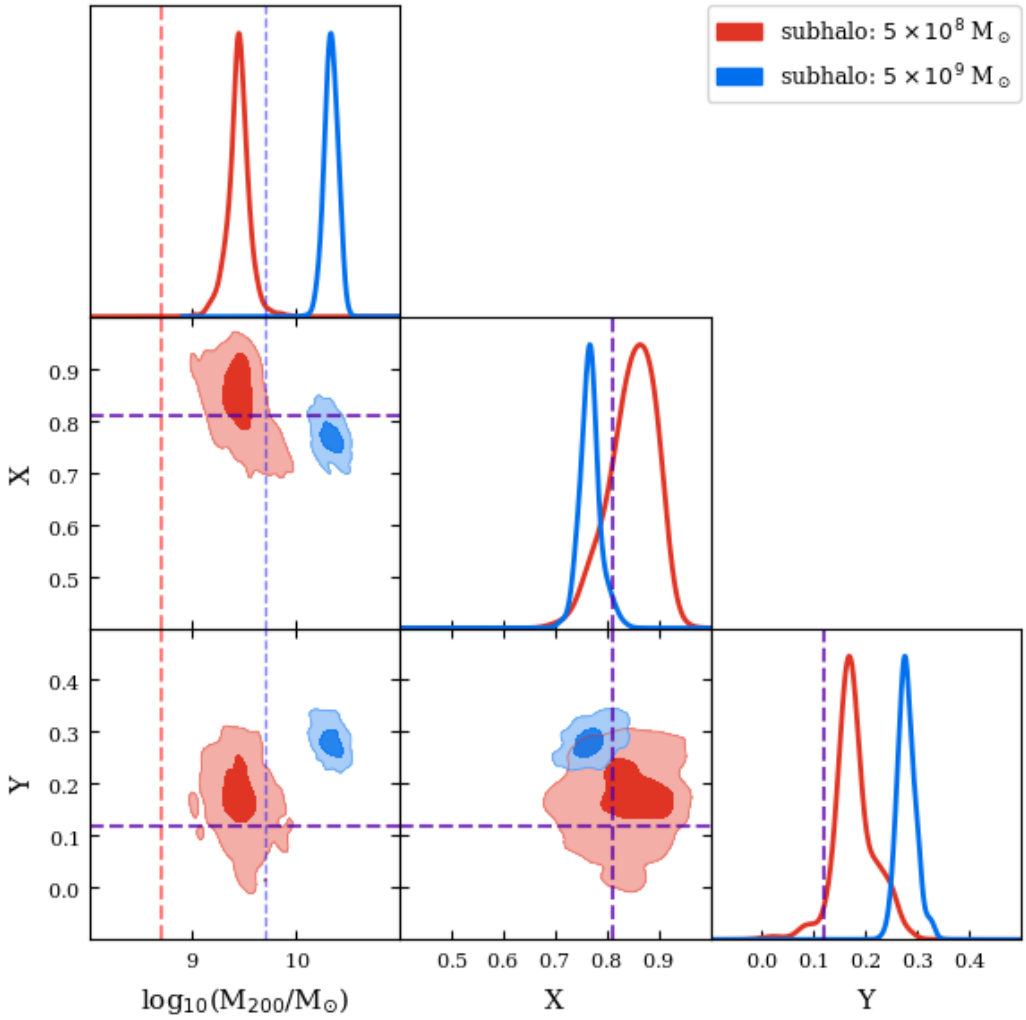


Figure 4.7: Posterior probability distribution of the subhalo model parameters, after the subhalo refining phase, when modelling the Projection 1 lens mass with an eBPL. Red and blue correspond to the cases of a $5 \times 10^8$ and $5 \times 10^9$ $M_\odot$ input subhalo respectively. The 2D contours cover the 68% and 99% credible regions. For 1D posteriors, the vertical dashed lines mark the true input values.

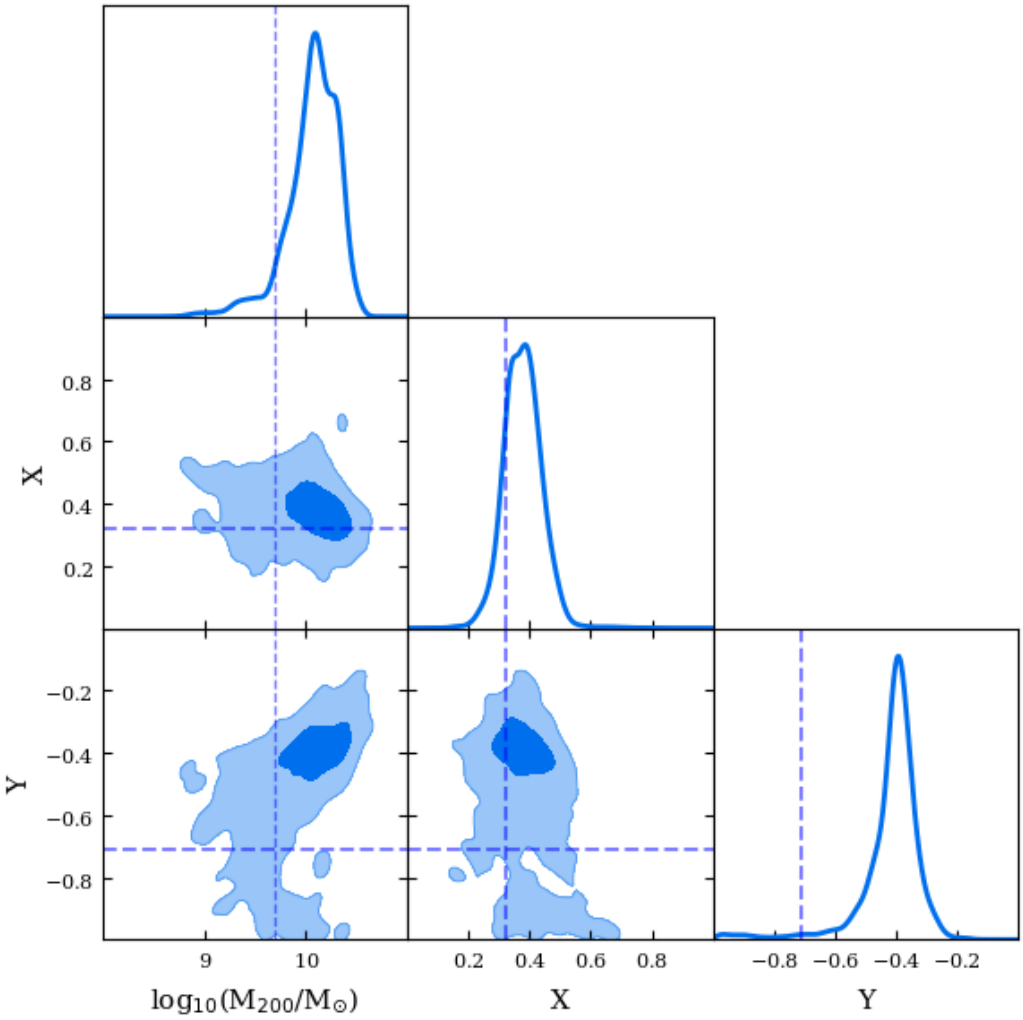


Figure 4.8: Subhalo parameters' posteriors of the subhalo refining phase, when modelling the Projection 2 lens mass with an eBPL. Only the case of a $5 \times 10^9$ $M_\odot$ input subhalo is shown (the case of a $5 \times 10^8$ $M_\odot$ subhalo does not lead to a clear detection). The 2D contours cover the 68% and 99% confidence regions. For 1D posteriors, the vertical dashed lines mark the true input values.

errors mark the 99% confidence regions. It is noted that in Fig. 4.8, although the subhalo's true parameters are recovered within 99% confidence regions (the light blue regions), the best-fit $M_{200}$ and y coordinate are clearly offset from the true input and in a case of smaller errors (higher S/N images), the true inputs might be ruled out.

### 4.4.3 Parametric Source

To verify that our conclusions are not a result of a systematic associated with our pixelised source model, in Appendix B we re-perform all of the above fits assuming a cored Sérsic profile for the source. For Projection 1 we see nearly identical behaviour in terms of false positives and the subhalo inference, however the $\Delta L$ values are much larger; of order $\sim 250$ compared to the values of $\sim 25$ seen for the pixelised source. This is expected, as the greater flexibility of the pixelised source reduces our sensitivity to a subhalo and therefore also false positives (Gilman et al., 2020c). For Projection 2, fits to the smooth data now infer a false positive with $\Delta L = 18.1$. This does not contradict the results using a pixelised source above, instead the values of $\Delta L =\sim 3-4$ shown in Fig. 4.6 have simply been boosted above our threshold value of $\Delta L = 5$ because fitting a cored Sérsic increases our sensitivity to subhaloes (and false positives). Thus, the eBPL does still produce false positive detections when it fits Projection 2, however to see these using a pixelised source one would likely require much higher S/N data.

### 4.4.4 Summary

For Projection 1, we saw false positive detections and an inability to recover an input subhalo's mass correctly. In contrast, for Projection 2, we did not infer a false positive detection (when assuming a pixelised source) and the subhalo's true mass is covered by the posterior. Taking into account the different convergence shapes of the two projections (see figure 4.3), we speculate the inaccurate inferences on

subhaloes for Projection 1 are caused by the clear mismatch in the shape of the eBPL and the more elliptical input profile. We also speculate the better performance seen for Projection 2 is because its rounder convergence is easier for the eBPL to model. However, due to the limited number of projections available, we cannot generalize these conclusions any further. We only saw the eBPL produced false positives in Projection 1 and there is a possibility that it is a different property of the lens driving this result. When analysing real lens systems we will look to see whether departures from ellipticity in the lens galaxy's light (Nightingale et al. 2022, in prep.) are correlated with subhalo detections, possibility indicating a false positive signal.

## 4.5 A Decomposed Model

Motivated by the inability of the eBPL to provide a robust subhalo inference, we now consider the decomposed model, which models a galaxy's stellar and dark matter mass separately. This includes sufficient freedom to capture complex features such as a pointy convergence profile, or other departures from elliptical symmetry.

### 4.5.1 Model introduction

In most strong lens images, we observe not only the lensed source's light, but also the light emitted from the lens galaxy, which should approximately trace its stellar mass distribution. For example, through inspection of the lens galaxy's light profile, we can estimate the position angle and axis ratio of the lens's stellar mass profile. More detailed light profile fits can provide us with a more detailed model of the stellar mass distribution. We now explore the potential of utilizing this information and if it can allow us to correctly recover the subhalo information hidden in the source's lensed images. We fit the lens's mass using a decomposed model which treats the lens galaxy's stellar mass and its dark matter mass separately. This type of model has been fitted in many previous studies (Dye and Warren, 2005, Suyu

et al., 2014, Wong et al., 2017) and Nightingale et al. (2019) showed using HST imaging of three SLACS lenses that such models capture variations in ellipticity and position angle within a galaxy that are indicative of pointy mass distributions.

For the stellar mass, we assume it exactly traces the stellar light, which allows us to directly transform between the two by multiplying by a constant mass-to-light ratio (M/L) parameter, which can be described as

$$\kappa(r) = \Psi \cdot I(r) \ , \tag{4.4}$$

where $I(r)$ corresponds to the light profile and $\Psi$ is its "mass-to-light ratio". For simplicity, we directly take the input stellar mass of the simulation's particle data as our lens light and therefore do not consider a more realistic galaxy light simulation process. In that sense, the "$I(r)$" is equivalent to the convergence profile and thus $\Psi$ becomes a dimensionless quantity and is set to be 1.0.

To utilize the "lens light" information, we model the "lens light" with three cored Sérsic profiles as described by Eq. 2.3. We opt for the cored Sérsic because of the simulated galaxy's core; for real lenses we anticipate that the regular non-cored Sérsic profile will suffice. We impose that the 3 cored Sérsic profiles share the same centre, but allow for them to have different position angles and axis ratios. We use three profiles because fits using two profiles do not fully capture the features of the "lens light" (e.g. clear spatially-correlated normalised residuals are seen when the best-fit two cored Sérsic model is subtracted from the true stellar mass distribution). In Fig. 4.9, we show the input lens light (left column), best-fit 3 cored Sérsic profiles (middle column) and corresponding normalised residuals (right column). For both projections (upper row corresponds to the Projection 1 and the lower one is for the Projection 2) the light is well fit by three cored Sérsics. Later, in our lens mass modelling, we fix the stellar mass distribution to be exactly the same as the best-fit three cored Sérsic profiles obtained from fitting the lens light, except for a free $\Psi$ which changes the overall normalisation of the projected stellar mass distribution.

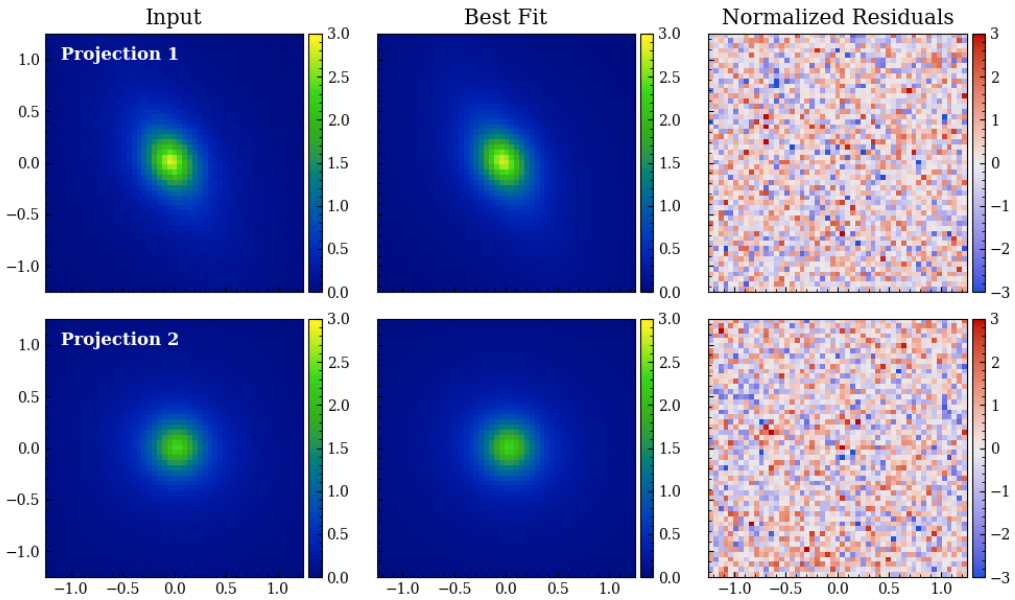


Figure 4.9: **Left column:** the mock lens light images. **Middle column:** the best recovered images using three cored Sérsics to model the lens light. **Right column:** the corresponding normalized residuals. The top row show the case of Projection 1 and the bottom row show the case of Projection 2. The units of the y and x axes are arcsec.

In addition to the stellar mass, we include an elliptical NFW profile into the lens model (to account for the dark matter). This has six free parameters: a scale radius, $r_{\rm s}$, and scale convergence, $\kappa_{\rm NFW}$; two ellipticity components; and the 2D coordinates of the halo centre. As in the eBPL case, we include an external shear in the decomposed lens model.

Neither cored Sérsic nor elliptical NFW profiles have analytical formulae for their deflection angles. For fast computation we follow Shajib (2019) and use a sum of 2D Gaussian profiles to approximate the cored Sérsic and elliptical NFW profiles. The resulting deflection angles are simply a sum of the deflection angles of the individual Gaussian profiles, which can be efficiently computed using analytical formulae. To be specific, in our work, in most cases we approximate a cored Sérsic profile by 30 Gaussian profiles with their standard deviations uniformly distributed in the $\log_{10}$ space between $0.01r_{\rm e}$ and $50r_{\rm e}$, where $r_{\rm e}$ is the effective radius of the cored Sérsic. Similarly, for an elliptical NFW profile, we also approximate it

with 30 Gaussians and the standard deviations of those Gaussians are uniformly distributed in the $\log_{10}$ space between $0.0005r_{\rm s}$ and $30r_{\rm s}$. We noticed that one of the best-fit cored Sérsic components to the "lens light" of Projection 2 has a Sérsic index of 0.51 and for that profile the decomposition formula (Eq. 5 of Shajib (2019)) becomes numerically unstable. For that one particular case, we instead decompose the Sérsic profile into a sum of Gaussians using Cappellari (2002)'s method, which optimizes the standard deviations and amplitudes of those Gaussians at the same time. We have tested our choices of the parameters of the Gaussian decomposition method across a large variety of cored Sérsics and elliptical NFW profiles to ensure that errors of approximating the deflection angles are much smaller than the perturbation of a subhalo of interest. In Table 4.2, we summarize our lens model parameters.

The approach we follow cannot be straightforwardly translated to real data. For example, we have modelled the lens's light in the absence of the source light and ignored potential complications such as a radial gradient in the mass-to-light ratio. The goal of this work is not to present a method that can be directly transferred to the fitting of real data, but simply to show that when sufficient complexity is added to the lens mass model one's inference on subhalo properties improves. Nevertheless, Nightingale et al. (2019) have already shown how `PyAutoLens` can fit this type of model to real data and we expand on this further in section 4.6.3.

### 4.5.2 Results

We now present results using the decomposed model, following the same structure we used for the eBPL results, whereby we begin with the smooth test results (where no subhalo is present in the simulated data) followed by results where the simulated data includes a subhalo.

In Fig. 4.10, we compare the input and best-fit model images for smooth cases. As shown by the normalized residuals in the third column, no clear correlated residuals

| | **Projection 1** | **Projection 2** |
|---|---|---|
| **Stellar Mass** | **3 Core Sersics** | |
| centre(x, y) [(″, ″)] | (0.008, -0.036) | (0.003, 0.022) |
| $I^{'}$ | {0.44, 0.60, 0.31} | {0.32, 0.50, 1.06} |
| $r_{\rm e}$ [″] | {0.65, 0.02, 4.42} | {0.11, 0.18, 2.39} |
| $r_{\rm c}$ [″] | {0.14, 0.27, 0.25} | {0.35, 0.13, 0.02} |
| $n$ | {1.44, 4.36, 4.91} | {2.64, 0.51, 2.31} |
| position angle [°] | {-62, -59, -45} | {-27, 69, -73} |
| axis ratio | {0.33, 0.82, 0.82} | {0.90, 0.89, 0.90} |
| $\Psi$ | [0.8, 1.2] | |
| redshift | 0.2 | |
| MGE {n, rmin, rmax} | {30, $0.01r_{\rm e}$, $50r_{\rm e}$} | |
| **Dark Matter Mass** | **NFW** | |
| centre($x$, $y$) [(″, ″)] | [-0.1, 0.1] | |
| $\log_{10}\ \kappa_{\rm NFW}$ | [-2, 0.3] | |
| $r_{\rm s}$ [″] | [10, 50] | |
| $e_1$ | [-1.0, 1.0] | |
| $e_2$ | [-1.0, 1.0] | |
| redshift | 0.2 | |
| MGE {n, rmin, rmax} | {30, $0.0005r_{\rm s}$, $30r_{\rm s}$} | |
| **External Shear** | | |
| $\gamma_{\rm 1ext}$ | [-0.2, 0.2] | |
| $\gamma_{\rm 2ext}$ | [-0.2, 0.2] | |
| **Subhalo** | **Spherical NFW** | |
| centre($x$, $y$) [(″, ″)] | ([-1.0, 1.0], [-1.0, 1.0]) | |
| $\log_{10}\ M_{200}$ [$\rm M_\odot$] | [6, 11] | |
| mass-concentration relation | Ludlow et al. (2016) | |

Table 4.2: Parameters and priors for the decomposed model. Parameters with values shown in "()" or "{}" are fixed during the modelling. Parameters with values shown as "[a, b]" are fit for, with a uniform prior between a and b.

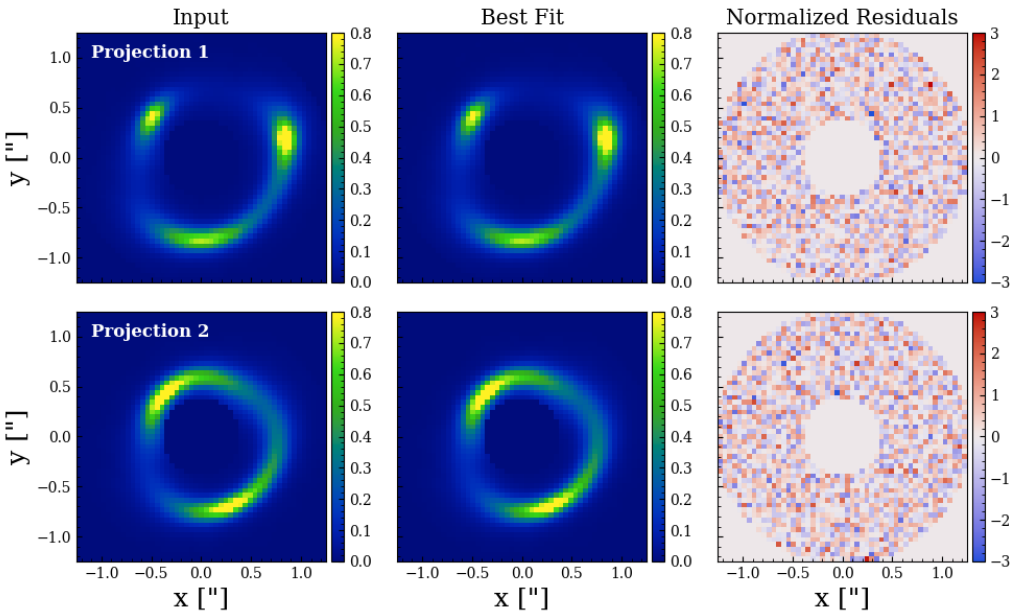


Figure 4.10: **Left column:** the mock lensing images. **Middle column:** the best recovered images using the decomposed model to fit the lens mass. **Right column:** the corresponding normalized residuals (residuals divided by the noise). The top row show the case of Projection 1 and the bottom row show the case of Projection 2. The colour bars for the left two columns are in units of $e^-$ $pix^{-1}$ $s^{-1}$.

exist, which indicates an overall good fit with the decomposed model. Comparing the results with the equivalent BPL results in Fig. 4.5, we see that the BPL results are indistinguishable from the decomposed model results in terms of the residuals, which confirms again that "subhalo-like" perturbations cannot be detected visually from the residual maps and we have to rely on careful statistical comparisons to make inferences about subhaloes.

In the left column of Fig. 4.11, we first show the maximum log likelihood difference maps when modelling the smooth image with the decomposed model described above. For both projections the decomposed model fits the image accurately with a maximum $\Delta L$ value below 5, correctly indicating that no subhalo exists in the lens galaxy. Unlike the eBPL, the decomposed model does not give false-positive signals in our "smooth tests".

In the middle and right columns of Fig. 4.11, we show the $\Delta L$ maps when a $5 \times 10^8$ $M_\odot$ or $5 \times 10^9$ $M_\odot$ subhalo is added to the lens galaxy at the positions

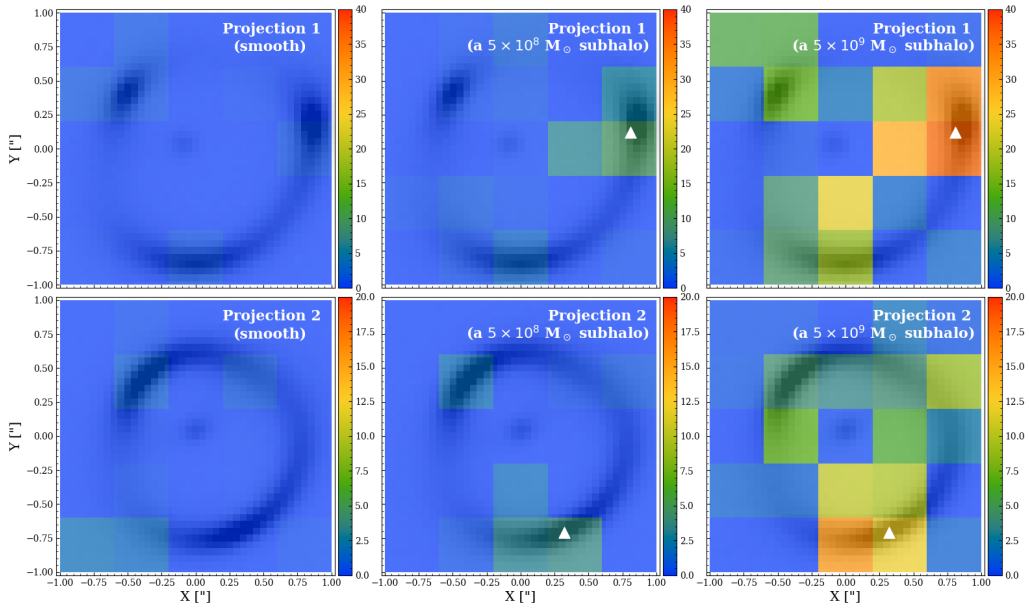


Figure 4.11: Modelling the lens with a decomposed stellar + dark matter model removes false-positive detections, and yields correct subhalo masses. Colours indicate the increase in maximum log likelihood, $\Delta L$, when a subhalo is included in the fit to a lens that: has no subhaloes (left), has a subhalo of mass $5 \times 10^8$ $M_\odot$ (middle), or has a subhalo of mass $5 \times 10^9$ $M_\odot$ (right). The position of the subhalo in the fit is free to vary within squares of side $0.4''$. The top and bottom rows show the results for Projection 1 and 2 (with different colour scales). White triangles mark the true locations of the subhaloes.

marked by the white triangles. For Projection 1 (upper panels), the regions where we detect the maximum $\Delta L$ is consistent with the position of each input subhalo. For an input subhalo of $5 \times 10^8$ $M_\odot$, the result shows a plausible detection where the maximum $\Delta L$ is 9.3, whereas for an input subhalo of mass $5 \times 10^9$ $M_\odot$, the detection is even clearer with a maximum $\Delta L$ of 36.0. Having successfully detected the subhalo in each case, we continue on to the subhalo refining fit, with Fig. 4.12 showing the inferred posteriors of the subhalo parameters. For both cases, the subhalo parameters are correctly recovered within 99% credible regions. For a $5 \times 10^8$ $M_\odot$ subhalo, the recovered value is $10^{8.9^{+0.8}_{-2.6}}$ $M_\odot$, and for a $5 \times 10^9$ M$\odot$ subhalo, the recovered value is $10^{9.5^{+0.5}_{-0.4}}$ $M_\odot$.

For Projection 2, we only get a detection when the true subhalo mass is $5 \times 10^9$ $M_\odot$, with a maximum $\Delta L$ of 15.8 (in the middle cell of the bottom row). With a $5 \times 10^8$ $M_\odot$ subhalo, all subhalo-position cells have $\Delta L < 5$, corresponding to no

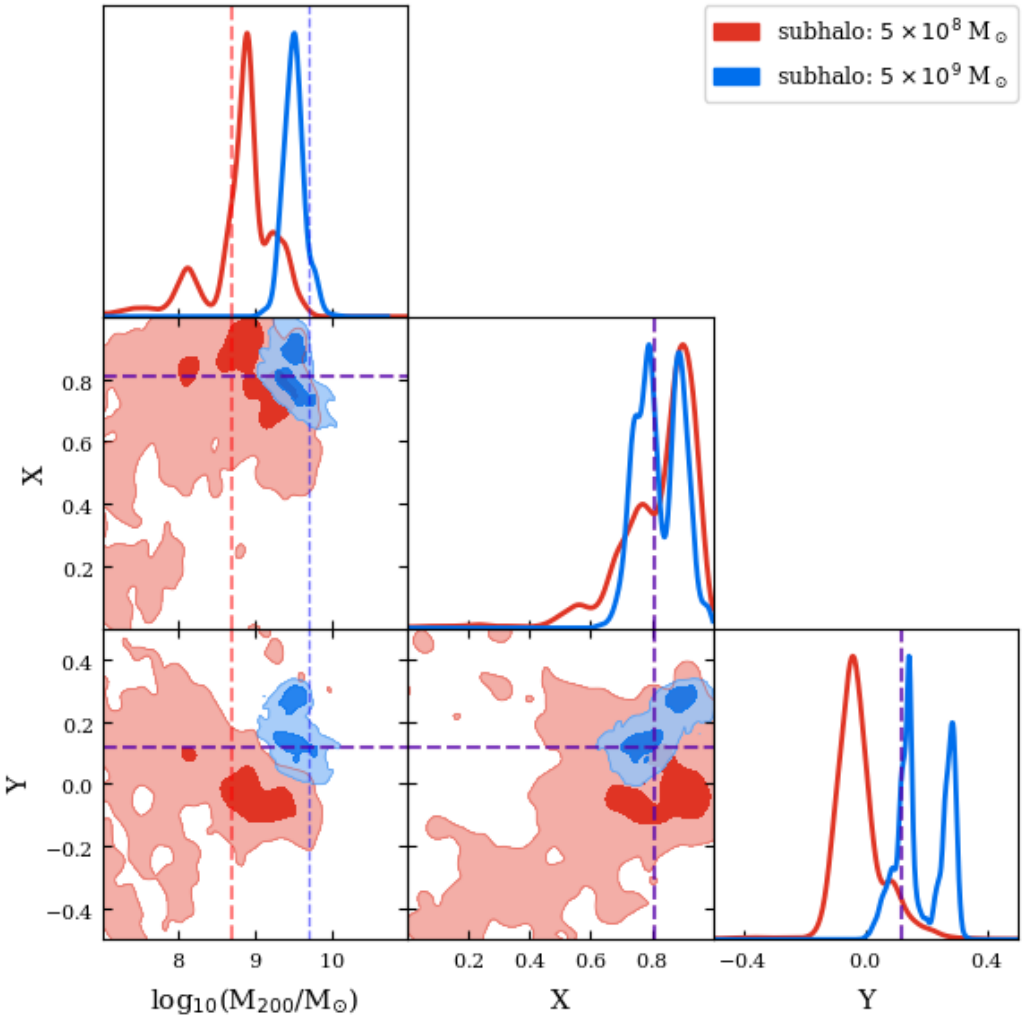


Figure 4.12: The posteriors on the subhalo parameters from the subhalo refining phase, fitting the decomposed model to mock data generated using Projection 1. Red and blue colours show the cases with an input subhalo mass of $5 \times 10^8$ and $5 \times 10^9$ $M_\odot$ respectively. The 2D contours cover the 68% and 99% confidence regions. For 1D posteriors, the vertical dashed lines mark the true input values.

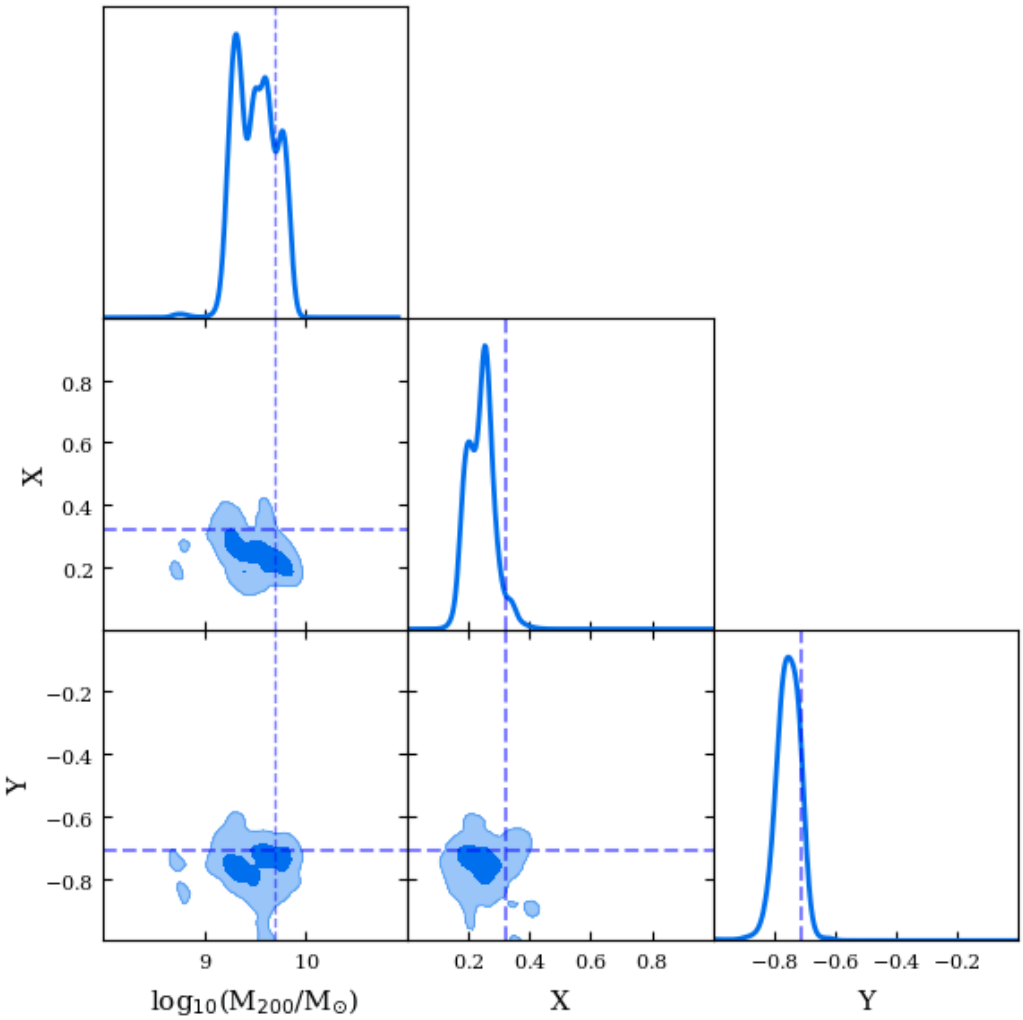


Figure 4.13: The same as Fig. 4.12, but for Projection 2. Only the case with a $5 \times 10^9$ $M_\odot$ subhalo is shown (a $5 \times 10^8$ $M_\odot$ subhalo is not clearly detected).

detection. In Fig. 4.13, we show the subhalo posteriors obtained from the subhalo refining phase for the $5 \times 10^9$ $M_\odot$ case. We recover the input subhalo mass, with a 99% credible region on $M_{200}$ of $10^{9.5^{+0.4}_{-0.7}}$ $M_\odot$. For the non-detection of the $5{\times}10^8$ $M_\odot$ subhalo, we do not believe this is a failure of the decomposed model, but instead a limitation of the data quality. In fact, if we check the inferred subhalo parameters for the sub grid cell which contains the input subhalo, the inferred subhalo's mass is $10^{8.7^{+0.7}_{-2.5}}$ $M_\odot$, which is still consistent with the true input mass. Thus, our inference on the subhalo's parameters is consistent with the truth, but we have insufficient S/N for the model to be favoured in terms of $\Delta L$.

We note that in Fig. 4.12 and 4.13, the posterior distributions are not smooth, having a "patchy" appearance in the 2D marginalised posteriors and "wiggles" in the 1D posteriors. These arise due to the pixelised source plane. The source plane pixelisation is created from a Voronoi tessellation of generating points, where the generating points are first placed in the image plane and then mapped into the source plane. Changes to the mass model change the mapping from image plane back to the source plane, such that the positions and shapes of the source-plane pixels varies as the lens mass model is changed. Certain locations for pixel boundaries may be more or less able to reproduce the observed data, leading to small changes to the mass model parameters capable of macroscopic changes to the likelihood. This phenomenon is more significant for more complex mass models which have more parameters and freedom to allocate those source pixel grids on the source plane. As a result, we get unsmooth posteriors for our decomposed model. The work of Etherington et al. (2022) discusses this further and presents a solution using a cap on the log likelihood of the model-fit.

### 4.5.3 Parametric Source

In Appendix B, we again verify that our conclusions hold when we assume a cored Sérsic profile for the source. For both projections, the decomposed model does not give a false positive; with the highest value of $\Delta L = 2.5$. Note that, for a cored Sérsic source, false positives were detected for both projections. Given that fits assuming a cored Sérsic for the source give a much higher sensitivity to subhaloes and false positives, this further strengthens our conclusion that adding the right type of complexity to the decomposed mass model removes the presence of false positives. As a result of this increased sensitivity, the $5 \times 10^8$ $M_\odot$ subhalo is also detected successfully in Projection 2, which is not the case for the pixelised source.

### 4.5.4 Offset True Positive Detections

In the right panels of Fig. 4.11 we note increases of $\Delta L =\sim 10 - 15$ away from the true location of the $M_{200} = 5 \times 10^9$ $M_\odot$ subhalo for both projections. These are solutions where an offset dark matter subhalo closely mimics the perturbing effects of the actual subhalo in the data. However, it is not a perfect representation of the actual subhalo, which is why fits at the true location infer higher overall log likelihood values. We do not consider these as false-positive detections because they are caused by the true presence of a detectable subhalo in the data. Should this behaviour be seen in real data we therefore should not discount the signal as a false positive. In fact, a candidate subhalo detection should be made and followed up with a second subhalo search which includes the first subhalo in the model, so as to validate the detection.

### 4.5.5 Summary

For both projections the decomposed model is a success. When we do not include a subhalo in the input lens galaxy, it returns no detections. When a subhalo is included in the mock data, it is able to correctly infer the existence of the subhalo through an increase in $\Delta L$ (at least for three out of the four cases we tried). Furthermore, it recovers the masses and positions of the subhaloes within 99% credible regions. By utilizing (idealized) "lens light" information, the decomposed model therefore successfully captures complexity in the mass profile (e.g. the non-elliptical shape) that the eBPL could not. The success of the decomposed model confirms that for subhalo detection, it is vital to model the lens galaxy's mass accurately.

## 4.6 Discussion

### 4.6.1 Implications for strong lensing subhalo detection

Our results confirm that if a dark matter subhalo is located near the emission of a strongly lensed source galaxy, its perturbing effects mean that its presence can be inferred. For gravitational imaging*, our work demonstrates this for first time by simulating the lens galaxy using a mass distribution derived from the particle data of a cosmological simulation, which therefore does not make idealized assumptions like a single axis of ellipticity. However, we also showed that assuming an overly simplistic mass model for the lens galaxy which lacks certain complexity compared to the true underlying mass distribution has two negative effects on the subhalo inference: (i) it may lead to false-positive detections of a dark matter subhalo even though a subhalo is not present in the data and; (ii) when a subhalo is truly present in the data it may lead to systematic biases on the inferred subhalo mass by a factor of $4-5$.

The notion that a mismatch in mass profile shape could lead to false-positive subhalo detections supports the analysis of Ritondale et al. (2019), who noted several false-positive signals found in real lensing systems in the BELLS-GALLERY sample. For example, they noted an increase in log Bayesian evidence of 72 in the lens SDSSJ0755+3445, but demonstrated – using a potential correction technique (Koopmans, 2005, Vegetti and Koopmans, 2009b) – that the mass model could be improved by small corrections over a large angular scale, as opposed to a localised correction reminiscent of a subhalo. This indicates that the subhalo-like signal is probably due to the mismatch in the macro models, as we saw in our tests. False positives are also partly the reason why Vegetti et al. (2014) and Vegetti et al. (2018) require Bayesian evidence increases of 50 and 100 to claim a dark matter detection; values below this threshold may be false positives (the authors also re-

*Similar tests on flux ratios have previously been explored by Hsueh et al. (2018).

quire validation via potential corrections). Whilst the false positives in this work did not create Bayesian evidence increases above 30, the overall size of the increase depends on the properties of the strong lens and sources simulated, the S/N of the data and model used to fit the data. In Appendix B false positives with evidence increases above 200 are inferred. Therefore, **our results do not indicate that previous detections of dark matter subhaloes in strong lenses are false positives**. Instead, they show the importance of techniques like the potential corrections and we provide insight on why these methods are able to distinguish a subhalo detection from missing complexity in the mass model.

### 4.6.2 Is our simulated lens galaxy realistic?

It is important to consider how realistic the simulated galaxy used in this work is. As discussed previously, the galaxy was selected to be similar to lens galaxies from the SLACS survey. It has a typical halo mass for a SLACS lens and its stellar mass and size (i.e. the half-light radius) follow recent observations of massive galaxies (Huang et al., 2018). The central galaxy has a complex shape, with isophotes that change shape when viewed from different directions, and where the shapes of the isophotes can vary with radius for a fixed viewing direction. We speculated that this departure from elliptical symmetry drove the false positives, because they are only seen for the projection where the mass distribution is highly elliptical. A varying isophotal shape with radius is commonly seen in observations of massive elliptical galaxies with comparable mass to SLACS strong lenses. For example, over 1/3 of galaxies with stellar masses above $10^{11.5}$ $M_{\odot}$ taken from the MASSIVE survey show isophotal position-angle rotations (Goullaud et al., 2018), known as "isophotal twists" (see Oh et al. (2017) for similar results in lower mass early-type galaxies). Similar features are also reported in three strong lenses by Nightingale et al. (2019). We therefore believe this aspect of our simulation is representative of real strong lenses and is a plausible cause of some of the false positives in the SLACS and BELLS-GALLERY lenses discussed previously.

The simulated galaxy also has a sub-kpc core, which generates a central image in our mock lens images. This phenomenon is seen in other works which simulate strong lenses from cosmological simulations (Mukherjee et al., 2018, Despali et al., 2020, Ding et al., 2021), with the core due to insufficient simulation resolution. Central images of this brightness are not seen in real observations of strong lenses, therefore such a large core is unrealistic. To ensure it does not impact our tests, the mass model parameterizations fitted in this work all included cores. We masked the central image so as to ensure the mass models did not utilize additional information that is not present in real images of strong lenses. Whilst this aspect of the simulated lens is therefore not realistic, the mass modeling performed in this work ensures we can generalize our conclusions to the analysis of real data.

### 4.6.3 Application to real data

Our next step is applying the decomposed model to real data. We expect that we will be able to fit mass models which omit parameters that account for a core, given that the core feature is a consequence of the inadequate simulation resolution. For the decomposed model, we will likely fit regular Sérsic functions instead of the cored Sérsics fitted in this work.

The decomposed model verified that if a mass model can accurately capture the lens galaxy's complexity, it will improve the subhalo inference. This work used information from the simulation that is not available when analysing real data, for example we utilized our true knowledge of the lens's stellar mass distribution. Nevertheless, we believe these models can be translated to real data, where the light emitted from the lens galaxy acts as a tracer for the stellar mass, information which is often omitted when modeling a strong lens (e.g. by assuming a power-law mass model). This approach to lens modeling was explored in Nightingale et al. (2019), who fitted a decomposed stellar plus dark matter to three strong lenses. The authors showed that all three lenses showed isophotal twists in their stellar emission and that when this was modelled using two stellar components with

different ellipticities and position angles it improved the mass model compared to a model assuming a single elliptical geometry. We are now investigating whether these lens systems produce subhalo detections, which would be indicative of a false positive.

The decomposed model must also make assumptions in converting light to mass. For example, whether the Sérsic profiles representing each stellar component share the same mass-to-light ratio or whether each ratio is a free parameter in the model. For each component, one must also choose whether the lens model accounts for a radially varying M/L (Napolitano et al., 2005, Tortora et al., 2011, Ge et al., 2021). The assumption of an elliptical NFW profile to describe the dark matter poses another possible mismatch. The main concern on small scales is whether the central slope, which in simulations is affected by the presence of baryons, is equal to the NFW one. To take this into account when modelling real data, we could model the dark matter as a profile with a free central slope, e.g. a generalized NFW profile (Zhao, 1996), or explicitly model the way baryons are expected to alter the dark matter distribution (Cautun et al., 2020, Callingham et al., 2020). We do not expect this to be a significant issue since for galaxy-galaxy strong lensing, the dark matter mass is typically sub-dominant in the region of interest (e.g. Li et al., 2016a, 2019). In future work we will seek to understand the importance of all these different assumptions with a view to improving the dark matter subhalo inference.

### 4.6.4 Subhalo Sensitivity

If the decomposed model can be successfully fitted to real data, it also has implications for how sensitive strong lensing is to low mass dark matter subhaloes. Firstly, if the method is able to reduce or remove the Bayesian evidence thresholds applied by works like Vegetti et al. (2014) to remove false positives, this will make us sensitive to lower mass subhaloes (which produce smaller evidence increases). Furthermore, because the decomposed model uses the stellar light as additional information which constrains the mass model, this may further boost one's sensitivity

to subhaloes by reducing the degeneracy between the lens galaxy's mass model and subhalo. This will require that sensitivity mapping of a strong lens, which quantifies what mass subhaloes one will detect if truly present in the data (Despali et al., 2020, He et al., 2022a, Amorisco et al., 2022), is performed using the decomposed model, as opposed to the power law model assumed in previous studies. The same level of care will be necessary in understanding how robust assumptions associated with the M/L and dark matter are.

### 4.6.5 Other Lensing Studies

A mass model mismatch has also been discussed in the analysis of strongly lensed quasars. Hsueh et al. (2017) showed that the flux ratio anomalies observed in lens system CLASS B0712+472 can be largely resolved by additionally adding a disk profile to the lensing model. The works of Gomer and Williams (2020, 2021), Cao et al. (2021), Van de Vyvere et al. (2022) show that such mismatches can impact on the inference of the Hubble constant via time-delay cosmology.

## 4.7 Conclusions

With a large increase in the number of observed galaxy-galaxy strong lenses expected within this decade, strong lensing could soon push the constraints on the halo mass function to low enough masses that it provides evidence in favour of or against warm dark matter models. However, detecting dark matter subhaloes through strong lensing is a challenging problem due to the complexity of the lens galaxy's mass distribution. In this work, we use a massive elliptical galaxy extracted from a state-of-the-art hydrodynamic simulation to create mock strong lens images. We represent the simulated galaxy's projected mass distribution as a sum of elliptical Gaussian profiles, which shows departures from the idealized elliptically symmetric mass models typically employed to analyse strong lenses (e.g. the power law profile (Tessore and Metcalf, 2015)). We project the same simulated galaxy

along two different line-of-sight directions, with one projection producing a pointy "American football like"-shape and the other one appearing rounder.

For each projection, we simulate three strong lens imaging datasets. The first dataset does not include a dark matter subhalo, whereas the other two include a $M_{200} = 5 \times 10^8$ $M_\odot$ and $M_{200} = 5 \times 10^9$ $M_\odot$ dark matter subhalo near the lensed source's light. To every dataset, we fit two lens mass models: (i) an elliptical broken power law (eBPL) mass model (O'Riordan et al., 2019) which represents the overall mass distribution of the lens galaxy (e.g. stars and dark matter) and; (ii) a decomposed model that models the stellar and dark matter mass separately (using the stellar particle data from the simulation to constrain part of the stellar mass model). For both models, we investigate fits which include a dark matter subhalo in the lens mass model, and therefore quantify whether we can accurately recover a dark matter subhalo when it is included in the simulation as well as whether we incorrectly infer the presence of a subhalo when it is not truly there; a false positive.

Our main results can be summarized as follows:

- When using an eBPL model to fit the lens mass to the pointy projection without a dark matter subhalo, a false-positive detection is inferred at over $3\sigma$ confidence. For the same projection, when a $5 \times 10^8$ $M_\odot$ or $5 \times 10^9$ $M_\odot$ subhalo is added to the mock lens, the fit correctly recovers the subhalo but overestimates its mass by a factor of $4 - 5$, with the true input mass outside the inferred 99% credible regions. However, when modelling data from the projection with a rounder convergence, the eBPL model does not give a false-positive and recovers the input $5 \times 10^9$ $M_\odot$ subhalo's mass accurately (the $5 \times 10^8$ $M_\odot$ subhalo is not detected due to insufficient data quality).

- When using the decomposed model to fit the lens mass, for both projections, we get no false positives and correctly recover the properties of an input subhalo when there is sufficient data quality to detect it.

The eBPL total mass model therefore shows undesirable results, including false positives and an inaccurate estimate of the subhalo mass, which the decomposed mass model does not. We speculate that this is because the eBPL parameterization does not capture aspects of the simulated lens's mass distribution. In particular, the eBPL does not capture the varying ellipticity and orientation seen in the pointy projection's mass distribution. The decomposed mass model does not assume a single elliptical mass distribution and can therefore account for this variation in ellipticity and orientation. Its improved model of the lens galaxy's mass therefore offers an improved subhalo inference which does not suffer false-positive detections.

**Our results do not imply that previous detections of dark matter subhaloes in strong lenses are false positives** (e.g. Vegetti et al. (2014)). These studies are fully aware of the false positive phenomena and they require a subhalo detection to pass stringent criteria to be considered a genuine dark matter subhalo. This includes a pixel-based correction to the gravitational potential (Koopmans, 2005) which accounts for the types of deficiencies in the mass model discussed in this work. In fact, our work demonstrates that dark matter substructures can be successfully detected in images of strong lenses, even when the lens galaxy's mass distribution is more complex than the mass model assumed to fit it.

Our work highlights the benefits of using cosmological simulations to test strong lens modeling methodology. When the eBPL showed inaccurate results, we were able to compare directly to the simulation's particle data in order to understand what complexity the model is missing. This is not possible when analysing real images of strong lenses. We are now looking to apply what we have learned in this study to real data, and fit strong lenses from existing lens samples with decomposed mass models which, crucially, relax the assumption of a single axis of ellipticity. Applying the models to real data has challenges, for example instead of relying on the simulation's stellar particle data we will need to use the lens's light to constrain the stellar mass (Nightingale et al., 2019). However, the pay-off could be huge, allowing us to more reliably detect lower mass dark matter substructures, that could

potentially push our sensitivity down to pivotal masses of $M_{200} = 5 \times 10^8$ $M_\odot$ where many viable alternatives to the cold dark matter model begin to make different, testable predictions.

Chapter 5

# Overall Conclusions & Future Work

ΛCDM, as the most commonly accepted cosmology paradigm, has been extremely successful in explaining and predicting many observations. It describes a universe in which structures form hierarchically from small scales to large due to gravitational instability, where dark matter, as the dominant matter component, plays a key role. However, although dark matter exists widely throughout the Universe, its nature remains unclear and understanding the nature of dark matter has become one of the most important and challenging tasks for modern physics. In this thesis, we focus on methods of constraining the dark matter particle mass through perturbations to strong gravitational lensing images by dark matter haloes, which utilize the fact that dark matter models with different particle masses predict different "cut-off" masses to their halo mass functions. In particular, constraints at the sub-galaxy mass range can rule out the cold dark matter model or its popular alternative, warm dark matter, with the latter typically corresponding to a particle with a mass of several keV. In this thesis, we study topics related to constraining the halo mass function in that mass range through strong gravitational lensing. Below we summarize our work for each chapter and briefly discuss some relevant challenges and future work.

In chapter 2, we investigate a forward-modelling procedure applied to a set of strong lensing systems to directly place constraints on the dark matter halo mass function. The method follows the work of Gilman et al. (2019), but is modified and developed to be used on lensing images with extended arcs. To be specific, our inference procedure is built under the Approximate Bayesian Computation framework (see Fig. 2.2 for the flow chart of the procedure). We first simulate a large number of strong lensing images (forward models) based on the best-fit macro model, with different simulated images having different populations of low-mass dark matter haloes, corresponding to different dark matter models (with different mass function cut-offs). Then we analyze those simulated images in the same way as we analyzed the original observation and compare the best-fit residuals of simulations with the observed best-fit residuals. We use the power spectrum of residuals as a summary statistic to quantify the "similarities" between the observation and different models and further derive the posterior distribution for the location of a cut-off in the halo mass function.

We find that for our mock tests, the true input cut-offs can be correctly and unbiasedly recovered through analyzing the power spectrum of best-fit residuals using the forward-modelling procedure (see Fig. 2.7, 2.8, 2.9 & 2.10). For a relatively "cold" dark matter model, where the particle mass is 8.86 keV, particles with mass less than 4.10 keV lie outisde of the 95% credible region, while for a warmer case with a true mass of 2.22 keV, the recovered 95% credible region is between 1.43 and 3.21 keV. It is noted that with the standard data quality we assume, which is comparable with the highest quality systems from the SLACS sample, even combining 50 systems together still results in large intrinsic scatter in the distributions of low-mass perturbers (see blue dashed lines in Fig. 2.7). We have also investigated how the procedure would behave for different quality observations. We find (see Fig. 2.9 & 2.10), that the signal would be boosted with deeper images, higher resolution and a larger intercepting volume for luminous arcs along the line of sight (as there are then more perturbers for a given DM model). We find that with worse

resolution than typical HST images, like EST and CSST images, the method can still put some constraints on the mass range of interest, which makes it promising for future observations that will produce catalogues of many tens of thousands of strong lensing images.

In chapter 3, we re-investigate the sensitivity maps of line-of-sight and in-lens low-mass perturbers. The sensitivity function quantifies the chance of detecting a dark halo of a certain mass at a certain position for a given strong lensing system. In previous work, to reduce the complexity introduced by the freedom of a perturber's redshift, an "effective mass" is assumed to exist whereby the perturber would produce the same lensing effects as a halo at the lens plane with mass equal to this effective mass. The "effective mass" is usually obtained through fitting to deflection angle fields. In our work, we instead take a more brute-force way to compute the sensitivity maps which involves repeatedly simulating and modelling strong lens images of a specific lens systems with a low-mass perturber added at different places with different masses (see Fig. 3.4 for the flow chart of the procedure). The key difference between our methods and previous method is that we now involve more realistic modelling processes on datasets with realistic noise.

We find that an NFW perturber causes the largest lensing perturbation when close to the lens redshift which is contrary to previous findings where a perturber produces a larger perturbation as it gets closer to the observer (see Fig. 3.7). Two possible reasons account for the difference: first, the previously used assumption that a line-of-sight perturber is equivalent to a perturber in the main lens plane with a mass equal to an "effective mass" is not a good approximation, as many asymmetric deflection patterns (caused by multi-plane lensing) are ignored as shown in Fig. 3.5; Second the degeneracy between the macro model and the low-mass perturber is ignored in previous work, and the perturbation of a low-mass halo in-front of the lens can be more easily absorbed by modifying the main lens than for a peturber in the macro lens plane. With our new method of computing the sensitivity, we further compare the relative contributions of line-of-sight and on-lens

perturbers. For the abundance and properties of on-lens haloes, we calibrate them with a high-resolution hydrodynamic simulation run by Richings et al. (2021). Our calculation shows that the contribution from line-of-sight haloes is still important, but no longer dominates the total number of detectable perturbers in most cases (see Fig. 3.9). We have also explored how the detectable number of low-mass perturbers would change with different image settings (see Fig. 3.9). We find that the benefit from increasing exposure time might not be as large as observing more systems because increasing exposure time by 4 times only doubles the detectable numbers.

In chapter 4, we explore how the complexity of the lens galaxy's mass distribution would affect subhalo detection. We build up our mock lensing images by taking our lens galaxy from a high-resolution hydrodynamic simulation, where we expect the simulated galaxy to have similar complexity to realistic galaxies such as asymmetry and twisting ellipticity. However, although having the highest resolution of a hydrodynamical simulation of a galaxy group so far, the simulated galaxy still suffers an unrealistic central density core, with a size of several hundred parsecs due to the limited resolution. To avoid the effects of particle noise and potential boundary truncation effects as seen in typical strong lensing simulations from particle data, we instead use a sum of many 2D Gaussians to model the mass distribution of different components of the simulated galaxy (a so-called multi Gaussian expansion), and simulate lensing images based on these best-fit Gaussians. We project the simulated galaxies into two different line-of-sight directions to obtain different galaxy "shapes". Finally, we simulate images for both projections with and without a subhalo to test how different mass models affect subhalo inference. Two kinds of lens mass models are tested in our work: an elliptical (broken) power law and a decomposed model, where we separately model the stellar and dark matter component of the lens galaxy. The source is modelled as a pixelised one.

We find that for one projection where the galaxy exhibits "pointy" deviations from ellipticity (also known as "discy"), the power law model gives a clear false-positive

signal when fitting to an image without a subhalo, and overestimates the subhalo's mass by $4-5$ times when a $5\times10^8$ or $5\times10^9$ $M_\odot$ subhalo is input (Fig. 4.6 & 4.7). However, when fitting to a projection with a rounder 2D shape of the lens galaxy, the power law model returns no-false positives for the case without a subhalo and recovers the true values of a $5\times10^9$ $M_\odot$ input subhalo within the $3\sigma$ credible region (Fig. 4.6 & 4.8). When using the decomposed model to fit the lens mass, for both projections, we get no false-positive signals in the no-subhalo cases and correctly recover the input subhalo except for missing a $5\times10^8$ $M_\odot$ one in Projection 2 due to limited data quality (Fig. 4.11, 4.12 & 4.13). This work confirms that an incorrect inference on the number and properties of subhaloes could be made due to a mismatch between the lens mass model and the real lens mass distribution, and indicates the necessity of extending our lens mass models with more complexity when searching for subhaloes through strong lensing.

Overall, in the thesis we have improved various aspects of methods that use strong lensing to constrain the halo mass function, thus preparing for the imminent discovery of hundreds of thousands of galaxy-galaxy strong lensing systems from new telescopes. We note we still make many assumptions and simplifications and there is further development needed to apply the models and methods of this thesis to realistic observations. This will be the aim of our future work. For the forward-modelling method developed in chapter 2, the challenge exists in the accuracy one can reach for the macro model. We could imagine that the subhalo signals could be biased or totally removed by a significant mismatch in either the lens mass or source light distributions. We have seen in chapter 4 that a mismatch between the lens model and true mass distribution could lead to an incorrect inference on the properties of detected subhaloes, and we would expect similar things could happen with the forward-modelling method. There are modifications that can possibly solve these issues. One is to further improve the mass and source model such that the scale of any mismatch in the macro structures is smaller than the perturbations due to low-mass haloes. Another is to search for a better summary statistic than

the power spectrum that is more sensitive to the perturbations of low-mass haloes. Considering the large number of possible summary statistics, we think this might be best done through a training-based machine learning technique, which hopefully can automatically extract the characteristic imprints of low-mass halo perturbations to strong lensing images. The obstacle faced by the sensitivity mappings discussed in chapter 3 is more on the engineering side rather than the science. The bottleneck is the speed of computing the sensitivity maps when using a pixelised source, which is much slower than the parametric source model used in our work. However, in the worst case of not finding a way to speed up these calculations, we can still afford to compute sensitivity maps for several lensing systems which can already put a strong constraint on the halo mass function. Finally, for the work of chapter 4, as we mention, although the decomposed model does well at capturing the complexity of the simulated galaxy, it might not be so successful in real applications where the stellar mass may not exactly trace the stellar light, and a more complex model with a gradient in the mass-to-light ratio may be necessary. One interesting and important piece of future work in this direction is to simulate full lensing images with lens light (even colour) also generated from simulated data and then use them as a guide to explore the complexity we need in our models. Also, at that stage, a more complex source than a simple cored-Sérsic should be used when simulating mock images, to ensure that the method is not limited to dealing with the case of simple source morphologies.

# Appendix A

## A.1 Determining Multiplane Resolution

In chapter 2, we simulate the effect of line-of-sight haloes by dividing the lightcone from the observer to the source galaxy into a number of intervals and approximating low-mass dark matter haloes within a given redshift interval as lying on a single plane at the central redshift. Reducing the redshift interval, $\Delta z$, between two neighbouring planes (increasing the number of multiplanes) will increase the accuracy of the approximation to the line-of-sight effects, but will also increase the computational cost. The smallest allowable $\Delta z$ should be determined by the accuracy one would like to achieve in the inference of $M_{\rm hf}$. In practice, one needs to make sure the "difference" caused by approximating line-of-sight effects into multiplanes is smaller than the "difference" caused by changing $M_{\rm hf}$ by the amount one would like to distinguish.

Fig. A.1 shows an example of the amplitudes of the differences in deflection angles when changing the values of $\Delta z$ and $M_{\rm hf}$. The two panels are computed from the same macro settings (a spherical isothermal sphere model with $R_{\rm E}$ of $1.5''$ at $z = 0.5$ and a source at $z = 1.0$) and the same low-mass dark matter haloes (generated from a distribution with $M_{\rm hf} = 10^7$ $\rm M_\odot$). To simplify the test, instead of using the mass function described in the main body of the paper, we impose a "sharp

cut" on the mass function, such that no haloes are drawn with $M_{200}$ smaller than $M_{\rm hf}$. Also, we assume that there is no correlation between $M_{\rm hf}$ and the mass-concentration relation to make sure massive haloes are unchanged when changing $M_{\rm hf}$.

The upper panel of Fig. A.1 shows the amplitudes of the differences in deflection angles when changing $\Delta z$ from 0.01 to 0.001 (a very high resolution setting which we take as the "accurate" result). The lower panel shows the amplitudes of the differences in deflection angles when changing $M_{\rm hf}$ from $10^7$ $\mathrm{M}_\odot$ to $10^{7.1}$ $\mathrm{M}_\odot$. As seen from the figure, the patterns of the differences caused by changing $\Delta z$ and $M_{\rm hf}$ are different. We use the mean amplitude of the difference in deflection angles within the annular region $1.0'' - 2.0''$ (the region between the two dashed circles in the figure) to quantify the "differences". The mean difference caused by changing $\Delta z$ is $3.47 \times 10^{-5}$ arcsec, which is smaller than the mean difference caused by changing $M_{\rm hf}$ by 0.1 dex, $2.42 \times 10^{-4}$ arcsec, suggesting that $\Delta z$ of 0.01 would not affect the ability to distinguish between models with $M_{\rm hf} = 10^7$ $\mathrm{M}_\odot$ and $10^{7.1} M_\odot$.

The results shown in Fig. A.1 are for a special case, so we repeat the same procedure for 128 different realisations of low-mass dark matter haloes. The orange histogram in Fig. A.2 shows the distribution of the $\log_{10}$ ratio of the mean difference in amplitudes defined previously, that is the ratio of the mean difference in the deflection angles between models with $M_{\rm hf} = 10^7$ and $\mathrm{M}_\odot = 10^{7.1}$ divided by the mean difference in the deflection angles for the $\Delta z$ given in the legend. As shown by the orange histogram, the ratios from all of the 128 realisations are larger than one, indicating that the differences caused by approximating line-of-sight effects using multiplanes separated by 0.01 in redshift is smaller than the difference cause by changing $M_{\rm hf}$ by 0.1 dex. Also, we plot the histogram of ratios for other values of $\Delta z$. As may be seen, increasing $\Delta z$ increases the differences caused by changing $\Delta z$ and, in some cases, the differences are larger than those caused by changing $M_{\rm hf}$ by 0.1 dex. To summarize, the value of $\Delta z$ we adopt for our tests, $\Delta z = 0.01$,

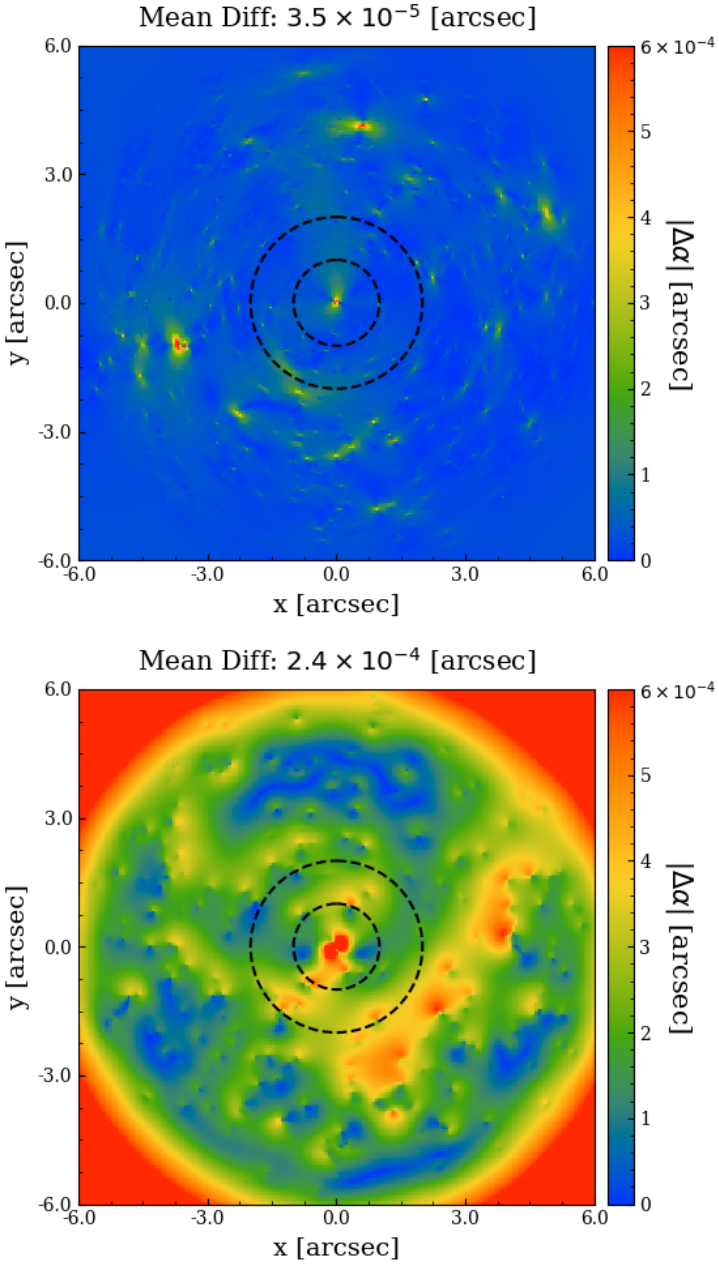


Figure A.1: **Upper panel**: amplitude of the differences in deflection angles caused by changing $\Delta z$ from 0.01 to 0.001. **Lower panel**: amplitude of the differences in deflection angles caused by changing $M_{\rm hf}$ from $10^7$ $M_\odot$ to $10^{7.1}$ $M_\odot$. The region between two dashed circles is the annulus between $1.0''$ and $2.0''$. The unit of the colourbar is arcsecs.

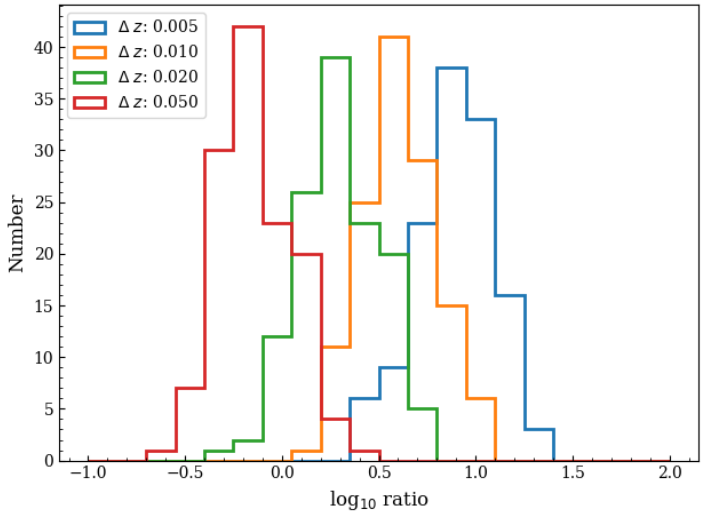


Figure A.2: Histograms of the $\log_{10}$ ratio of the mean amplitude of the differences in deflection angles caused by changing $\Delta z$ and $M_{\rm hf}$. Blue, orange, green and red colors shows results for $\Delta z = 0.005$, 0.01, 0.02 and 0.05 respectively.

does not affect our inference of $M_{\rm hf}$ to an accuracy of 0.1 dex.

# Appendix B

## B.1 Parametric source results

The work of chapter 4 primarily focuses on the lens mass distribution. The effects of source modelling on the subhalo inference is seldom discussed. In this section, to give a brief idea on how our results would be affected by source modelling, we fit the same mock data with the same mass models discussed above but with a parametric source model. To be specific, the source model we apply here has the same form used to simulated the data, which is an elliptical cored Sérsic profile. When simulating mock data, we have fixed its break radius to be $0.01''$, but when using it as a source model, we set its break radius to be a free parameter.

The increase in log likelihood for many model-fits including a subhalo, $\Delta L$, are higher when we assume that the source is an elliptical cored Sérsic profile as opposed to a pixelised source. This is because the pixelised source models have a much higher level of freedom in how they fit the data. If a mass model provides a good – but not perfect – fit, the pixelisation can make small adjustments to the source pixel values to fit the data equally well (Gilman et al., 2020c). This is appropriately penalized using a Bayesian framework (see Suyu et al. (2006) and Nightingale et al. (2018)), but nevertheless produces smaller likelihood contrasts than fitting a parametric source model like the cored Sérsic profile, which has a lot

less freedom in adjusting its parameters in order to account for an inaccurate mass model. This is also dependent on the fact that the elliptical cored Sérsic profile was used to both simulate and fit the mock strong lenses; had there been a mismatch here parametric fits would likely not give such large $\Delta L$ values.

In Fig. B.1, we show $\Delta L$ when fitting the data with an eBPL profile. For projection 1, for both the smooth case and a $5 \times 10^8$ $M_\odot$ subhalo input case, the eBPL plus cored Sérsic source model returns similar results, with a highest $\Delta L$ giving $\sim 250$ at the middle left region indicating the existence of a $10^{10.1^{+0.2}_{-0.1}}$ $M_\odot$ subhalo, which is not consistent with our input (e.g. it is a false positive). For the case of a $5 \times 10^9$ $M_\odot$ input subhalo, the highest $\Delta L$ is $\sim 600$ around the middle right region, which is consistent with our input. For this case, we further model the subhalo by freeing its position and the posterior we get is shown in color red in Fig. B.2. We see that although the position is estimated around the true input, the subhalo's mass is overestimated by around 4 times, which is similar to our previous findings for a pixelised source.

For projection 2, we see that for the smooth test case, false-positive signals show up in upper right regions with the highest $\Delta L$ to be $\sim 18$. Read from the grid of highest $\Delta L$, the best-fit subhalo's mass is $10^{9.3^{+0.4}_{-0.5}}$ $M_\odot$. False positives were not detected for this projection using a pixelised source. For the case of an input subhalo of $5 \times 10^8$ $M_\odot$, there are some plausible signals around the middle right regions with the highest $\Delta L$ to be $\sim 8$. The mass of the plausible subhalo obtained in this case is $10^{9.6^{+0.2}_{-0.5}}$ $M_\odot$. For the third case where a $5 \times 10^9$ $M_\odot$ subhalo added, the $\Delta L$ map returns the correct answer with the highest $\Delta L$ to be 120 at the place where we input the subhalo. For this one, similarly, we further model the subhalo by freeing its position. The posterior is shown in color blue in Fig. B.2. We see that the input subhalo can be well recovered in this case.

In Fig. B.3, we show $\Delta L$ maps of modelling the data with the decomposed model plus a cored Sérsic source. We see that the results are similar to the pixelisation results: for smooth tests, no clear false-positive signals show up. For subhalo tests,

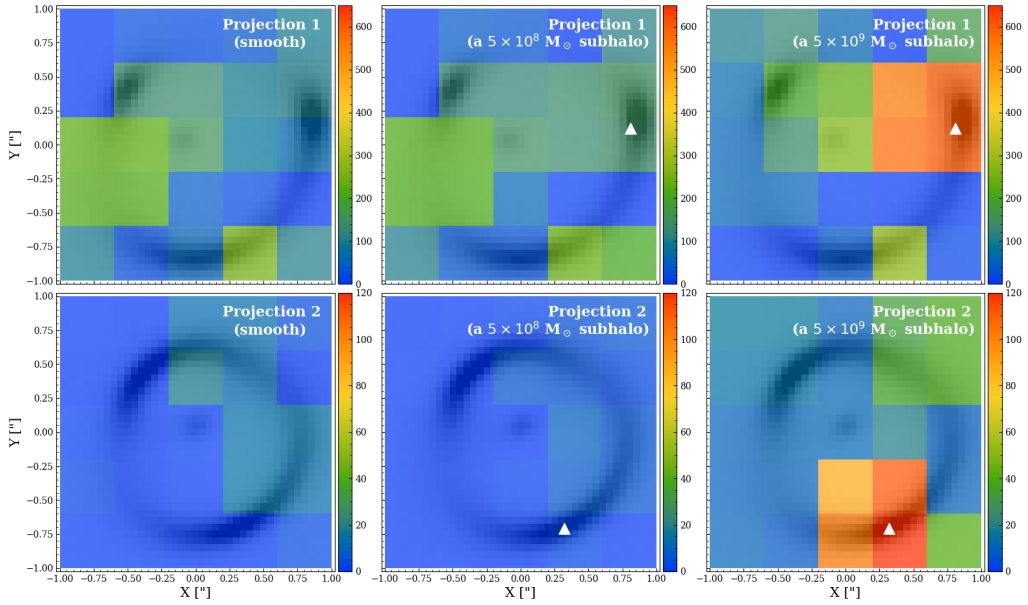


Figure B.1: $\Delta L$ maps of using eBPL + cored Sérsic source model. Colours indicate the increase in maximum log likelihood, $\Delta L$, when a subhalo is included inside $0.4'' \times 0.4''$ squares during a fit to a lens that has: no subhalos (left), a subhalo of mass $5 \times 10^8$ $M_\odot$ (middle), or a subhalo of mass $5 \times 10^9$ $M_\odot$ (right). Top and bottom rows show the results for Projection 1 and 2 (with different colour scales). White triangles mark the true locations of the subhaloes.

the highest $\Delta L$ is consistent with the region of an input subhalo. In Fig. B.4, we further plot the posteriors obtained for the detected subhaloes. Overall, input subhaloes can be recovered to a good level although for the $5 \times 10^9$ $M_\odot$ subhalo cases, the recovered masses are slightly offset to the true value, albeit this is close enough that it could simply be due to noise in the mock observation.

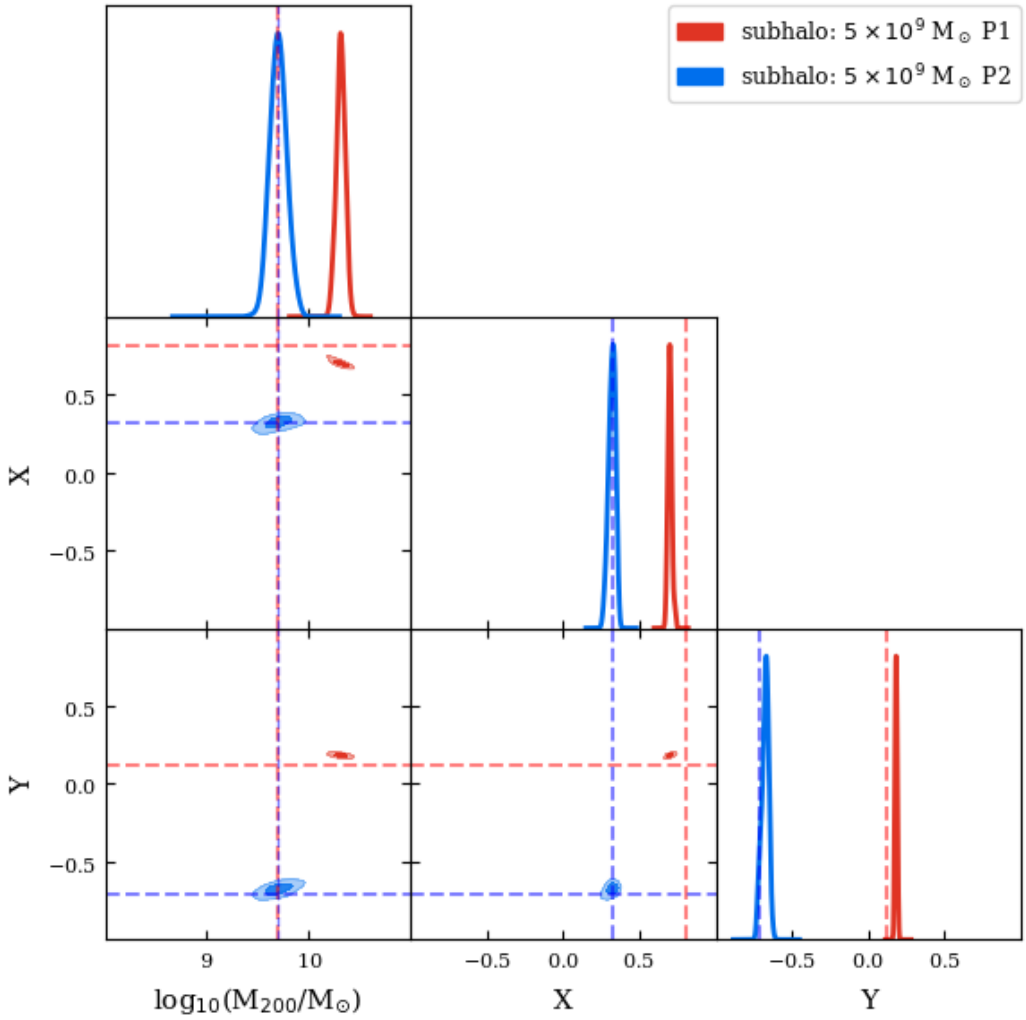


Figure B.2: Posteriors of detected subhalo parameters of eBPL + cored Sérsic model. The red posteriors show the results for an input of a $5 \times 10^9$ $M_\odot$ subhalo in Projection 1. The blue posteriors show the results for an input of a $5 \times 10^9$ $M_\odot$ subhalo in Projection 2. The 2D contours cover the 68% and 99% confidence regions. The dashed lines in corresponding colors marked the true input values.

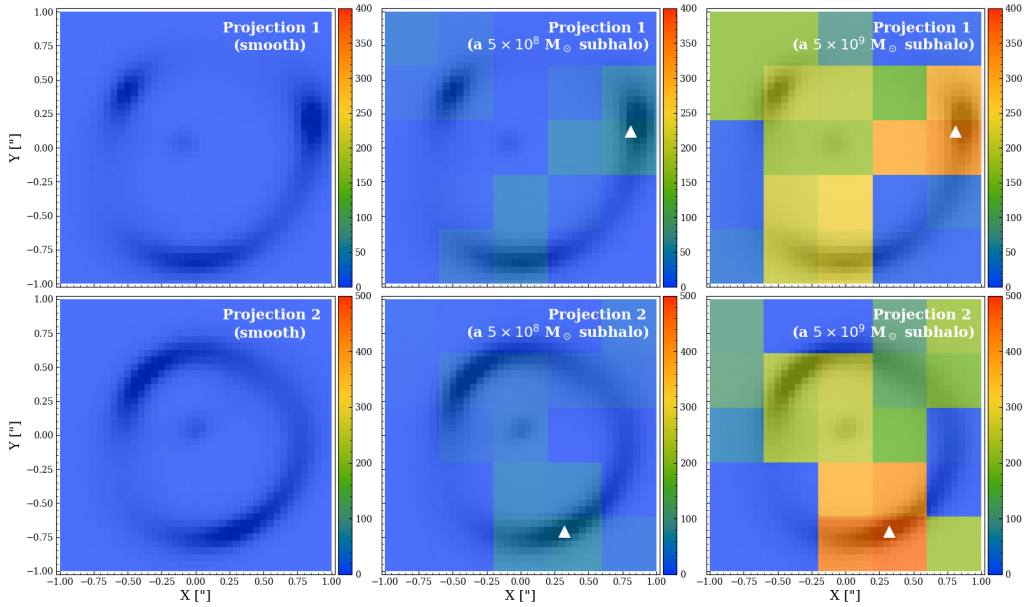


Figure B.3: $\Delta L$ maps of using stellar + dark matter + cored Sérsic source model. Colours indicate the increase in maximum log likelihood, $\Delta L$, when a subhalo is included inside $0.4'' \times 0.4''$ squares during a fit to a lens that has: no subhalos (left), a subhalo of mass $5 \times 10^8$ $M_\odot$ (middle), or a subhalo of mass $5 \times 10^9$ $M_\odot$ (right). Top and bottom rows show the results for Projection 1 and 2 (with different colour scales). White triangles mark the true locations of the subhaloes.

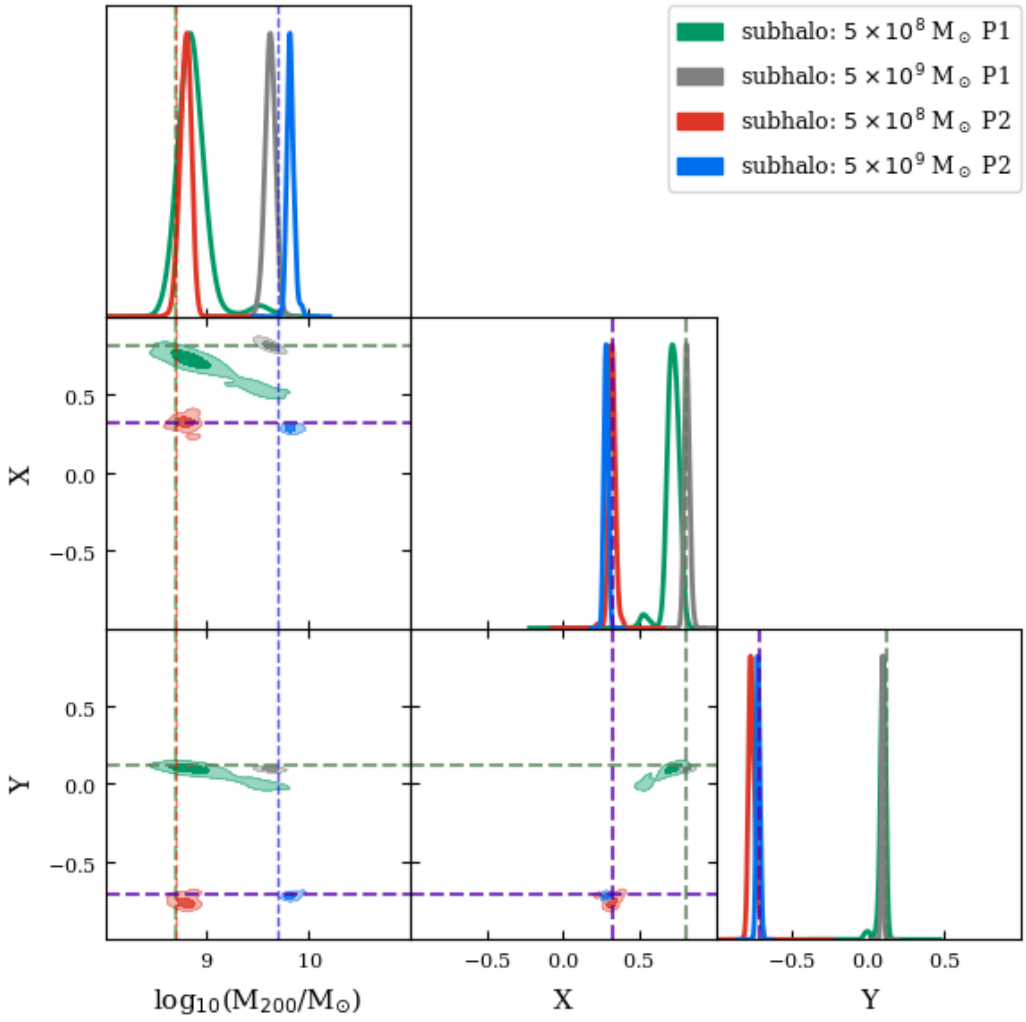


Figure B.4: Posteriors of detected subhalo parameters of the stellar + dark matter + cored Sérsic source model. The green, grey, red and blue posteriors respectively show the results for: an input of a $5 \times 10^8$ $M_\odot$ subhalo in Projection 1; an input of a $5 \times 10^9$ $M_\odot$ subhalo in Projection 1; an input of a $5 \times 10^8$ $M_\odot$ subhalo in Projection 2; an input of a $5 \times 10^9$ $M_\odot$ subhalo in Projection 2. The 2D contours cover the 68% and 99% confidence regions. The dashed lines in corresponding colors marked the true input values.

# Bibliography

Akeret, J., Refregier, A., Amara, A., Seehars, S. and Hasner, C. *J. Cosmology Astropart. Phys.*, 2015(8):043, Aug. 2015.

Akerib, D.S. et al. *Physical Review Letters*, 118(2):021303, Jan. 2017.

Amara, A., Metcalf, R.B., Cox, T.J. and Ostriker, J.P. *MNRAS*, 367(4):1367–1378, Apr. 2006.

Amorisco, N.C. et al. *MNRAS*, 510(2):2464–2479, Feb. 2022.

Aprile, E. and Xenon Collaboration. The XENONnT Dark Matter Experiment. In *APS April Meeting Abstracts*, page J9.003, Jan. 2017.

Baltz, E.A., Marshall, P. and Oguri, M. *J. Cosmology Astropart. Phys.*, 2009(1): 015, Jan. 2009.

Banik, N., Bovy, J., Bertone, G., Erkal, D. and de Boer, T.J.L. *J. Cosmology Astropart. Phys.*, 2021(10):043, Oct. 2021.

Bayer, D. et al. *arXiv e-prints*, art. arXiv:1803.05952, Mar. 2018.

Benitez-Llambay, A. and Frenk, C. *MNRAS*, 498(4):4887–4900, Nov. 2020.

Benson, A.J., Frenk, C.S., Lacey, C.G., Baugh, C.M. and Cole, S. *MNRAS*, 333 (1):177–190, June 2002.

Bentley, J.L. *Commun. ACM*, 18(9):509–517, sep 1975.

Birrer, S., Amara, A. and Refregier, A. *J. Cosmology Astropart. Phys.*, 2017(5): 037, May 2017a.

Birrer, S., Welschen, C., Amara, A. and Refregier, A. *J. Cosmology Astropart. Phys.*, 2017(4):049, Apr. 2017b.

Bolton, A.S., Burles, S., Koopmans, L.V.E., Treu, T. and Moustakas, L.A. *ApJ*, 638(2):703–724, Feb. 2006.

Bolton, A.S. et al. *ApJ*, 757(1):82, Sept. 2012.

Bose, S. et al. *MNRAS*, 455(1):318–333, Jan. 2016.

Brehmer, J., Mishra-Sharma, S., Hermans, J., Louppe, G. and Cranmer, K. *ApJ*, 886(1):49, Nov. 2019.

Brewer, B.J., Huijser, D. and Lewis, G.F. *MNRAS*, 455(2):1819–1829, Jan. 2016.

Buchner, J. et al. *A&A*, 564:A125, Apr. 2014.

Bundy, K. et al. *ApJ*, 798(1):7, Jan. 2015.

Callingham, T.M. et al. *MNRAS*, 495(1):12–28, June 2020.

Cao, X. et al. *Research in Astronomy and Astrophysics*, 2021.

Cappellari, M. *MNRAS*, 333(2):400–410, June 2002.

Cappellari, M. *MNRAS*, 390(1):71–86, Oct. 2008.

Cautun, M. et al. *MNRAS*, 494(3):4291–4313, May 2020.

Çağan Şengül, A., Tsang, A., Diaz Rivero, A., Dvorkin, C., Zhu, H.M. and Seljak, U. *Phys. Rev. D*, 102(6):063502, Sept. 2020.

Chatterjee, S. and Koopmans, L.V.E. *MNRAS*, 474(2):1762–1772, Feb. 2018.

Collett, T.E. *ApJ*, 811(1):20, Sept. 2015.

Collett, T.E. and Auger, M.W. *MNRAS*, 443(2):969–976, Sept. 2014.

Cui, X. et al. *Physical Review Letters*, 119(18):181302, Nov. 2017.

Cyr-Racine, F.Y., Keeton, C.R. and Moustakas, L.A. *Phys. Rev. D*, 100(2):023013, July 2019.

Dalal, N. and Kochanek, C.S. *ApJ*, 572(1):25–33, June 2002.

Davies, F.B., Hennawi, J.F., Eilers, A.C. and Lukić, Z. *ApJ*, 855(2):106, Mar. 2018.

Davis, M., Efstathiou, G., Frenk, C.S. and White, S.D.M. *ApJ*, 292:371–394, May 1985.

Despali, G. and Vegetti, S. *MNRAS*, 469(2):1997–2010, Aug. 2017.

Despali, G., Vegetti, S., White, S.D.M., Giocoli, C. and van den Bosch, F.C. *MNRAS*, 475(4):5424–5442, Apr. 2018.

Despali, G., Lovell, M., Vegetti, S., Crain, R.A. and Oppenheimer, B.D. *MNRAS*, 491(1):1295–1310, Jan. 2020.

Diaz Rivero, A. and Dvorkin, C. *Phys. Rev. D*, 101(2):023515, Jan. 2020.

Díaz Rivero, A., Dvorkin, C., Cyr-Racine, F.Y., Zavala, J. and Vogelsberger, M. *Phys. Rev. D*, 98(10):103517, Nov. 2018.

Diemer, B. *ApJS*, 239(2):35, Dec. 2018.

Ding, X. et al. *MNRAS*, 503(1):1096–1123, May 2021.

Dye, S. and Warren, S.J. *ApJ*, 623(1):31–41, Apr. 2005.

Dye, S. et al. *MNRAS*, 440(3):2013–2025, May 2014.

Dye, S. et al. *MNRAS*, 452(3):2258–2268, Sept. 2015.

Efstathiou, G. *MNRAS*, 256(2):43P–47P, May 1992.

Ene, I. et al. *MNRAS*, 479(2):2810–2826, Sept. 2018.

Enzi, W., Vegetti, S., Despali, G., Hsueh, J.W. and Metcalf, R.B. *MNRAS*, 496 (2):1718–1729, Aug. 2020.

Etherington, A. et al. *MNRAS*, 517(3):3275–3302, Dec. 2022.

Fearnhead, P. and Prangle, D. *Journal of the Royal Statistical Society: Series B (Statistical Methodology)*, 74(3):419–474, 2012.

Feroz, F., Hobson, M.P. and Bridges, M. *MNRAS*, 398(4):1601–1614, Oct. 2009.

Fleury, P., Larena, J. and Uzan, J.P. *J. Cosmology Astropart. Phys.*, 2021(8):024, Aug. 2021.

Frenk, C.S. and White, S.D.M. *Annalen der Physik*, 524:507–534, Oct. 2012.

Frenk, C.S., White, S.D.M., Davis, M. and Efstathiou, G. *ApJ*, 327:507, Apr. 1988.

Frenk, C.S., White, S.D.M., Efstathiou, G. and Davis, M. *ApJ*, 351:10, Mar. 1990.

Gaia Collaboration et al. *A&A*, 616:A1, Aug. 2018.

Gao, L., White, S.D.M., Jenkins, A., Stoehr, F. and Springel, V. *MNRAS*, 355(3): 819–834, Dec. 2004.

Gao, L., Navarro, J.F., Frenk, C.S., Jenkins, A., Springel, V. and White, S.D.M. *MNRAS*, 425:2169–2186, Sept. 2012.

Garrison-Kimmel, S. et al. *MNRAS*, 471(2):1709–1727, Oct. 2017.

Garzilli, A. et al. *MNRAS*, 489(3):3456–3471, Nov. 2019.

Ge, J., Mao, S., Lu, Y., Cappellari, M., Long, R.J. and Yan, R. *MNRAS*, 507(2): 2488–2499, Oct. 2021.

Gilman, D., Birrer, S., Treu, T., Nierenberg, A. and Benson, A. *MNRAS*, page 1582, Jun 2019.

Gilman, D., Birrer, S., Nierenberg, A., Treu, T., Du, X. and Benson, A. *MNRAS*, 491(4):6077–6101, Feb. 2020a.

Gilman, D., Birrer, S. and Treu, T. *A&A*, 642:A194, Oct. 2020b.

Gilman, D., Du, X., Benson, A., Birrer, S., Nierenberg, A. and Treu, T. *MNRAS*, 492(1):L12–L16, Feb. 2020c.

Gomer, M. and Williams, L.L.R. *J. Cosmology Astropart. Phys.*, 2020(11):045, Nov. 2020.

Gomer, M.R. and Williams, L.L.R. *MNRAS*, 504(1):1340–1354, June 2021.

Goullaud, C.F., Jensen, J.B., Blakeslee, J.P., Ma, C.P., Greene, J.E. and Thomas, J. *ApJ*, 856(1):11, 2018.

Graham, A.W., Erwin, P., Trujillo, I. and Asensio Ramos, A. *AJ*, 125(6):2951–2963, June 2003.

Hahn, C., Vakili, M., Walsh, K., Hearin, A.P., Hogg, D.W. and Campbell, D. *MNRAS*, 469(3):2791–2805, Aug. 2017.

He, Q. et al. *MNRAS*, 496(4):4717–4733, Aug. 2020.

He, Q. et al. *MNRAS*, 512(4):5862–5873, June 2022a.

He, Q. et al. *MNRAS*, 511(2):3046–3062, Apr. 2022b.

Hermans, J., Banik, N., Weniger, C., Bertone, G. and Louppe, G. *MNRAS*, 507 (2):1999–2011, Oct. 2021.

Hezaveh, Y.D. et al. *ApJ*, 823(1):37, May 2016.

Hinshaw, G. et al. *ApJS*, 208(2):19, Oct. 2013.

Hsu, D.C., Ford, E.B. and Terrien, R. *MNRAS*, 498(2):2249–2262, Oct. 2020.

Hsueh, J.W. et al. *MNRAS*, 469(3):3713–3721, Aug. 2017.

Hsueh, J.W., Despali, G., Vegetti, S., Xu, D., Fassnacht, C.D. and Metcalf, R.B. *MNRAS*, 475(2):2438–2451, Apr. 2018.

Hsueh, J.W. et al. *MNRAS*, 492:3047–3059, Jan. 2020.

Huang, S. et al. *Monthly Notices of the Royal Astronomical Society*, 480(1):521–537, 2018.

Hut, P. *Physics Letters B*, 69:85–88, July 1977.

Iršič, V. et al. *Phys. Rev. D*, 96(2):023522, July 2017.

Kahn, F.D. and Woltjer, L. *ApJ*, 130:705, Nov. 1959.

Kaiser, N. *ApJ*, 284:L9–L12, Sept. 1984.

Koopmans, L.V.E. *MNRAS*, 363:1136–1144, Nov. 2005.

Lazar, A., Bullock, J.S., Boylan-Kolchin, M., Feldmann, R., Çatmabacak, O. and Moustakas, L. *MNRAS*, 502(4):6064–6079, Apr. 2021.

Li, H., Li, R., Mao, S., Xu, D., Long, R.J. and Emsellem, E. *MNRAS*, 455(4): 3680–3692, Feb. 2016a.

Li, R., Frenk, C.S., Cole, S., Gao, L., Bose, S. and Hellwing, W.A. *MNRAS*, 460 (1):363–372, July 2016b.

Li, R., Frenk, C.S., Cole, S., Wang, Q. and Gao, L. *MNRAS*, 468(2):1426–1432, June 2017.

Li, R. et al. *MNRAS*, 490(2):2124–2138, Dec. 2019.

Lovell, M.R. et al. *MNRAS*, 420(3):2318–2324, Mar. 2012.

Lovell, M.R., Frenk, C.S., Eke, V.R., Jenkins, A., Gao, L. and Theuns, T. *MNRAS*, 439(1):300–317, Mar. 2014.

Ludlow, A.D. et al. *MNRAS*, 460(2):1214–1232, Aug. 2016.

Macciò, A.V., Ruchayskiy, O., Boyarsky, A. and Muñoz-Cuartas, J.C. *MNRAS*, 428(1):882–890, Jan. 2013.

Mao, S. and Schneider, P. *MNRAS*, 295(3):587–594, Apr. 1998.

Maresca, J., Dye, S. and Li, N. *MNRAS*, 503(2):2229–2241, May 2021.

McCully, C., Keeton, C.R., Wong, K.C. and Zabludoff, A.I. *MNRAS*, 443(4): 3631–3642, Oct. 2014.

Metcalf, R.B. and Madau, P. *ApJ*, 563(1):9–20, Dec. 2001.

Metcalf, R.B. and Petkova, M. *MNRAS*, 445(2):1942–1953, Dec. 2014.

Minor, Q., Kaplinghat, M., Chan, T.H. and Simon, E. *MNRAS*, July 2021.

Muñoz, J.A., Kochanek, C.S. and Keeton, C.R. *ApJ*, 558(2):657–665, Sept. 2001.

Mukherjee, S. et al. *MNRAS*, 479(3):4108–4125, Sept. 2018.

Mukherjee, S. et al. *MNRAS*, 504(3):3455–3477, July 2021.

Napolitano, N.R. et al. *MNRAS*, 357(2):691–706, Feb. 2005.

Navarro, J.F., Frenk, C.S. and White, S.D.M. *ApJ*, 462:563, May 1996.

Navarro, J.F., Frenk, C.S. and White, S.D.M. *ApJ*, 490(2):493–508, Dec. 1997.

Newton, O. et al. *J. Cosmology Astropart. Phys.*, 2021(8):062, Aug. 2021.

Nierenberg, A.M., Treu, T., Wright, S.A., Fassnacht, C.D. and Auger, M.W. *MNRAS*, 442(3):2434–2445, Aug. 2014.

Nierenberg, A.M. et al. *MNRAS*, 471(2):2224–2236, Oct. 2017.

Nightingale, J.W., Dye, S. and Massey, R.J. *MNRAS*, 478(4):4738–4784, Aug. 2018.

Nightingale, J.W. et al. *MNRAS*, 489(2):2049–2068, Oct. 2019.

Nightingale, J.W., Hayes, R.G. and Griffiths, M. *Journal of Open Source Software*, 6(58):2550, 2021a.

Nightingale, J.W. et al. *Journal of Open Source Software*, 6(58):2825, 2021b.

Oh, S., Greene, J.E. and Lackner, C.N. *ApJ*, 836(1):115, 2017.

O'Riordan, C.M., Warren, S.J. and Mortlock, D.J. *MNRAS*, 487(4):5143–5154, Aug. 2019.

O'Riordan, C.M., Warren, S.J. and Mortlock, D.J. *MNRAS*, 496(3):3424–3435, Aug. 2020.

O'Riordan, C.M., Warren, S.J. and Mortlock, D.J. *MNRAS*, 501(3):3687–3694, Mar. 2021.

Petkova, M., Metcalf, R.B. and Giocoli, C. *MNRAS*, 445(2):1954–1966, Dec. 2014.

Planck Collaboration et al. *A&A*, 594:A13, Sept. 2016.

Planck Collaboration et al. *A&A*, 641:A6, Sept. 2020.

Quinn, J. et al. *MNRAS*, 459(3):2394–2407, July 2016.

Richings, J. et al. *MNRAS*, 492(4):5780–5793, Mar. 2020.

Richings, J., Frenk, C., Jenkins, A., Robertson, A. and Schaller, M. *MNRAS*, 501 (3):4657–4668, Mar. 2021.

Ritondale, E., Vegetti, S., Despali, G., Auger, M.W., Koopmans, L.V.E. and McKean, J.P. *MNRAS*, 485(2):2179–2193, May 2019.

Rozo, E. et al. *ApJ*, 708(1):645–660, Jan. 2010.

Rubin, V.C. and Ford, Jr., W.K. *ApJ*, 159:379, Feb. 1970.

Sahu, K.C. et al. *ApJ*, 933(1):83, July 2022.

Sawala, T. et al. *MNRAS*, 456(1):85–97, Feb. 2016.

Sawala, T. et al. *MNRAS*, 467(4):4383–4400, June 2017.

Schaye, J. et al. *MNRAS*, 446(1):521–554, Jan. 2015.

Scherrer, R.J. and Turner, M.S. *Phys. Rev. D*, 33:1585–1589, Mar 1986.

Schneider, A., Smith, R.E., Macciò, A.V. and Moore, B. *MNRAS*, 424(1):684–698, July 2012.

Schneider, P. *Astronomy and Astrophysics*, 568:L2, aug 2014.

Schneider, P., Ehlers, J. and Falco, E.E. *Gravitational Lenses*. 1992. doi: 10.1007/978-3-662-03758-4.

Sérsic, J.L. *Boletin de la Asociacion Argentina de Astronomia La Plata Argentina*, 6:41–43, Feb. 1963.

Shajib, A.J. *MNRAS*, 488(1):1387–1400, Sept. 2019.

Sheth, R.K. and Tormen, G. *MNRAS*, 308(1):119–126, Sept. 1999.

Sheth, R.K., Mo, H.J. and Tormen, G. *MNRAS*, 323(1):1–12, May 2001.

Shu, Y. et al. *ApJ*, 833(2):264, Dec. 2016.

Speagle, J.S. *MNRAS*, 493(3):3132–3158, 2020.

Springel, V., White, S.D.M., Tormen, G. and Kauffmann, G. *MNRAS*, 328(3):726–750, Dec. 2001.

Springel, V. et al. *MNRAS*, 391:1685–1711, Dec. 2008.

Suyu, S.H., Marshall, P.J., Hobson, M.P. and Bland ford, R.D. *MNRAS*, 371(2):983–998, Sept. 2006.

Suyu, S.H. et al. *ApJ*, 788(2):L35, June 2014.

Tessore, N. and Metcalf, R.B. *A&A*, 580:A79, Aug. 2015.

Thoul, A.A. and Weinberg, D.H. *ApJ*, 465:608, July 1996.

Tortora, C., Napolitano, N.R., Romanowsky, A.J., Jetzer, P., Cardone, V.F. and Capaccioli, M. *MNRAS*, 418(3):1557–1564, Dec. 2011.

Trujillo, I., Erwin, P., Asensio Ramos, A. and Graham, A.W. *AJ*, 127(4):1917–1942, Apr. 2004.

Van de Vyvere, L., Sluse, D., Mukherjee, S., Xu, D. and Birrer, S. *A&A*, 644:A108, Dec. 2020.

Van de Vyvere, L. et al. *A&A*, 659:A127, Mar. 2022.

Vegetti, S. and Koopmans, L.V.E. *MNRAS*, 392:945–963, Jan. 2009a.

Vegetti, S. and Koopmans, L.V.E. *MNRAS*, 400:1583–1592, Dec. 2009b.

Vegetti, S., Koopmans, L.V.E., Bolton, A., Treu, T. and Gavazzi, R. *MNRAS*, 408 (4):1969–1981, Nov. 2010.

Vegetti, S., Lagattuta, D.J., McKean, J.P., Auger, M.W., Fassnacht, C.D. and Koopmans, L.V.E. *Nature*, 481(7381):341–343, Jan. 2012.

Vegetti, S., Koopmans, L.V.E., Auger, M.W., Treu, T. and Bolton, A.S. *MNRAS*, 442(3):2017–2035, Aug. 2014.

Vegetti, S., Despali, G., Lovell, M.R. and Enzi, W. *MNRAS*, 481(3):3661–3669, Dec. 2018.

Viel, M., Becker, G.D., Bolton, J.S. and Haehnelt, M.G. *Phys. Rev. D*, 88(4): 043502, Aug. 2013.

Vogelsberger, M. et al. *MNRAS*, 444(2):1518–1547, Oct. 2014.

Wang, J. et al. *Nature*, 585(7823):39–42, Sept. 2020.

Warren, S.J. and Dye, S. *ApJ*, 590(2):673–682, June 2003.

White, S.D.M. and Frenk, C.S. *ApJ*, 379:52–79, Sept. 1991.

White, S.D.M. and Rees, M.J. *MNRAS*, 183:341–358, May 1978.

Winn, J.N., Rusin, D. and Kochanek, C.S. *Nature*, 427(6975):613–615, Feb. 2004.

Witt, H.J. and Mao, S. Probing the structure of lensing galaxies with quadruple lenses: the effect of 'external' shear, Oct. 1997.

Wong, K.C. et al. *MNRAS*, 465(4):4895–4913, Mar. 2017.

Xu, D. et al. *MNRAS*, 447(4):3189–3206, Mar. 2015.

Xu, D. et al. *MNRAS*, 469(2):1824–1848, Aug. 2017.

Xu, D.D. et al. *MNRAS*, 398(3):1235–1253, Sept. 2009.

Xu, D.D. et al. *MNRAS*, 421(3):2553–2567, Apr. 2012.

Young, P., Gunn, J.E., Kristian, J., Oke, J.B. and Westphal, J.A. *ApJ*, 241:507–520, Oct. 1980.

Zavala, J. and Frenk, C.S. *Galaxies*, 7(4):81, Sept. 2019.

Zhao, H. *MNRAS*, 278(2):488–496, Jan. 1996.

Zwicky, F. *Helvetica Physica Acta*, 6:110–127, 1933.

Zwicky, F. *ApJ*, 86:217, Oct. 1937.

## Colophon

This thesis is based on a template developed by Matthew Townson and Andrew Reeves. It was typeset with LaTeX $2_\varepsilon$. It was created using the *memoir* package, maintained by Lars Madsen, with the *madsen* chapter style. The font used is Latin Modern, derived from fonts designed by Donald E. Kunith.